Multiscale Modelling of Xenobiotic Transport Through Biotissues

Andrew Sneddon

A thesis submitted in partial fulfilment of the requirements of Liverpool John Moores University for the degree of Doctor of Philosophy

June 2020

Declaration

The work presented in this thesis was carried out at the Department of Applied Mathematics, Liverpool John Moores University. Unless otherwise stated, it is the original work of the author. While registered as a candidate for the degree of Doctor of Philosophy, for which submission is now made, the author has not been registered as a candidate for any other award. This thesis has not been submitted in whole, or in part, for any other degree.

Andrew Sneddon
Department of Applied Mathematics
Liverpool John Moores University
James Parsons Building
3 Byrom Street
Liverpool
Merseyside
L3 3AF
UK

Acknowledgements

First and foremost, I'd like to thank my supervisor, Steve. Over your years in LJMU, you created a team environment that made me look forward to coming into the office. The trips away, nights out and countless coffee mornings show what a tightly nit group Webb lab is. Your help throughout my studies has been invaluable; I will be forever grateful for the time and effort you have put in to help my finish this project. I'd also like to thank Joe for all his effort and input over the past couple of years. Your eye for detail regarding both the modelling and write-up have been invaluable.

I'd like to thank Dr Helen Colley and Professor Craig Murdoch at the University of Sheffield for being so warm an friendly with me from the day I began. I would like to thank Dr Ian Jarman for taking over as my supervisor at LJMU, and for his input in recent months. Finally, I would like to thank all the staff within the maths department at LJMU, which have been there through all my stages in academia.

To the squad in 6.13; Tez, Chantelle, Adam, and Ross, you've made the last four years beyond enjoyable. I couldn't of asked for a better group of friends. I could not have done it without you all.

I'd like to thank my Mum and Carl for supporting me over the past year I've been home. I'm super grateful for all you've done. And to my Dad and Kath, thank you for encouragement. Finally, to my wonderful girlfriend Cath, to whom I can finally answer the question of 'are you not done yet?', with a yes!

Abstract

In this thesis, we explore three methods that are commonly used to describe the movement of chemicals *in-vivo*. We employ a number of techniques to include parameters and features to account for the complex physiology of the system we model. In Chapter 2, we investigate a micro-scale model, to describe the distribution of chemicals applied to the skin topically using histology images. Due to the complex, heterogeneous nature of the skin, the model which is dependent on both space and time is solved using the finite element method. It is shown, that the model can predict the *in-vitro* distribution of chemicals with differing physico-chemical properties. In Chapter 3, employ a physiologically-based-pharmacokinetic (PBPK) model, to account for the systemic delivery of the percutaneous absorption of compounds. The output from the model described in Chapter 2 is then paired with this PBPK model in order to describe the distribution of xenobiotics at all stages of percutaneous absorption. The model is then used to understand how properties such as skin thickness, vehicle concentration, as well as the skin condition atopic dermatitis affect plasma concentration.
Finally, Chapter 4 describes a model for the permeation and uptake of polymersomes into spheroids. Model physiological parameters are derived from *in-vitro* data, which is then used to understand which binding parameters have the greatest contribution to the therapeutic efficacy of the treatment. Furthermore, optimal polymersome radii are derived for a range intracellular pore sizes.

Contents

Chapter 1

Introduction

1.1 Background

We live in an age where, for the most part, data is abundant. This holds true for the biological sciences, whereby both academics and industry researchers are continually contributing a wide variety of data, varying from simple rate reactions, to complex systems [1]. This has led to the development of new areas of research, such as quantitative systems pharmacology (QSP), which aims to create multi-scale, mechanistic models to bridge the gap between the biological knowledge of target scale effects, and more tradition modelling approaches like pharmacokinetic/pharmacodynamic (PKPD) models [2]. The creation of such systems requires that the modelling at each scale be representative of the process, and can be validated against experimental data.

When developing any new molecule that humans may be exposed to, it is important to understand how it may interact with the body. The development of *in-silico* mod-

els for this purpose is a key tool, which may be used at the early stages of development as a method for screening potential candidate molecules, through to the later stages where *in-vivo* data may be used to refine the models. The ability to understand how a molecule may distribute and possible metabolism pathways is key in being able to predict any adverse outcomes of a xenobiotic. This has led to the development of databases of adverse outcome pathways (AOPs), which aim to describe a sequential chain of causally linked events, which lead to an toxicological effect [3]. One example of such a database is the *AOPwiki* [4], which is a cross-continent effort to centralize all know AOPs. While a mechanistic understanding of what happens once the xenobiotic enters the body is key, there is also a need to understand how it may first enter the body. Humans are constantly exposed to a variety of xenobiotics, whether it be passive environmental exposure, application of cosmetics, or intake via nutrition or prescribed pharmaceuticals. Modelling the uptake of these xenobiotics into the body can be complex due to differences in molecule size, physicochemical properties, dose, and route of uptake. This leads to a multivariate problem, whereby, movement of xenobiotics through biotissues may vary hugely depending upon a combination of aforementioned physico-chemical properties. Within the literature, methods for modelling movement generally fall into two categories: spatially dependent models where movement is governed by a diffusion coefficient, and mass balance derived models where movement is generally a linear transfer or flow term linked to concentration [5]. Both styles of modelling are used commonly within the literature. The choice of which method to use is based upon the expertise of the user, the amount of data available, and the complexity of the system.

1.2 Physico-chemical properties

Throughout this thesis, we will make reference to a number of physico-chemical properties, which can be used to make predictions of the movement and distribution within biotissues. It is therefore important to define each of these properties and describe the capacity in which they may be used.

1.2.1 Partition coefficient, Log P

A partition coefficient, describes the ratio of concentrations of a given xenobiotic, within two immiscible phases at equilibrium. As different biotissues have varying levels of lipids, water, and proteins, it is essential to use partition coefficients to account for the varying concentrations of the xenobiotic within the different tissues.

1.2.2 Octanol water partition coefficient, $K_{o/w}$

The partition coefficient above is used to describe the ratio of concentration between any two phases. However, due to the vast number of phases for which we may wish to describe distribution between, a common method is to instead describe the ratio of concentration in two fixed phases. The octanol water partition coefficient describes the ratio of concentrations in water and octanol, which is a fatty alcohol. The ratio is described as follows,

$$\log K_{o/w} = \log \left(\frac{[solute]^{un-ionized}_{octanol}}{[solute]^{un-ionized}_{water}} \right).$$

We may therefore say, the larger the $logK_{o/w}$ value, the more lipophilic a compound is.

1.2.3 Acid dissociation constant, pKa

The acid dissociation constant, K_a, is a quantitative measure of the strength of an acid in solution. Suppose we have a chemical species HA which is an acid, that dissociates into A^-, the conjugate base of the acid, and a hydrogen ion, H^+. At equilibrium, the pKa is defined as follows,

$$pKa = \log_{10} \frac{[HA]}{[A^-][H^+]}.$$

This property is particularly important when modelling transport through biotissues, as charged compounds maybe have an increased affinity to proteins such as albumim, which may alter transport rates, elimination rates, and partition coefficients.

1.2.4 Solubility

Solubility, S, is a measure of how much of a compound can dissolve in a reference liquid at a given temperature. Given that the reference liquid is usually water, a compounds solubility along with a partition coefficient (calculated as a ratio of concentrations in the phase and water) may be used to estimate an upper bound of the concentration in the given phase. The solubility of a vast number of compounds can be found in the literature, however, where not available, may be estimated using an empirical formula as described in Chapter 2.

1.3 Diffusion and Brownian motion

In its simplest form, diffusion describes the net movement of particulates from a region of high concentration to a region of low concentration, for which, the difference in concentrations is often referred to as a concentration gradient, which describes the change over some unit of space [6]. In 3-dimensional space, Brownian motion can be used to describe diffusion. Brownian motion describes the random movement of particles suspended within a fluid, caused by their collision with faster moving molecules within the fluid. It is assumed that in a closed system, at a constant temperature after a given period of time, particles will be evenly distributed among the volume it consumes due to there being no preferential direction of movement. The kinetic energy of the particles, and therefore the speed at which they move may be used to calculate a diffusion coefficient, D, by taking an average of the squared velocity of diffusing particles [7]. This results in a constant with units of area per unit time.

The use of diffusion coefficients is very common when modelling the movement of particles using methods that solve for both time and space. These methods may be computationally expensive, especially when solving two and three-dimensional problems and often requires specialist software due to the complexity of calculations involved. This specialist software generally carries a cost, and therefore different methods of modelling movement may be more relevant in certain cases.

1.3.1 Stoke's law and the Einstein relation

Diffusion coefficients, as described in Section 1.3 are commonly used as a method for describing the speed at which molecules will diffuse across some space. A molecule's diffusion coefficient may be estimated experimentally; however, this value can be affected by the medium that the molecules is diffusing through and the temperature. Stoke's law was first derived by George Stokes in 1851 as a method for calculating the drag force exerted on spherical objects with small Reynolds numbers in viscous fluids [8]. The frictional force, F_d, is calculated as follows,

$$F_d = 6\pi\mu R v, \tag{1.1}$$

where μ is the viscosity, R is the radius of the spherical object, and v is the flow velocity relative to the object. The Einstein relation was derived in 1905 simultaneously by both Einstein [9], as part of his PhD thesis, and Sutherland [10], who used the same method to derive the equation. The full derivation on the equation is well documented within the literature, for example, see work by Kubo [11]. The idea behind the relation is that after a given period of time, with random movement, particles will be evenly distributed assuming a closed system. A particle's kinetic energy may be calculated using the Boltzman constant, k_B, and its temperature in kelvin, T. This may be related to the particles drift velocity, v, to give the following,

$$D = v k_b T. \tag{1.2}$$

This predicts that particles with a higher temperature have increased kinetic energy, and will therefore diffuse more quickly leading to a reduced time to reach an evenly distributed state.

A special case of the Einstein relation may be calculated for spherical particles through a liquid with low Reynolds number, known as the Stokes-Einstein equation [12]. This makes use of Stoke's law, as well as the Einstein relation to take into account the drag a particle may undergo while diffusing through a given liquid. The equation is calculated as follows,

$$D = \frac{k_B T}{6\pi\mu R}. \tag{1.3}$$

The equation is regularly used within the literature for a variety of scenarios by assuming that the particles modelled are spherical. One of the key benefits of the Stokes-Einstein equation is the ability to predict a diffusion coefficient with very little information required. However, due to the different ratios of the lipid and aqueous phases in biotissues, calculating diffusion coefficients by fitting to experimental data may be more accurate.

1.3.2 Fickian diffusion

Fick's laws are used to describe diffusion; diffusion is the movement of molecules from a region of high concentration, to an area of low concentration. Fick's first law may be derived by considering two regions, x on the left and $x + \Delta x$ on the right, with a crossing area A. In the left region, we have $N(x)$ particles, while in the right region

we have $N(x + \Delta x)$ particles. If we assume the probability of a particle moving left or right is equal, then the net amount of particles crossing to the right region is,

$$-\frac{1}{2}(N(x + \Delta x) - N(x)). \tag{1.4}$$

Therefore, the flux of molecules over a small period of time τ through A is,

$$J = \frac{-\frac{1}{2}(N(x + \Delta x) - N(x))}{A\tau}. \tag{1.5}$$

Where concentation is given as,

$$C(x) = \frac{N(x)}{A\Delta x}, \tag{1.6}$$

we may therefore instead write equation 1.5 in terms of concentration to give us Fick's first law given as,

$$J = -\frac{(\Delta x)^2}{2\tau}\frac{(C(x + \Delta x) - C(x))}{\Delta x} = -D\frac{\partial C(x)}{\partial x}, \tag{1.7}$$

where D is the diffusion coefficient. We are able to derive Fick's second law from the first law and an assumption of conservation of mass. If we instead imagine a box, with volume $A\Delta x$, and we have a flux of material entering the box, $J(x)$, and a flux exiting the box, $J(x + \Delta x)$. Due to conservation of mass, the rate of change of

particles within the box over some small time τ may be given as,

$$\frac{C(t+\tau)-C(t)}{\tau} = \frac{1}{\tau}\frac{(J(x)-J(x+\Delta x))A\tau}{A\Delta x}. \tag{1.8}$$

If we then take the limit as $\tau \to 0, \Delta x \to 0$ we get Fick's second law, given as,

$$\frac{\partial C}{\partial t} = -\frac{\partial J}{\partial x} = D\frac{\partial^2 C}{\partial x^2}. \tag{1.9}$$

We are able to extend this to the 3D case with spatial co-ordiantes (x, y, z), which would instead lead to,

$$\frac{\partial C}{\partial t} = -\frac{\partial J(x)}{\partial x} - \frac{\partial J(y)}{\partial y} - \frac{\partial J(z)}{\partial z}, \tag{1.10}$$

and

$$\frac{\partial C}{\partial t} = D\Big(\frac{\partial^2 C}{\partial x^2} + \frac{\partial^2 C}{\partial y^2} + \frac{\partial^2 C}{\partial z^2}\Big) = D\nabla^2 C. \tag{1.11}$$

It is possible to represent the Laplacian (∇^2) in terms of spherical coordinates, where u is the radial distance, ϕ is the polar angle and θ is the azimuthal angle. This leads to the following,

$$\nabla^2 = \frac{1}{r}\frac{\partial}{\partial r}\Big(r^2\frac{\partial}{\partial r}\Big) + \frac{1}{r^2\sin\theta}\frac{\partial}{\partial\theta}\Big(\sin\theta\frac{\partial}{\partial\theta}\Big) + \frac{1}{r^2\sin\theta}\frac{\partial^2}{\partial\phi^2}. \tag{1.12}$$

Substituting this into Equation 1.11 leads to,

$$\frac{\partial C}{\partial t} = D\left(\frac{1}{r}\frac{\partial}{\partial r}\Big(r^2\frac{\partial C}{\partial r}\Big) + \frac{1}{r^2\sin\theta}\frac{\partial}{\partial\theta}\Big(\sin\theta\frac{\partial C}{\partial\theta}\Big) + \frac{1}{r^2\sin\theta}\frac{\partial^2 C}{\partial\phi^2}\right) \tag{1.13}$$

A number of mathematical models for tumours make the assumption of spherical symmetry [13, 14, 15, 16], choosing to only describe what happens radially. This will reduce the problem to a single spatial dimension (in r). If spherical symmetry is assumed, it follows that both $\frac{\partial}{\partial\theta} = \frac{\partial}{\partial\phi} = 0$. This leads to a spherically symmetrical form of Ficks second law, with spherical coordinates,

$$\frac{\partial C}{\partial t} = \frac{D}{r^2}\frac{\partial}{\partial r}\Big(r^2\frac{\partial C}{\partial r}\Big). \tag{1.14}$$

1.3.3 Mass action

Mass action methods lend themselves very well to modelling the movement of particles due to the ease of formulating a set of equations to model a system. Regions are described as a single or set of well mixed, homogeneous compartments with varying volumes. Examples of methods that can be derived using mass action include finite differences and pharmacokinetic (PK) models. Both these methods may comprise of a series of compartments for which the flow of the modelled molecules is governed by a difference style, first-order transfer term. To represent a spatial dimension like in the finite differences method, a series of compartments can be created, which physiologically may represent a single feature in a system. The change in concentration within these compartments is then calculated using a series of ordinary differential

equations. A benefit of this type of modelling is the ease at which a system may be created; the governing equations may be derived by simply referring to a schematic of the system which the user wishes to model. Furthermore, relatively little expertise is needed to solve the system, with the option of using software such as *SimBiology* which can generate code for a given model. While this may be beneficial to users with little expertise, caution must still be taken in formulating a system. Many of the software packages do contain soft checks on systems such as unit checks, however, users with little expertise should always consult someone with more modelling knowledge when implementing something based upon a *in-silico* prediction. One benefit of this method is that due to the low complexity of the system, the computational cost is low.

1.4 Transport modelling in the skin

Transdermal drug delivery can be traced back to ancient times, where the Ebers Papyrus, dating back to 1550 B.C. suggests various remedies for a variety of skin conditions [17]. Historical reports also exist alluding to flying ointments, where hallucinogenic substances were suspended in lipophilic bases. Preparations were then applied to broomsticks, held in between the legs [18]. It is evident that, for a long time, humans have understood the ability to deliver drugs transdermally. However, it wasn't until work by Rothman in the 1940s that we began to understand the role of physico-chemical properties in a chemical's ability the permeate the skin [19]. From the 1940s through to the 1970s work by Higuchi [20, 21], Hadgraft & Somers [22],

and Blank & Scheuplein [23, 24, 25, 26] described different aspects that were key to a drug's ability to permeate the skin. Since then, the models used to describe the transdermal delivery processes have increased in sophistication, varying from simple steady-state models, through to complex multi-phase spatial models.

A simple way to describe solutes passing across the skin is to assume steady-state conditions, where the stratum corneum is the barrier and behaves as a pseudo-homogeneous membrane, with properties not changing with time or space. We can relate the amount of solute Q, that is crossing the skin with an area, A, over a time period, T, with a constant concentration gradient between the two surfaces, ΔC_s, with a diffusion coefficient within the skin D, with a path length h, to get,

$$Q = \frac{DAT\Delta C_s}{h}. \tag{1.15}$$

Steady-state may only be reached after the lag time for solute diffusion across a homogenous membrane, which is given as $h^2/6D$. This may also be estimated, by looking at the cumulative solute accumulation, where the lag time is given as the x-axis intercept [27]. Due to the assumption of steady-state, and not mimicking real-life situations, the models are of limited use. However, steady-state models are helpful in estimating the partition coefficient, k_p, between the solute and the skin as a ratio of the concentrations at steady state. Where J_{ss} is the flux at steady state, and the partition coefficient is given as the ratio of the concentrations within the skin, C_s and

vehicle C_v, Equation 1.15 may be re-written as,

$$J_{ss} = \frac{k_p D \Delta C_v}{h}. \tag{1.16}$$

Estimating k_p is the first step researchers should take when looking a the uptake of solutes across the skin for a variety of research topics. When trying to identify potential drugs for transdermal delivery, drugs need to be soluble to permeate to lower layers and enter systemic circulation. When screening for potentially hazardous chemicals for pesticides or household goods, solutes with lower skin permeability are favorable to reduce the potential for entering the systemic circulation.

1.4.1 Pharmacokinetic models

Pharmacokinetic (PK) modelling is a commonly used method to study the temporal dynamics of compounds within the body. An assumption is made, that the region of interest (whole body or tissues within part of the body) may be split into several well-mixed compartments, where transfer between given compartments may be calculated by first-order rate equations [28]. This may be favourable for simplicity, as these models only require ordinary differential equations (ODEs), that are only time dependent. When applied to the skin, a PK model may take different layers skin to constitute the compartments, where the first-order rates may be determined by looking at the partition coefficient $\log P$ of the drug. A typical model intended to represent an experimental set-up can be found in a paper by Davies et al. [29], which was constructed as follows: a compartment for the application of the chemical, DP; a

compartment for the stratum corneum, SC; a compartment for the rest of the viable skin, VS; and a compartment for the fluid below the skin, RF. Where M followed by a subscript denotes amounts, C followed by a subscript denotes concentrations, K followed by subscripts donates the first-order permeation rates from a compartment to a neighbouring compartment, E_{DP} is evaporation loss and E_v flow from the skin to the space below, the model was constructed as follows:

$$\frac{dM_{DP}}{dt} = -E_{DP}C_{DP} - K_{DP:SC}C_{DP} + K_{SC:DP}C_{SC}, \tag{1.17}$$

$$\frac{dM_{SC}}{dt} = K_{DP:SC}C_{DP} - K_{SC:DP}C_{SC} - K_{SC:V}C_{SC} + K_{V:SC}C_V, \tag{1.18}$$

$$\frac{dM_{VS}}{dt} = K_{SC:V}C_{SC} - K_{V:SC}C_V - E_VC_V, \tag{1.19}$$

$$\frac{dM_{RF}}{dt} = E_VC_V. \tag{1.20}$$

It may be noted that the ratio of the two first-order rate terms between compartments are proportional to the partition coefficients between the compartments. These values are calculated by fitting to experimental data. A particular advantage of this style of modelling is the ease of pairing with a whole-body physiologically based pharmacokinetic (PBPK) model, in order to model systemic exposure. However, PK modelling does not account for spatial differences in the skin [27], as compartments are assumed to be homogeneous and well mixed. Furthermore, PK models cannot account for membrane properties and multiphase transport that may be accounted for in transient models. Attempts have been made by McCarley & Bunge [28, 30, 31] and Reddy et al. [32] to mimic the membrane properties found in the skin. However, as found with PK models, the parameters used do not relate to the physiology of the

skin, and therefore the predictive power of the model is directly linked with the data used to parametrise it.

1.4.2 Finite differences

An extension to the PK model described in Section 1.4.1 was published by Davies et al. who made use of the finite difference method [29]. The finite differences approach instead treats each compartment of a PK style model, as a series of compartments, which when applied to modelling skin, allows the user to account for concentration gradients across skin layers and time lags [33]. Transfer between layers within the same compartment a function of the difference in concentrations, while movement between compartments is modelled in the same way as PK models. Davies model consisted of three skin compartments: stratum corneum; epidermis; and dermis; and two compartments for the donor phase and receptor fluid. Each of the three skin compartments, as well as the donor phase compartment, was then divided into a set of ten sub-compartments. Like other PK models, movement between compartments is a function of concentrations in each of the compartments and a first-order rate term. Movement between the sub-compartments was governed by the concentrations within each of the sub-compartments. The model was then fitted to experimental data, where the concentration in each of the equivalent compartments was recorded at 5 time points for 13 different chemicals.

To assess the effectiveness of the finite differences approach, the residual sum of squares (RSS) was calculated for the finite differences model, as well as 1-2-and-3-compartment models, as well as the Bayesian information criterion (BIC). A BIC

value is used for model selection, where model accuracy is desirable, and model complexity is penalised. The addition of the penalisation term reduces the chance of selecting a model which over-fits the data. The authors found that the finite differences model outperformed each of PK models for 6 of the 13 the chemicals tested. For the chemicals where a PK model outperformed the finite difference model, the difference in RSS was 1.2%, or less. However, the increase in the number of parameters meant that the finite difference model had an inferior BIC score for all of the chemicals. While it has been shown to outperform PK models, a finite difference approach still lacks the use of physiologically relevant parameters.

1.4.3 Finite volumes

Similar to the finite difference method, the finite volume method is a method for reducing partial differential equations down to algebraic equations. Volume integrals that contain a divergence term, ∇, can be converted to surface integrals through the use of the divergence theorem [34]. These terms can instead be evaluated as fluxes along the surface of a given finite volume.

One example of the use of the finite volume method is by Naegel et al. [35]. The authors created a 2-dimensional brick and motor style model, where the corneocytes are embedded within the lipid phase [36]. The model is then treated as having three phases: the corneocyte phase Ω_{cor}; the lipid phase; Ω_{lip}; and a deeper skin layer phase, Ω_{DSL}. Transport in each phase was modelled using Fick's second law, with diffusion coefficients for each phase being derived experimentally. To calculate the amount of substance passing through an interface, a surface integral must be calculated. This

leads to the use of the finite-volume method, with the resulting linear system being solved using an algebraic-multigrid method. The authors then compared the *in-silico* depth profiles to those obtained experimentally and found that the model fit the data well.

1.4.4 Random walk

The very essence of diffusion is the random movement of particles, and as a result, several investigators have spent time modelling diffusion using random walk methods. By pairing a random number generator with some governing rules of diffusion, particles movement may be simulated. Frasch [37] published a model using a realistic stratum corneum geometry from mouse skin. For any given time step, n, the location of the particle is given as $(x(n), y(n))$, which is determined from its previous position $(x(n-1) + \Delta x(n), y(n-1) + \Delta y(n))$, as well as its squared displacement $r^2(n) = \Delta x^2(n) + \Delta y^2(n)$. The mean squared displacement was related to the diffusivity through the following,

$$< r^2 >= 4Dt \tag{1.21}$$

where D is the diffusion coefficient and t is time. Random walk models are a powerful tool, and have been shown to be more effective then quantitative structure-permeation relationship (QSPR) models at predicting diffusion coefficients from physico-chcemical properties.

1.5 Transport modelling in tumours

While many mathematical models exist that describe the uptake and delivery of nanoparticles to tumours, the lack of treatments that make use of the technology shows that there is still a gap between theoretical knowledge and implementation. A large portion of the research within the field has focused on the delivery across the vascular network of the tumour, as this is the main barrier when trying to deliver large objects such as nanoparticles *in-vivo* [38, 39]. However, there are a number of papers on the diffusion and binding of molecules in both tumors and spheroids of tumor cells. A measure of an anti-cancer molecule's effectiveness, is the fraction of cells that are killed after treatment. Therefore, the goal is to create a treatment that may permeate well, and only kill the targeted cancer cells.

A theoretical paper by Graff et al. [13] looked at the diffusion and binding kinetics of antibodies with antigens within tumour spheroids. The model consisted of 3 partial differential equations (PDEs), which modelled the temporal distribution of antigens, antibodies, and the antibody-antigen complex. Both the antigen and antibody-antigen complex was assumed to be fixed in space, while antibody movement was modelled using Fick's second law, with an assumption of spherical symmetry. Antibody-antigen complex formation, disassociation, and metabolism followed first-order kinetics. The authors found that the time taken to reach equilibrium for binding was much quicker than that of the diffusive time-scale, which suggests that the rate of diffusion was the limiting factor for antibody treatment.

A paper by Ghaghada et al. [40] chose to account for a non-homogeneous distribu-

tion of cell surface receptors. The authors argued that once the initial complex has formed, only a fraction of the surface receptors on the cell may then bind, which they named a cells area of influence (AOI). Related, they also include a term for the active fraction area of the carrier (AFAC), i.e. the fraction of the nanoparticle available for binding, as a function of tether, ligand and nanoparticle size. The authors found that binding and the receptor-mediated endocytosis took place on different time scales, and therefore, a kinetic model was created to include both phenomena.

Baish et al. [41] argued that the vast difference in vascularity between tumour and regular tissues may be quantified with two measures: δ_{max}, the maximum distance in the tissue from the nearest blood vessel; and λ, a measure for the shape of the space between vessels, which may be used to determine the rate of delivery into tissue. It was found that the maximum time to deliver the nanoparticles to any point within the tumour scales with the square of δ_{max}. The use of these metrics also allowed the authors to show that emerging therapeutic agents that inhibit or increase the vascularity of the tumour have potential for treatment *in-vivo*.

Stylianopoulos et al. [42] created a model, which looked at the electrostatic interactions between the delivered nanoparticles and the charged vessel walls of vascular tumours. They found that a small increase in electrostatic attraction doubled the flux of the nanoparticles. Furthermore, they found that for a given nanoparticle radius, there exists a surface charge density threshold, for which a large increase in transvascular transport is predicted. The vascular domain of the tumour in the mathematical model was created using gradients of vascular endothelial growth factors and fibronectin. Blood flow through the tumour was assumed to follow Poiseuille's law,

which relates flow to the blood's viscosity, pressure gradient and length and diameter of the vascular network. Flow across the vascular network wall follows Starling's law, which accounts for varying force on the vascular wall depending on heart rate and stroke volume. Interstitial flow was governed by Darcy's law, which describes the flow through a porous medium. A model for the uptake of the nanoparticles was not included. Instead, Stylianopoulos et al. focused on the transvascular flux; a measure of nanoparticle delivery to intracellular space rather than the uptake, as it was shown by both Graff and Ghaghaha [13, 40] that the permeation was the rate limiting factor in uptake.

A model by Van de Ven et al. [43] looked at the effect of nanoparticle delivery on the growth of avascular tumours, which was paired with a model by McDougall et al. [44] to account for angiogenesis. A key feature of the model is allowing tumour growth, which is dependent on oxygen and nutrient gradients, as well as whether the drug concentration, T_{drug} is above some threshold in proliferating cells. They were able to achieve this by splitting the tumour into three regions: a proliferating region, where the cells have sufficient levels of nutrients and oxygen; a hypoxic region, where cells have sufficient levels of nutrient and oxygen to survive, but not enough to proliferate; and finally, a necrotic region, where the nutrient and oxygen levels are too low. Growth was then modelled using a generalized form of Darcy's law. Transport of both the nanoparticles and oxygen made use of reaction-diffusion equations for each of the regions. The effect of the drug on the tumour cells was assumed to only take place within the proliferating region, effective when drug concentration is above a given threshold. This led to the authors being able to predict what dose is required

to reduce the tumour volume by 50%.

Frieboes et al. [45] created a model for the accumulation of nanoparticles within tumours. Like in Van de Ven et al. [43], tumour growth is modelled by splitting the mass into proliferating, hypoxic and necrotic regions, with tumour growth velocity being governed by Darcy's law. The authors looked at optimising nanoparticle properties such as size, ligand density, and receptor-ligand density to maximize the number of nanoparticles adhering to the vascular walls of the tumour, therefore increasing the delivery of the nanoparticles to the target cells, and reducing off-target toxicity.

A paper by Namazi et al. [46] incorporates a phase lagging model of drug diffusion. The purpose of the lag time is to quantify the time difference between the delivery of the drug and increase in concentration within the tumour. The authors were able to solve a standard diffusion equation via the use of substitutions and a Laplace transformation in order to find the concentration profiles for three different diffusion coefficients. Using this, they were able to create an effective diffusion coefficient for a drug, which could predict the depth to which the drug penetrates with strong accuracy when compared to experimental results ($R^2 = 0.99$).

In order to compare the effectiveness of encapsulated treatments, Wang et al. [47] compared free and encapsulated forms of the same drug in tumours. A spatio-temporal model was created comprised of two PDEs representing the dynamics of drug concentration and volume fraction of cancer cells. Uptake is modelled with first-order kinetics, which is related to a reduction in the number of cancer cells. This then allowed the authors to model variable tumour volume. Experimental data,

paired with the model showed that the use of encapsulated drug leads to a three-fold increase in the death of tumour cells when compared with the free-drug equivalent.

Scapra et al. [48] looked at quantifying the release of the therapeutic agent released from nanoparticles inter-cellularly. They developed an assay based upon the hydrophilic dye, fluorescein. Due to the large aqueous component of the cells, fluorescence could be detected once the nanoparticles were internalised and the payload released. The number of internalised nanoparticles per cell was estimated based on the intensity of the fluorescence. It was found that after one hour, the average number of nanoparticles per cell was 209. After three hours, the average was 238 per cell, and after twenty-four hours, the average was 286 per cell. This non-linear relationship between time and the number of internalised nanoparticles suggests that extracellular concentration may not be the only driving factor in the internalisation of the nanoparticles. It may also suggest that cell surface-receptors are not always returned to the cell surface, as previously thought.

To get a complete understanding, drug pharmacokinetics (PK), and effects within the tumour must also be predicted. Work by Sinek et al. [49] modelled the PK of doxorubicin and cisplatin; two commonly used tumour treatments. Sinek et al. made use of a finite-element model developed by Zheng et al. [50], which simulates multi-scale tumour growth and angiogenesis. Three ordinary differential equations were used to represent compartments within the model, with an extra compartment added when modelling doxorubicin. These compartments represent; extracellular, cytosolic, and DNA-bound drug, with the extra compartment representing intracellular organelles. Model parameters were obtained by fitting data, while initial volumes and concentra-

tions within compartments were estimated. The study shows that the effectiveness of therapy relies heavily upon the cellular environment.

1.6 Research novelty

This thesis describes the development of three *in-silico* models, which describe the movement of xenobiotics through biotissues. In Chapter 2, we describe a novel method for predicting the movement of solutes and their metabolites through human skin. Section 1.4 outlines both empirical and mechanistic approaches to modelling transdermal drug delivery. However, these approaches tend to ignore the complex physiology of the skin and instead describe the skin as a collection of approximated layers. Such layers are then treated as homogeneous media with typically no intra/extracellular distinction. Another key issue in many models is that barrier properties neither change with time, nor position and therefore diffusion is strictly governed by the concentration at that point in space. Furthermore, many models assume a reservoir-like, topical, infinite doses which allows the underlying equations to then be solved by making use of steady state-kinetics. However, this is very difficult to mimic *in-vivo* and has little application in real-world situations. Parametrising traditional models is also an issue as values are calculated as averages rather than capturing the actual microscale details. This leads to issues when the physiology of the skin may vary (e.g. comparing drug delivery and enzyme kinetics in the skin from different areas of the body).

Several bodies of work exist which aim to overcome some of these shortfalls, by look-

ing in detail at specific layers of the skin [51, 52, 53]. However, they fail to combine this level of detail to create a complete model of transdermal drug delivery. To date, perhaps the best attempts at overcoming the aforementioned issues was published by Kattou et al. [54], and Chen et al. [55], who both created a finite element model of the skin. The models included layer-specific partition and diffusion properties, and a brick and mortar style stratum corneum. However, unlike the model described in Chapter 2, it does not include geometrically correct discrete cells, and does not account for the barrier properties of the stratum corneum caused partially by the presence of proteins such as keratin and filaggrin [56].

Within Chapter 3, we develop a PBPK model, which when paired with the model in Chapter 2, can predict the temporal distribution of chemicals entering the body transdermally. Several PBPK models exist which allow for chemicals to enter the body via the skin [57, 58, 59, 60, 61, 62]. However, these models are all designed to predict the uptake and distribution of a single stated chemical. Furthermore, in all of these models, the skin is treated as a single compartment. It was shown by Davies et al. [29], that when using compartmental models for the skin, an increase in the number of compartments allowed the model to better fit the data. Therefore, to the best of our knowledge, there are no examples of models within the literature that accounts for the complex physiology of the skin, combined with the ability to predict drug distribution based upon physico-chemical properties.

When modelling nanoparticle delivery, there are two common approaches: a complex binding model with no spatial component such as those found in work by Sorrell et al. [63], and Ghaghada et al. [40]; or a simple binding model where a spatial

component is included [13, 47, 64]. The choice to either model binding complexity or a spatial component may be due to the added computational complexity required when numerically solving partial differential equations when compared to ordinary differential equations. The complex binding models have a far greater number of equations when compared to the spatial models, which only account for unbound, bound, and internalised nanoparticles. In Chapter 4, we combine the complex binding model by Sorrell et al. [63] with a spatial framework, while greatly reducing the number of equations required using statistical moment closure. This model reduction allows for a greater in-depth analysis of the system, allowing us to understand what the key parameters are which affect the delivery of these polymersomes, and what physiological parameters affect their permeation.

1.7 Thesis overview

This thesis details the development of three models which describe multi-scale transport of xenobiotics in both *in-vivo* and *in-vitro* settings in order to better understand how physiological parameters effect absorption, distribution, metabolism and excretion. A number of mathematical techniques are utilised to ensure that the model closely mimics the experimental set up. Where space isn't an important factor, a system of ODEs are used to describe the rate of change of the xenobiotics with respect to time. When space is a factor, a system of PDEs are instead used to predict the dynamics of various variables. This thesis consists of three research chapters and one discussion chapter.

Chapter 2 describes the development of a novel numerical, continuous-discrete hybrid partial differential equation approach to describe the time dependent spatial distribution of a given compound and its metabolites. Model parameters are derived from a number of different literature sources, based on the physico-chemical properties of the compound modelled. The model is then validated against published *in-vitro* data, for a number of compounds with different initial concentrations and physico-chemical properties. The model is highly adaptable and can be used to model skin from different parts of the body, different exposure scenarios, and different metabolism pathways.

In Chapter 3, we describe a multi-purpose whole-body PBPK model. The model is adapted to account for a percutaneous absorption through inclusion of a first-order kinetic term in the skin compartment. We derive unknown PBPK parameters for lidocaine by fitting the model to published IV data. The model is then used to understand how various parameters, such as skin thickness, initial concentration and size of area of application effect the temporal dynamics of plasma concentration. We also investigate how a reduction in skin-barrier properties found with diseases such as atopic dermatitis, effects plasma concentration when paired with a varied skin thickness, initial concentration, or size of area of application.

Within Chapter 4, we take a previously published model of polymersome uptake by cancer cells, and reduce the number of equations required through the use of a statistical moment closure. The model is then adapted to describe the permeation, and uptake of polymersomes in a spheroid with the addition of a spatial dimension. Spheroid physiological parameters are initially estimated by fitting the model

to experimental data of polymersome uptake provided by collaborators. Optimal polymersome properties were then calculated to ensure the maximal volume of therapeutic dose is delivered to cells across the spheroid. Global sensitivity analysis was then performed to understand what the key binding parameters are, and how they affect the uptake of polymersomes within the spheroids.

Chapter 2

Modelling the transport of xenobiotics through human skin

2.1 Background

The skin can be described as three layers: the epidermis, the dermis and the subcutaneous tissue, which all have differing structural and physiological properties. The innermost layer is the subcutaneous tissue: it consists of fibroblasts, which attach the upper layers of the skin to skin and bones; adipocytes, which contain much of the body's fat stores for insulation and energy; and macrophages for clearance of cellular debris and pathogens [65]. The middle layer of the skin is the dermis: it also consists of fibroblasts, adipocytes and macrophages, as well as the dermal matrix containing collagen for strength and elastin which provides elasticity [66]. The dermis connects to the epidermis via the basement membrane.

The outermost layer of the skin is the epidermis, consisting of 90% increasingly flat-

tening keratinocytes suspended within a lipid matrix [51]. The epidermis may be further divided into four strata, from the inner to the outer they are: the stratum basale; stratum spinous; stratum granulosum; and the stratum corneum. The basale layer consists of mainly keratinocytes, with some merkel cells present, which are responsible for light touch sensation [67]. Within the spinous layer, keratinocytes start to connect via desmosomes and start to produce lamellar bodies, which contain lipids and catabolizing enzymes, both of which are essential chemical/biochemical barriers [68]. Within the granular layer, further secretion of lamellar bodies take place, and cells start to lose organelles and nuclei. At their final stage of differentiation, keratinocytes become known as corneocytes, which make up the outermost layer of the epidermis, the stratum corneum. One characteristic the keratinocytes posses is that they become flatter as they progress from the basale layer to stratum corneum.

The stratum corneum is the primary resistance layer of the skin, greatly reducing the ability for hydrophilic compounds to permeate. Compounds that can permeate generally do so via the intracellular lipid layer [69]. The structure is akin to a bricks and mortar, where the bricks represent the non-living corneocytes and the lipids, organised into bilayers, may be thought of as the mortar. Due to this structure, the route for a diffusing compound is tortuous, causing hydrophilic compounds to travel via lipid head group regions, and lipophilic compounds to travel through lipid tails. Once a compound has permeated the stratum corneum, it may diffuse through the further levels of the epidermis, where it may be subject to various phase II metabolising enzymes, which have been shown to be expressed within the lower layers of the epidermis [70, 71].

For the most part, drugs are delivered in two ways: intravenously (IV) or orally. However, both methods of administration have drawbacks. Drugs delivered intravenously generally require a trained healthcare professional, run the risk of infection and may compromise the structure of the veins at the delivery site. Drugs administered orally may have their structure altered within the gastrointestinal (GI) tract, generating a certain level of uncertainty on the degree and speed of uptake between patients [72]. This leads to a need to develop new methods of administration to bypass the drawbacks of IV and oral administration. Transdermal drug delivery is one possible alternative method of delivery, which is being utilised more by pharmaceutical companies due to a number of advantages such as ease of administration, bypassing the GI tract, lower enzyme activity, localised delivery, and it is particularly useful for drugs where there is a significant first pass effect by the liver.

Due to the complex structure and physiology of the skin, the number of drugs designed to be delivered transdermally is still low; although, the number of drugs being approved for delivery transdermally has increased year by year since the 1980's [69]. It is therefore necessary to develop a microscale knowledge of the mechanisms that govern transdermal drug delivery to develop a predictive tool to screen potential candidates. There are currently very few drugs that are delivered via the skin (e.g. nicotine patches, fentanyl spray and patches) but with advancements in technology such as permeability enhancers and hypodermic needles the future potential is promising. Development of physiologically relevant *in-silico* models will aid in the optimisation of the use of permeability enhancers due to the understanding of drug delivery and the ease and speed of simulations.

The mathematical modelling of transdermal drug delivery is a growing area of research which has received much more interest in recent years, including a task force set up by Cosmetics Europe [73]. Cosmetics Europe represent a consortium of Europe's largest cosmetic and personal care companies, who were particularly interested in an *in-silico* approach to defining bioavailability and metabolism of xenobiotics in the skin. This aligned with a wider desire across multiple scientific disciplines to greatly reduce animal testing through the use of initial screening processes for potential candidate chemicals. Many papers have been written attempting to describe aspects of drug delivery via the skin using both mechanistic and empirical approaches which have been summarised by both Mitragotri et al. and Russel & Guy [27, 74]. However, the publications summarised in these bodies of work tend to ignore the complex physiology of the skin, and instead try to describe it as a collection of approximated layers. Such layers are then treated as homogeneous media with typically no intra/extracellular distinction. Another key issue in many models is that barrier properties neither change with time nor position and therefore diffusion is strictly governed by the concentration at that point in space. Furthermore, many models assume a reservoir-like, topical, infinite dose which can then be solved using steady state kinetics. However, this is difficult to mimic *in-vivo* and has little application in real world situations. Parametrising traditional models is also an issue as values are calculated as averages rather than capturing the actual microscale details. This leads to issues when the physiology of the skin may vary (e.g. comparing drug delivery and enzyme kinetics in the skin from different areas of the body). There are examples of work which have attempted to account for some of these shortcomings. However,

they still fall short by simplifying large parts of the complex physiology of the skin. Within this chapter, we describe the development and implementation of a novel technique for predicting the delivery and metabolism of xenobiotics transdermally. Our model uses a numerical, continuous-discrete hybrid, partial differential equation approach to describe both the steady-state and time-dependent spatial distributions of a given compound and its metabolites. This method captures the complexity of transdermal delivery, by incorporating discrete cell geometries gathered from histology sections of native human skin, and allows for multiphase transport.

2.2 Methods

2.2.1 COMSOL

COMSOL Multiphysics is a finite element simulation software for the modelling of numerous processes covering a vast array of scientific disciplines. The software allows the user to utilise a range of packages which may be used to model a variety of physical phenomena. The type of problems solved in COMSOL are generally both spatially and temporally dependent, and are therefore solved using partial differential equations (PDEs). COMSOL utilises a powerful numerical technique, named finite the element method. This method can be used to solved PDE's in the weak form, which will be discussed in more detail in Section 2.2.2. Of particular use to us is the *transport of dilute species* module, which may be used to model both diffusion and convection of multiple chemicals in up to three dimensions.

2.2.2 Finite element modelling in COMSOL

A dynamic, mathematical problem which is time and space dependent is generally expressed in terms of partial differential equations. However, for complex geometries, like the discrete cells found in our skin model, analytical methods cannot be used, due to the difficulty in constructing a set of functions which satisfy the boundary conditions. However, for models with less complexity, analytical solutions to diffusion equations exist. Instead, we rely upon numerical techniques, developed over the last few decades to approximate the solutions to these problems. The finite element method relies upon discretising the domain into a set of smaller domains named elements. Calculations are then made for each element, which can then be used to calculate a solution for the entire domain. An example of a small amount of our model domain, reduced into elements, is shown in Figure 2.1.

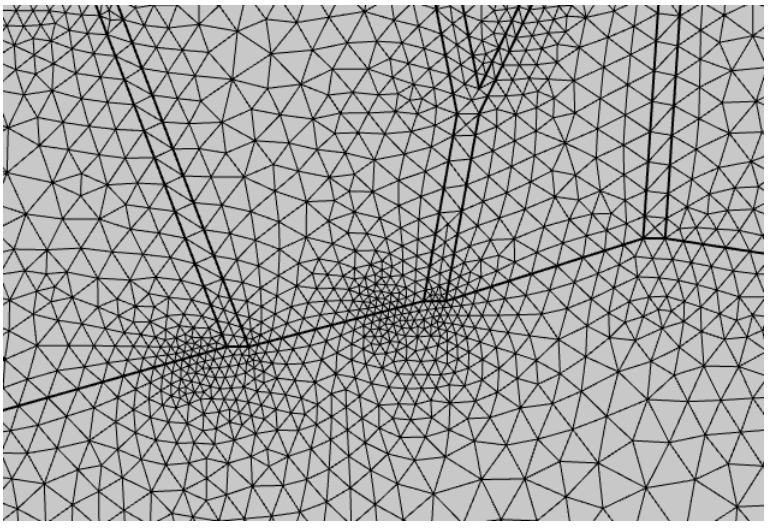

Figure 2.1: An example of a geometry discretised into elements. Solutions are generated for each of these elements, and are paired together in order to generate a result for the entire domain.

The mathematical model for diffusion, Fick's Second Law, is generally given in its

strong form: a governing equation, with accompanying boundary conditions, which gives the concentration at every point within a domain a solution must satisfy. Instead, to numerically approximate a solution, the finite element relies on the weak form of an equation. The weak form is obtained by multiplying the governing equation by some test function, then integrating over the domain. The test function, and solution, are assumed to belong to Hilbert spaces. A Hilbert space is an infinite-dimensional function space, which has the beneficial property of allowing the test functions to be manipulated in the same way a vector is in a vector space. Green's first identity is then used to remove the Laplace operator. If this then holds for all points in Hilbert space, then the weak form of an equation is complete. This is particularly beneficial over the strong form of an equation, as it does not have to be well defined at all points. An approximate solution may then be calculated in a finite-dimensional subspace of the Hilbert space, which may be expressed as a linear combination of a set of basis functions, belonging to the subspace [75]. The basis functions are generally very simple piecewise functions; however, the combination of these functions in order to minimise the error between the approximation and solution is generally kept secret by software providers.

2.3 Model creation and parametrisation

The unique and novel feature of the model described in this chapter is the ability to create geometries which mimic that of native human skin, which allows for the modelling of multiphase transport. Figure 2.2 shows E-cadherin immunohistochemical-

stained native human epidermis. Shown are discrete keratinocytes within the lower layers of the epidermis, which become flattened as they displace outwards towards the stratum granulosum and corneum. To create the model geometry, we begin by defining boundaries of each of they layers using *WebPlotDigitizer*. *WebPlotDigitizer* allows a user to select points on an image, which can be exported to packages such as Matlab and used to define a geometry.

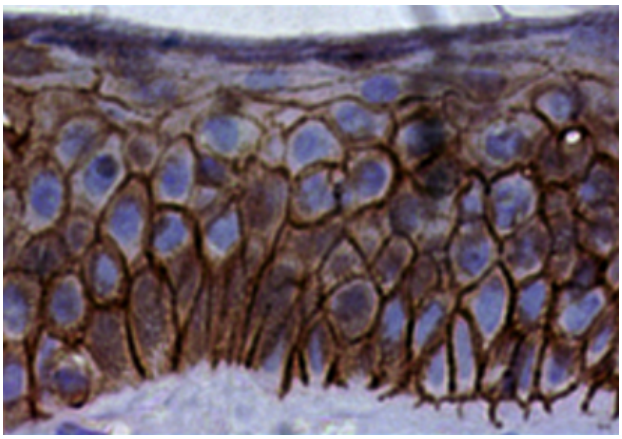

Figure 2.2: E-cadherin immunohistochemical-stained native human epidermis, which is used to define the geometry of our model. Discrete keratinocytes are visable in the lower layers, which then flatten as they displace outwards towards the stratum granulosum and corneum.

WebPlotDigitizer may also be used in the creation of the boundaries of the discrete cells. One possible higher throughput approach is to use a Voronoi tessellation, which only requires the point of the nucleus. This method is discussed in detail, and is utilised in Chapter 4. One limitation of this method is that it only generates convex polygons, and therefore would not pick up all the details of the histology image shown in Figure 2.2. Instead, we chose to define the boundary points by selecting points along it. While this took longer than the alternate approach, it picked up far more of the detail of the histology image. In order to assess the range of extracellular gaps,

transmission electron microscopy (TEM) was used. Figure 2.3 show a TEM image on native human skin. With an understanding of the size of extracellular gaps, the geometry created could be altered by moving all cell boundary points inward towards the nucleus, in order to create gaps akin to that found in Figure 2.3.

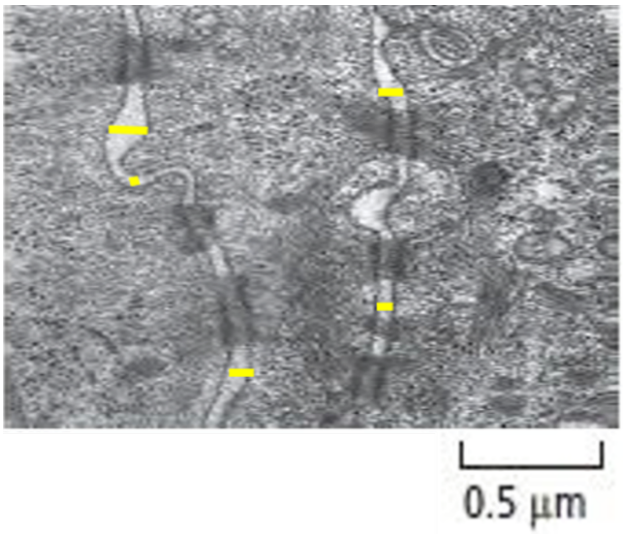

Figure 2.3: Unpublished transmission electron microscopy image of human epidermis was used to assess size of extracellular gaps.

This leads to the construction of the final geometry of the epidermis shown in Figure 2.4. The two outer most layers, the stratum corneum and stratum granulosum, are described as individual, whole layers, while the lower layers are instead being described by the discrete cells. Finally, we must define the dermis. Kretos et al. [76] reported, for native human skin, the dermis is on average, 300 μm thick. The geometry for the dermis may be generated, by utilising the points which form the base of the epidermis, to form a union, and create a geometry with a 300 μm depth.

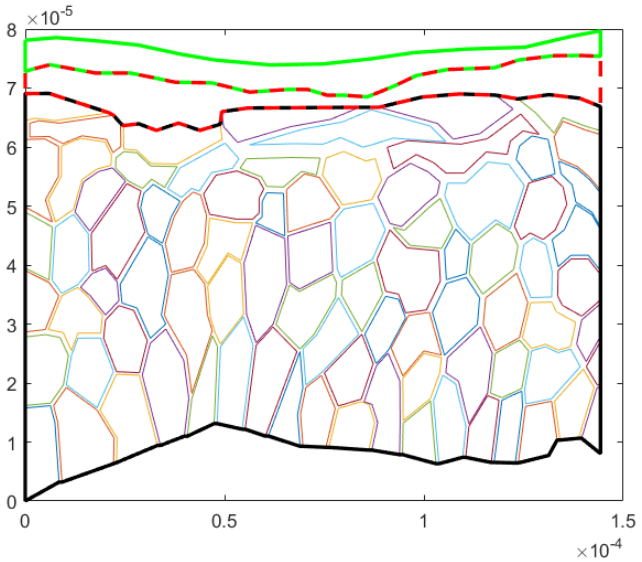

Figure 2.4: The physiologically relevant skin geometry generated using the histology image in Figure 2.2. Visible is the stratum corneum, stratum granulosum, and discrete cells within the lower layers of the epidermis manually segmented, using *WebPlotDigitizer*, with intracellular gaps estimated using the TEM image shown in Figure 2.3.

2.3.1 Calculation of diffusion coefficient for the stratum corneum

With the model geometry defined, we now can assign transport properties to each of the regions. As each of the stratum within the epidermis have varying levels of lipids, proteins, water and morphology, each must be assigned a different diffusion coefficient. Within the literature, significant effort has been put into predicting diffusion coefficients across the stratum corneum (SC) using a variety of techniques. As the stratum corneum is the primary barrier layer of the skin, the transfer of any xenobiotic across the skin initially depends on the upon its ability and time taken to permeate the stratum corneum.

One method for predicting diffusion coefficients, are so-called quantitative structure permeation relationship (QSPR) models. QSPR models extend quantitative

structure-activity relationship (QSAR) models, by including physiochemical properties. The main focus of QSPRs has been the calculation of permeability coefficients (k_{sc}), defined as being the steady-state flux of a chemical across the skin, normalized by the concentration gradient. An example of a QSPR model, can be derived from a generalised form of the Potts-Guy equation [77], given as,

$$\log k_{sc} = a + b \log P - c\, MW, \tag{2.1}$$

where a, b and c are estimated using regression methods, MW is the compounds molecular weight, and $\log P$ is the partition coefficient. The equation incorporates the essence of diffusion within the SC: an inverse relationship between molecular volume and its diffusivity. A molecule's theoretical maximum diffusivity was calculated, and was used in conjunction with a function based on the molecular volume and octanol water coefficient, k_{ow}, to predict a molecule's permeability. This could be used to derive a diffusion coefficient through a SC with thickness h_{sc}. The diffusion coefficient was calculated as follows,

$$D = D_0 e^{-\beta V}, \tag{2.2}$$

where V is the estimated molecular volume of the permeant, D_0 is the diffusivity through water and β could be determined by fitting to experiments.

Johnson et al. proposed that transdermal drug delivery, for the most part, occurred via the intrakeratinocyte lipid domain [78]. The authors assumed that the intrak-

eratinocyte lipid is anisotropic, such that molecules pass through at different rates in different directions, but the domain is arranged in such a way that molecules can pass through the SC without having to cross the lipid head group region [27]. A lateral diffusion coefficient was calculated as a function of a molecule's permeability, k_{sc}, which in turn, was calculated as a function of the molecule's octanol water coefficient ($k_{sc} = k_{ow}^{\beta}$). By performing a regression analysis on data from 120 human skin permeability measurements, β was determined. A strong relationship was found between molecular weight and ability to permeate the SC. It was concluded that the lateral diffusion was sufficient to explain the resistance to permeation through the SC. Where k_{sc} is the permeability through the SC, and 0.36cm is derived by multiplying the thickness of the stratum corneum by the effective tortuosity of the stratum corneum, the diffusion coefficient through the SC is given as,

$$D_{lat} = \frac{k_{sc}}{K_{o/w}^{0.76}}(0.36\,\mathrm{cm}). \tag{2.3}$$

A different approach was taken by Mitragotri, who instead proposed an equation to describe solute diffusion lipid bilayers using scaled particle theory [79]. Scaled particle theory is a statistical mechanical descriptive device for the fluid phase of a model in three dimensions [80]. The model allows for molecules to diffuse in all directions within the lipids, and an averaged displacement between the three directions was calculated. A diffusion coefficient can be calculated based upon the work required to create a free volume required for diffusion, by calculating the conditional probability density that a path exists between two points in the direction of diffusion and is

of the critical path length required for solute diffusion. Mitragotri predicted that solutes' partition coefficients in the intrakeratinocyte lipids are similar to those that are measured in isotropic solvents, such as octanol. They could therefore use the ratio of a molecule's solubility in octanol and water, $K_{o/w}$, along with the solute radius, r, to predict permeability as,

$$k_{sc} = 5.6 \times 10^{-6} K_{o/w}^{0.7} e^{-0.46r^2}. \tag{2.4}$$

Perhaps the most comprehensive approach is provided in a series of papers by Wang et al. [51, 52]. In the first of the two publications, Wang et al. introduced a model which incorporated more realistic keratinocyte shape, anisotropic lipid phase diffusion, and allowed for molecules to permeate through the keratinocytes. Transport properties were defined for diffusion through the intrakeratinocyte lipids, keratinocytes, as well as transfer between the phases, proportional to the partition coefficient. The inclusion of keratinocyte phase transport is particularly important for hydrophilic compounds, which transport poorly through the lipid layers. In the second of the two papers, the model is then fully parametrised using both experimental data and fundamental transport theory. This led to a model which could predict permeability for both small and large molecules through partially and fully hydrated SCs. Where $(k_{sc})^{comp}$ is the dimensional SC permeability (calculated as a function of diffusion and partition coefficients of water, corneocytes and lipids) as described by Wang et al. [51, 52], and h_{sc} is the thickness of the stratum conreum, the diffusion coefficient through the

SC is given as,

$$D_{sc} = \frac{(k_{sc})^{comp}(h_{sc})}{K_{sc/w}}. \tag{2.5}$$

Diffusion coefficients for acetaminophen (APAP) were calculated using each of the methods shown below in Table 2.1, to assess the difference between each of the models. For the simulations within this chapter, we used the model described by Wang et al. [51, 52]. The authors used the most comprehensive approach based on fundamental transport theory calibrated with existing experimental data. This contrasts with the other authors that either used mechanistic or empirical methods, rather then a combination like Wang's method.

Author	Method used	D_{sc} ($cm^2\ s^{-1}$)
Potts & Guy [77]	Re-arrangement of quantitative structure-activity relationship (QSAR) equation.	1.6843×10^{-9}
Johnson et al. [78]	Lateral diffusion coefficient via the intracellular lipid matrix with no permeability through the keratinocytes.	4.7892×10^{-9}
Mitragotri [79]	Scaled Particle Theory.	1.6792×10^{-9}
Wang et al. [51, 52]	Multiphase, trapezoidal brick and mortar model parametrised using experimental data and fundamental transport theory.	1.3931×10^{-10}

Table 2.1: The diffusion coefficients from four different models for APAP across the Stratum Corneum.

2.3.2 Calculation of diffusion coefficients for the rest of the viable epidermis and dermis

Within the rest of the viable epidermis, we need to define diffusion coefficients for the stratum granulosum, the extracellular fluid, discrete cells, and the transfer between

the extracellular fluid and cells. Nitsche et al. [53] calculated a multiphase diffusion model for the viable epidermis, by treating the epidermis as a hexagonal array of cells bounded by 4-nm-thick, anisotropic lipid bilayers, separated by 1-mm layers of extracellular fluid. Diffusion via the extracellular fluid was assumed to be the bulk aqueous diffusion, D_{aq}, reduced by a hindrance factor, $H^{ext} = 2$, which represents the reduced mobility through extracellular space [81], and is given as,

$$D_{ext} = D_{aq}/H_{ext}. \tag{2.6}$$

Nische et al. [53] also calculated effective diffusion coefficients for the epidermis. They provide three equations, which describe effective diffusion coefficients for hydrophilic and lipophilic molecules. These are calculated as a function of the diffusion coefficient through water, and a hindrance factor. The hindrance factor arises from a molecule's tendency to diffuse via either cytoplasm (H_{cyt}), extracellular fluid (H_{ext}) or via the lipid matrix depending upon the molecules lipophilicity. Like in Equation 2.6, diffusion coefficients are calculated as a function of bulk aqueous diffusion reduced by a hindrance factor. For highly lipophilic permeants, the following relationship for diffusion through the granular layer is given,

$$D_{gran} = D_{aq}/H_{cyt}. \tag{2.7}$$

This suggests that displacement through the epidermis is dependent on mobility through cytoplasm. The same calculation can be used to calculate the diffusion

coefficient through the cytoplasm, D_{intra}. For larger, hydrophilic permeants, within the granular layer, the following relationship for diffusion is given,

$$D_{gran} = D_{aq}/H_{ext}. \tag{2.8}$$

A series of papers by Menochet et al. [82, 83] described a method for calculating a *passive diffusion clearance* for a xenobiotic, as a function of its $\log D_{7.4}$. A molecule's $\log D_{7.4}$ describes the partition coefficient at a specific pH value (in our case, 7.4). For non-ionisable compounds, this is equal to the $\log P$. For ionisable compounds, the $\log D_{7.4}$ will be altered by pH, as the distribution of charged and uncharged forms would change. Although the paper focuses on hepatocytes, it may be assumed that hepatocytes and keratinocytes share similar lipid bilayers, and therefore the passive diffusion clearance term may adequatly describe passive diffusion for keratinocytes. The relationship between *passive diffusion clearance* and $\log D_{7.4}$ is given as follows,

$$\log(P_{diff}) = 0.6316 \log D_{7.4} - 0.3143. \tag{2.9}$$

However, the units for this term are μL/min/10^6cells, whereas our model requires units of either [unit of area/unit of time], or [1/unit of time]. A recent publication by Leedale et al. [84] describes a method of modifying P_{diff}, in order to define a permeability coefficient Q, which is also a function of the cell radius, R. An assumption is made that the cells are spherical, and therefore, the rate of change of the amount

in the cell, A_{cell}, is calculated by integrating over the surface of the cell to get,

$$\frac{dA_{cell}}{dt} = 4\pi R^2 Q C_0 = \frac{P_{diff} C_0}{10^6}, \tag{2.10}$$

where C_0 is the extracellular concentration, which cancels when utilising Eq 2.9 to get,

$$Q = \frac{1}{10^6} \frac{10^{0.6316 \log D_{7.4} - 0.3143}}{4\pi R^2}. \tag{2.11}$$

As the stratum corneum and, more generally, the epidermis are the principal barriers for transdermal delivery, little effort has been spent investigating diffusion coefficients through the dermis as it was assumed that, if a substance may permeate the upper layers of the epidermis, it will reach the dermis and enter systemic circulation. In a number of models, this often leads to the lower layers of the epidermis and dermis being modelled as a single, homogeneous medium. In a geometrically complex, non-homogeneous model such as ours, it is important to define each of the unique regions with their own parameters, to more accurately represent human skin. The composition of the dermis is largely collagen [85]. Therefore, we calculate the diffusion coefficient in the dermis, D_{derm}, by looking at methods for deriving diffusion coefficients for collagen within the literature. Such work has been done by Ramanujan et al. in which diffusion coefficients for collagenous gels were calculated [86]. Permeability was measured by assessing the flow rate through the collagen gels. The

diffusion coefficient was calculated as follows,

$$D_{derm} = \frac{D_0 \alpha}{1 + \left(\frac{R_h^2}{K}\right)^{0.5} + \frac{1}{9}\left(\frac{R_h^2}{K}\right)}, \tag{2.12}$$

where α is the pore radius (calculated to be 5.25×10^{-7} cm), R_h represents the particle radius, K is permeability calculated as function of pore size and porosity, and D_0 is calculated using the Stokes-Einstein relation given as,

$$D_0 = \frac{k_B T}{6\pi\mu R_h}, \tag{2.13}$$

where k_B is the Boltzman constant, T is temperature in Kelvin and μ is the viscosity of water.

2.3.3 Partition coefficients

As shown in Sections 2.3.1 and 2.3.2, a compound's partition coefficient is one of the significant predictors of its diffusivity; however, we must also utilise partition coefficients in order to construct our boundary conditions to ensure the model does not tend towards a homogeneous state. Without partition coefficients, a boundary condition between two regions A and B may be,

$$C_A = C_B. \tag{2.14}$$

However, due to the scale of the model and diffusion coefficients, this will lead to a homogeneous state when steady state is reached, as previously mentioned. Instead, we

use a boundary condition similar to that used by Dancik et al.[87], which incorporates the partition coefficient by setting the concentration at the boundary between two regions, A and B, to be proportional to their partition coefficents, K_A and K_B, given as,

$$\frac{C_A}{K_A} = \frac{C_B}{K_B}. \tag{2.15}$$

In general, partition coefficients are calculated relative to a common phase, which is typically water. It is essential for boundary conditions like shown above, that each of the partition coefficients are calculated relative to the same common phase. In order to incorporate this into COMSOL, we set the boundary, by re-arranging Eq 2.15, to the following,

$$C_A = \frac{C_B K_A}{K_B}. \tag{2.16}$$

In order to implement Eq 2.16, we must estimate the partition coefficients for a drug in the stratum corneum, the rest of the epidermis, the dermis, and the molecule's vehicle. Diffusion through the stata corneum predominately takes place either via the lipid phase or via the corneocytes. Therefore, a partition coefficient may be calculated by incorporating the partition coefficients (K_{lip}, K_{cor}) and the volume fraction of these individual phases (ϕ_{lip}, ϕ_{cor}).

$$K_{sc} = \phi_{lip} K_{lip} + \phi_{cor} K_{cor}. \tag{2.17}$$

Dancik et al. [87] claimed that the partition coefficient for unbound, non-ionized solutes for the epidermis and dermis are equal, and may be calculated as,

$$K_{de} = K_{ed} = \phi_{aq}/f_{non/vt}, \tag{2.18}$$

where ϕ_{aq} is the aqueous volume fraction accessible to the solutes, which was found to be equal to 0.6 after fitting to data [87], and $f_{non/vt}$ is the fraction of non-ionized solute in the viable tissues, calculated as follows,

$$f_{non/vt} = \frac{1}{1 + 10^{7.4-pKa}}. \tag{2.19}$$

Finally, the partition coefficient of the vehicle in pure water is calculated from the fraction of non-ionized permeant in the vehicle,

$$K_v = \frac{1}{f_{non/veh}}, \tag{2.20}$$

where $f_{non/veh}$ may be calculated from the vehicle pH and input pKa as,

$$f_{non/veh} = \begin{cases} \frac{1}{(1+10^{pH-pKa})}, & \text{weak acid,} \\ \frac{1}{(1+10^{pKa-pH})}, & \text{weak base.} \end{cases}$$

Alternatively, if the vehicle is volatile (e.g. ethanol, or acetone) then the partition coefficient may be calculated by assuming there is no vehicle, instead utilising the

permeant's density, ρ, and solubility in water, S_w, to give,

$$K_v = \rho / S_w. \tag{2.21}$$

2.3.4 Boundary conditions on the SC/DP interface

As described in Section 2.3.3, the movement of the modelled compound between one layer of the skin and another was modelled as a continuity of flux, where movement is driven by the concentration gradient, and the partition coefficients of the two layers. Due to there being no inherent boundary between these layers, instead there is a change in physiological properties, it is a reasonable method for modelling these interfaces, and has been used in a number of publications including work by Dancik et al. [54, 55, 87]. It is well understood that the SC is the primary barrier in minimising water loss from the body and preventing the permeation of xenobiotics. This is due to the densely packed, lipid-protein matrix that exists within the SC. The protein filaggrin has been shown to exist in abundance in the SC, and has been associated with the barrier properties [56]. Mutations in the gene encoding filaggrin have been associated with a number of skin diseases, and reduced barrier function. It is therefore necessary that we account for this barrier-like property by modifying the boundary condition on the SC/DP interface. We propose the following boundary condition,

$$-D\frac{\partial C}{\partial x} = k_{sc}\Big(C_v^* - \frac{C_{sc}}{k_{sc}}\Big), \tag{2.22}$$

where k_{sc} is the permeability through the SC which is dependant on the thickness of the SC, and is caclculated as described in Equation 2.4, C_{sc} is the concentration in the stratum corneum, k_{sc} is the partition coefficient for the stratum corneum and C_v^* is defined as follows,

$$C_v^* = \frac{C_{sat} C_v}{C_v + K_m}, \tag{2.23}$$

where C_{sat} is the maximum concentration within the SC, C_v is the concentration in the vehicle and $K_m = C_{sat}/Z$, where Z is some constant to be decided later. Permeability constants were generally the accepted method for estimating delivery through the SC, prior to the development of more computationally intense methods in more recent years, which instead rely upon diffusion coefficients. Equation 2.4 relates a solutes octanol water partition coefficient $K_{o/w}$ along with its approximate atomic radius in order to approximate permeability. As K_m is an artificial parameter, designed to control the slope of C_v^*, a better approximation may be made by fitting to experimental data. Dancik et al. [87] relates C_{sat} to the partition coefficient in the SC, $K_{sc/w}$, as calculated in Section 2.3.3, to the solute's solubility in water S_w through the following relationship,

$$C_{sat} = K_{sc/w} S_w. \tag{2.24}$$

We may arrive at this equation naturally by understanding that $K_{sc/w} = C_{sc}/C_w$, when the two states are in steady state. At maximum solubility, we may instead have $K_{sc/w} = C_{sat}/S_w$, which re-arranges into Equation 2.24. As described by Dancik et al. [87], C_{sat} is a lower bound of the solubility in the stratum corneum; however, no

changes should be made to the value without experimental data to validate. Where no experimental value of S_w is known, it may be estimated at 25^oC using a method proposed by Jain and Yalkowsky [88],

$$\log S_w = 0.5 - \log K_{o/w} - 0.01(T_m - 25), \tag{2.25}$$

where T_m is the melting point of the permeant. A correction to solubility may be made if there is a difference between the temperatures of the permeant when applied, T_1, and the surface temperature of the skin T_2, through the following relationship,

$$S_w(T_2) = S_w(T_1) \times 10^{[0.01(T_2 - T_1)]} \tag{2.26}$$

Finally, as the relationship from Eq 2.25 has units mol/L, we must convert to g/L for use in Equation 2.24.

In order to understand how the various parameters within the saturation function, C_v^*, affect the overall distribution in the skin, we may perturb these parameters. We chose to model cinnamyl alcohol, with an initial concentration in the donor phase of 191 mM, as it is a chemical we will investigate further later on in the chapter. We begin by perturbing the maximum concentration, C_{sat} between 20 and 200 mol/m^3. Figure 2.5 shows the effect of changing C_{sat} on the distribution of cinnamyl alcohol in the various layers of the skin. For all values of C_{sat}, quasi-steady-state is reached in the SC quickly. This steady-state concentration within the SC is driven by C_{sat}, as well as the partition coefficients of the various layers. An increase in C_{sat} also

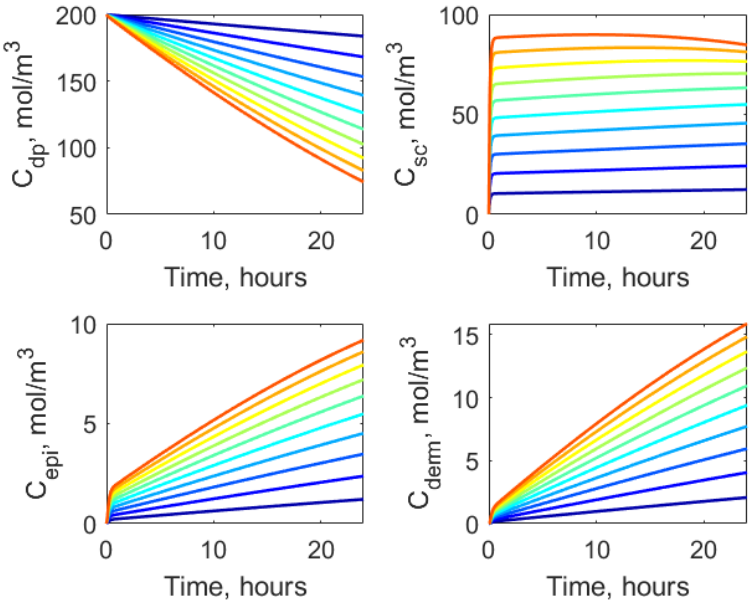

Figure 2.5: Time-dependent, spatially averaged concentration of cinnamyl alcohol in the donor phase, stratum corneum, epidermis and dermis with varying values of C_{sat}. The values of C_{sat} are linearly spaced between 20 mol/m^3(blue), and 200 mol/m^3(red).

increases the concentration within both the epidermis and dermis. This is due to both the increase in flux on the DP/SC boundary, and an increase in concentration gradient at the SC/epidermis boundary.

Figure 2.6 shows the effect of changing the value of Z on the distribution of cinnamyl alcohol. The effect on changing Z has far less impact when the concentration in the donor phase is greater then the maximum concentration in the SC. This is because Z controls K_m, which controls the slope of the curve. However, changes in Z does have a small effect on C_v^* at all concentration of C_v sampled in Figure 2.6. The change in C_v^* will in turn, have an effect on the concentration gradient on the DP/SC boundary, therefore altering the flux, and the concentration in all layers of the skin.

Figure 2.7 shows the effect that varying the permeation constant, P_{sc}, has on the distribution of of cinnamyl alcohol. It is clear that a small value of P_{sc} decreases the

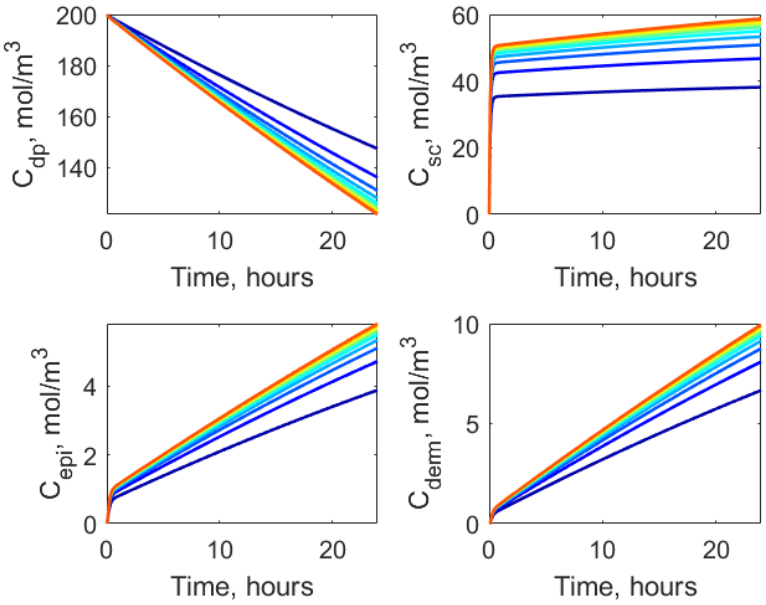

Figure 2.6: Time-dependent, spatially averaged concentration of cinnamyl alcohol in the donor phase, stratum corneum, epidermis and dermis with varying values of Z. The values of Z are linearly spaced between 2 (blue), and 10 (red).

concentration in all layers of the skin. However, increasing the value of P_{sc} beyond 1×10^{-7} m^2/s has very little effect on the amount of chemical permeating into the skin. This would suggests that P_{sc} is a sensitive parameters up to the point where the concentration in the SC reaches maximum concentration imposed by C_{sat}.

2.3.5 Metabolism

The presence of various phase II metabolising enzymes within the lower layers of the skin is well known [89]. Depending on a chemical's ability to permeate the skin, and the concentration at which is reached in the lower layers of the skin, we may, or may not require metabolism terms. Chemicals which pass through the skin quickly may be subject to metabolism at levels which are negligible. However, for chemicals which pass through more slowly, it may be important to account for the various metabolism

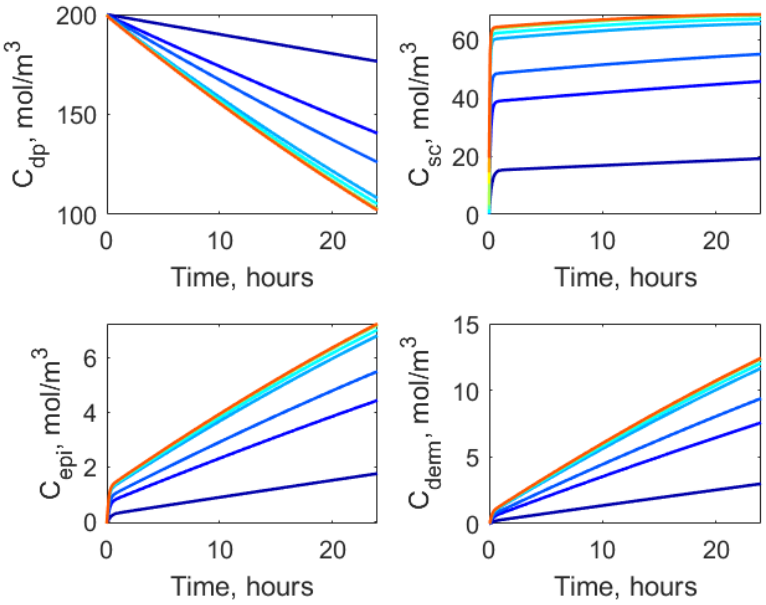

Figure 2.7: Time-dependent, spatially averaged concentration of cinnamyl alcohol in the four compartments with varying permeation constant, P_{sc}. Values were sampled between 1×10^{-9} m/s (blue) and 5×10^{-5} m/s (red). The permeation constant is a key parameter in the dictating the total flux into the SC up to a point, at which the concentration in the SC reaches C_{sat}.

pathways. One issue is the lack of data on the concentration of these various enzymes within the skin. However, for the liver these values are well documented. In order to relate the two, we begin by assuming that Michaelis-Menten kinetics is an adequate representation of the metabolism, where the V_{max} and K_m values are known for each of the metabolising enzymes within the liver. Furthermore, we know that V_{max} is related to the catalytic rate constant, k_{cat}, and the initial concentration of the enzymes, $[E]_0$, by the following,

$$V_{max} = k_{cat}[E]_0.$$

If we therefore assume that k_{cat} remains constant, we can relate our V_{max} in the liver and skin, by simply scaling by the ratio of enzyme concentrations. Where the

concentration of the enzymes is unknown within the skin, we may instead turn to the gene expression values relative to the liver. Figure 2.8 shows the relative fold decrease in gene expression in the skin when compared to the liver.

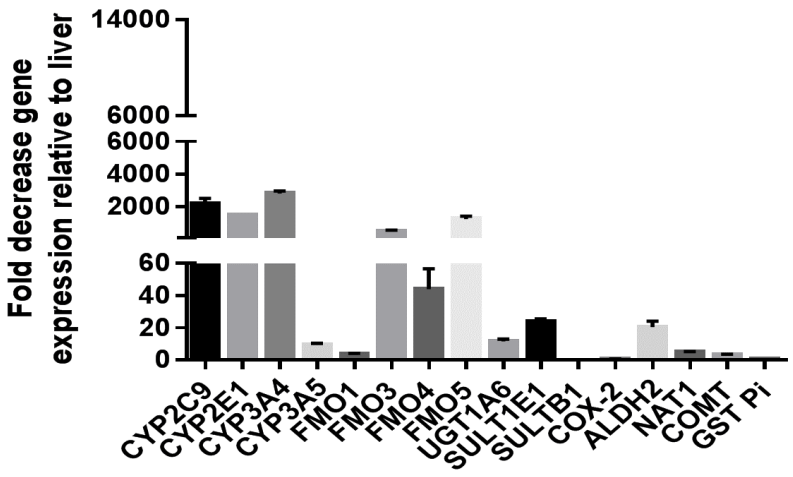

Figure 2.8: Unpublished data on the relative fold decrease in gene expression for a number metabolising enzymes preasent in both the skin and liver, provided by collaborators at the University of Sheffield.

2.4 Model validation

In order to assess the ability of the model to predict the spatial distribution of xenobiotics, we must benchmark against *in-vitro* data for a number of different chemicals which cover a range of physico-chemical properties. However, data sources within the literature are scarce, with very few authors choosing to accompany their models with data. Fortunately, a paper by Davies et al. [29] was accompanied by data describing the distribution of 13 different chemicals at six time points across a 24 hour peroid. The author's experiment looked at the concentration of these chemicals in three skin regions: the stratum corneum, the epidermis and the dermis. As well, two regions at

opposite ends of the skin: the donor phase, above the stratum corneum which is the source of the compound, and the receptor fluid, which is the region under the dermis. In order to relate the model to the data, we must account for the two non-skin regions, and alter our geometry. One limitation of this data source, is the majority of the compounds modelled are skin sensitisers, that is, they irreversibly bind to proteins in the skin. This can lead to a higher concentration of the sensitizing compound in the upper layers of the skin, which will not reduce over time like non-sensitizing compounds. Much time has been spent by various groups of researchers developing *in-silico* models to predict compounds that potentially could be sensitizers, and to which degree these compounds will bind [90, 91]. While these models are improving, there is still much work to be done to be able to quantify if, and to which degree compounds will sensitize the skin.

A finite dose of $25\,\mu\mathrm{L/cm^2}$ was applied topically to exposed skin with a surface area of either $0.64\,\mathrm{cm^2}$ or $0.32\,\mathrm{cm^2}$. Converting from μl to $\mathrm{cm^3}$, our dose may be re-written as $0.025\,\mathrm{cm^3/cm^2}$, which leads to a height of 0.025 cm, or $250\,\mu$m. We may therefore create a donor phase geometry with a height of $250\,\mu$m, to model this region. Volume for the receptor fluid isn't explicitly given in the publication, however, the publication describes a flow-through chamber, where the receptor fluid is in constant motion. This ensures that the concentration within the receptor fluid is never greater than the dermis, and therefore ensures that flow out of the skin is not restricted by lack of concentration gradient. As we are not able to account for the receptor fluid motion, we instead set the thickness of the receptor fluid to be large enough, as to never reach steady-state between the receptor fluid and dermis within the time scales

studied. For each of the chemicals, the $\log P$, $\log D$ and molecular weight, MW were collected, in order to calculate diffusion coefficients in the same manner as Sections 2.3.1 and 2.3.2. These properties are summarised in Table 2.2.

Chemical	**log P**	**log D**	**MW**
1,4-Dihydroquinone	0.59	1.36	110.112
MPT	0.99	0.99	208.235
Benzaldehyde	1.48	1.48	106.124
3,4-Dihydrocoumarin	1.89	1.89	148.161
4-Ethylresorcinol	2.32	2.32	138.166
Cinnamic aldehyde	1.9	1.9	132.162
6-Methylcoumarin	2.3	2.3	160.172
Cinnamic alcohol	1.95	1.82	134.178
DNCB	2.17	2.46	202.55
Phenylbenzoate	3.59	2.21	198.221
α-HCA	4.6	4.6	216.324
1-Bromododecane	5.9	5.9	250.228
1-Bromohexadecane	7.68	7.68	305.344

Table 2.2: The 13 chemicals which were topically applied to human skin by Davies et al. [29]. $\log P$ values were taken directly from Davies et al. Molecular weights were taken from PubChem, as were $\log D$ values, where available. If $\log D$ were not available on PubChem, they were instead estimated using ChemSpider (*www.chemspider.com*).

In order to calculate the diffusion coefficient for the dermis (D_{col}), we require an approximation to the radius of each of the molecules. However, these values cannot be found in the literature. It is therefore necessary to estimate the radius for each of the chemical using the following method.

By definition, the molecular weight, MW, is equal to the number of grams of one mole of a molecule with units g/mol. If we additionally know a molecules density, ρ with units g/cm^3, we may calculate the molar volume, V_m, as follows,

$$V_m = \frac{MW}{\rho}, \tag{2.27}$$

which has units mol/cm^3. By utilising Avogadro's constant, and assuming the molecule is spherical, we may approximate its radius by the following,

$$r_s = \left(\frac{3}{4\pi N_a V_m}\right)^{1/3} \tag{2.28}$$

With all the required physico-chemical properties calculated, we are able to calculate the required diffusion coefficients for each of the regions for each of the chemicals, as summarised in Table 2.3. The final step is the inclusion of an evaporation term. A paper by Kasting et al. describes a method for estimating the evaporation of volatile vehicles, such as ketones and alcohols [92]. The evaporation term may be calculated as,

$$k_{evap} = \frac{k_g}{\rho}\left[\frac{P_{vp}MW}{(0.76 \times 10^6)RT}\right], \tag{2.29}$$

where T is the temperature in celsius, R is the gas constant, ρ is the density, P_{vp} is the vapour pressure and k_g is the gas phase mass transfer coefficient found to be 269 for a bench-top and 849 for a fume hood.

For the majority of the chemicals assessed in the Davies et al. paper, the vehicle was a 4:1 mix of acetone and olive oil. We may therefore include the evaporation term found in Eq 2.29, by multiplying k_{evap} by 0.8, to account for the total volume of acetone.

Chemical	$\mathbf{D_{sc}}$	$\mathbf{D_{gran}}$	$\mathbf{D_{intra}}$	$\mathbf{D_{ext}}$	$\mathbf{D_{col}}$
1,4-Dihydroquinone	9.949×10^{-15}	4.1474×10^{-12}	3.1105×10^{-07}	6.431×10^{-11}	8.9103×10^{-11}
MPT	1.4043×10^{-15}	1.2192×10^{-11}	9.1441×10^{-07}	2.7408×10^{-11}	8.887×10^{-11}
Benzaldehyde	1.2692×10^{-14}	3.8977×10^{-12}	2.9233×10^{-07}	6.7911×10^{-11}	8.904×10^{-11}
3,4-Dihydrocoumarin	9.7056×10^{-15}	3.626×10^{-12}	2.7195×10^{-07}	4.2234×10^{-11}	8.8961×10^{-11}
4-Ethylresorcinol	1.8982×10^{-14}	3.8254×10^{-12}	2.869×10^{-07}	4.648×10^{-11}	8.902×10^{-11}
Cinnamic aldehyde	1.2823×10^{-14}	3.6344×10^{-12}	2.7258×10^{-07}	4.9454×10^{-11}	8.8964×10^{-11}
6-Methylcoumarin	1.3179×10^{-14}	3.564×10^{-12}	2.673×10^{-07}	3.805×10^{-11}	8.8941×10^{-11}
Cinnamic alcohol	1.1216×10^{-14}	3.6046×10^{-12}	2.7034×10^{-07}	4.8415×10^{-11}	8.8954×10^{-11}
DNCB	9.2959×10^{-15}	3.692×10^{-12}	2.769×10^{-07}	2.8321×10^{-11}	8.8981×10^{-11}
Phenylbenzoate	7.348×10^{-15}	3.2247×10^{-12}	2.4185×10^{-07}	2.9064×10^{-11}	8.8821×10^{-11}
α-HCA	3.7417×10^{-14}	2.9294×10^{-12}	2.1971×10^{-07}	2.6218×10^{-11}	8.8694×10^{-11}
1-Bromododecane	3.443×10^{-14}	2.9265×10^{-12}	2.1949×10^{-07}	2.2319×10^{-11}	8.8693×10^{-11}
1-Bromohexadecane	2.4534×10^{-14}	2.7048×10^{-12}	2.0286×10^{-07}	1.8325×10^{-11}	8.8579×10^{-11}

Table 2.3: The diffusion coefficients calculated for each of the 13 chemicals used by Davies et al. [29] as described in Sections 2.3.1 and 2.3.2. Units for all diffusion coefficients are m^2/s.

2.4.1 Cinnamic alcohol

Cinnamic alcohol is an organic compound readily found in perfumes and deodorants. Within the data, summarised within Section 2.4, examples of the distribution of cinnamic alcohol may be found for initial concentrations of 192 mM and 1510 mM at six time points across a 24-hour period. A summary of the diffusion coefficients calculated for cinnamic alcohol are shown in Table 2.3, calculated as described in Sections 2.3.1 and 2.3.2. For the boundary condition on the donor-phase/stratum corneum boundary, we are required to calculate a permeability constant, h, as described in Equation 2.22 in Section 2.3.4. The permeability constant is calculated by Equation 2.4, as function of its octanol/water partition coefficient, $K_{o/w}$, and the solute radius, r_s, which can be estimated using Equation 2.28. The largest driver of the total amount of solute which permeates the skin is the permeation constant, P_{sc}, in the flux term on the DP/SC boundary. In order to assess how well our predicted value fits the data, we may perturb this value and calculate an error metric when compared to the data presented in Section 2.4. The chosen error metric is the normalised root mean squared error (NRMSE), defined as,

$$NRMSE = \frac{\mid y - \hat{y} \mid}{\mid y - \mu \mid}, \tag{2.30}$$

where y denotes the data, $\hat{y}$ denotes the model estimate for the corresponding data, and μ denotes the mean of the data. We require a normalised error metric in order to calculate an averaged error for a given parameter as the concentration in the dif-

ferent layers varies. Without the normalised error metric, the result would be heavily weighted towards the donor phase fit, where the concentration is the highest.

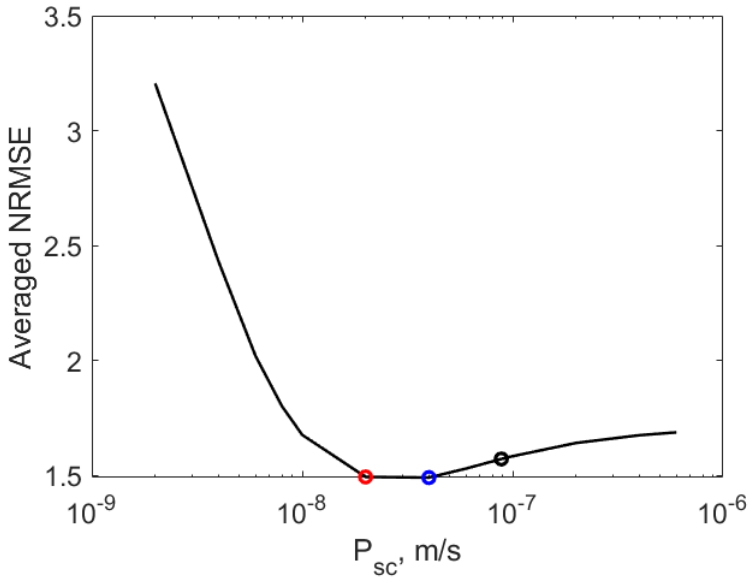

Figure 2.9: The normalised root mean squared error (NRMSE) calculated for 13 different permeation constants, P_{sc}, between the values of 1×10^{-9} m^2/s and 5×10^{-7} m^2/s. Highlighted in red and blue are the permeation constants which minimize the NRMSE, corresponding to the same colour plots show in Figure 2.10. Highlighted in black is the permeation constant which was calculated using Equation 2.4.

Figure 2.9 shows the averages NRMSE for cinnamyl alcohol with an initial concentration of 192 mM. It shows that the values of P_{sc} which minimises the error metric are 2×10^{-8} m^2/s (shown in red), and 4×10^{-8} m^2/s (shown in blue). However, using the predicted permeation constant only increased the error by 5.2%. It is clear from Figure 2.10 there is no single value of the permeation constant which best models the *in-vitro* data in all layers; instead, we see that $P_{sc} = 2 \times 10^{-8}$ m^2/s fits the stratum corneum and epidermis data, while $P_{sc} = 4 \times 10^{-8}$ m^2/s better fits the donor phase and dermis data. One possible explanation may be a difference between the predicted and actual partition coefficients for one or more of the layers. Due to continuity of

flux boundary condition described in Section 2.3.4, compound movement is driven by both difference in concentration and the ratio of partition coefficients for both layers. An alteration in one or more of the partition coefficient would change the flux between layers, therefore changing the concentration in one or more of the layers.

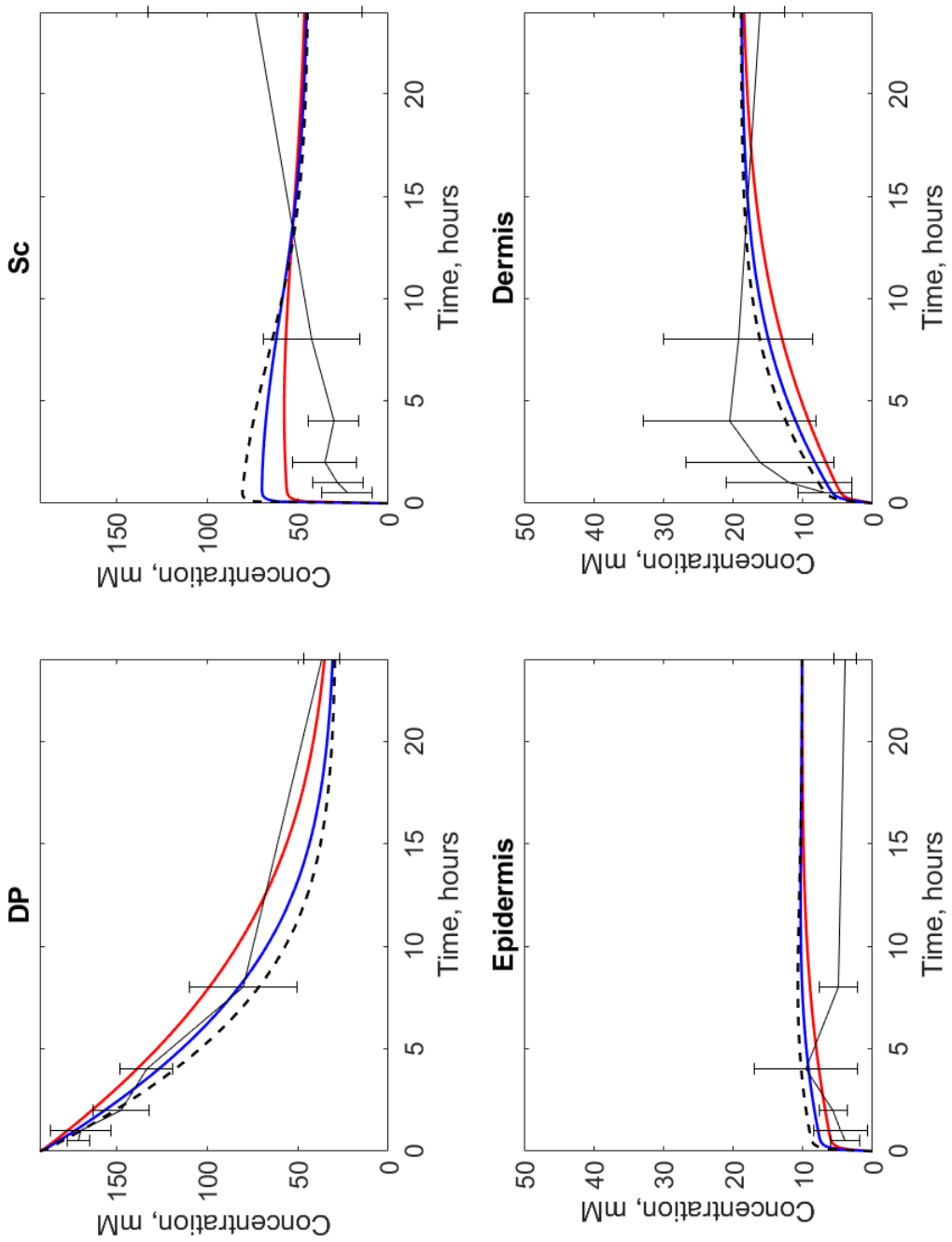

Figure 2.10: The temporal distribution of cinnamic alcohol in the four simulated layers. The red and blue plots correspond to the values of the permeation constant which minimise the NRMSE in Figure 2.9, while the black-dashed plot corresponds to the permeation constant calculated using Equation 2.4.

Next, we again simulate the diffusion of cinnamyl alcohol with an initial concentration of 1510 mM in the donor phase. Like with the lower concentration, we will perturb the value of the permeation constant, calculate the value of the error metric and compare the predicted value.

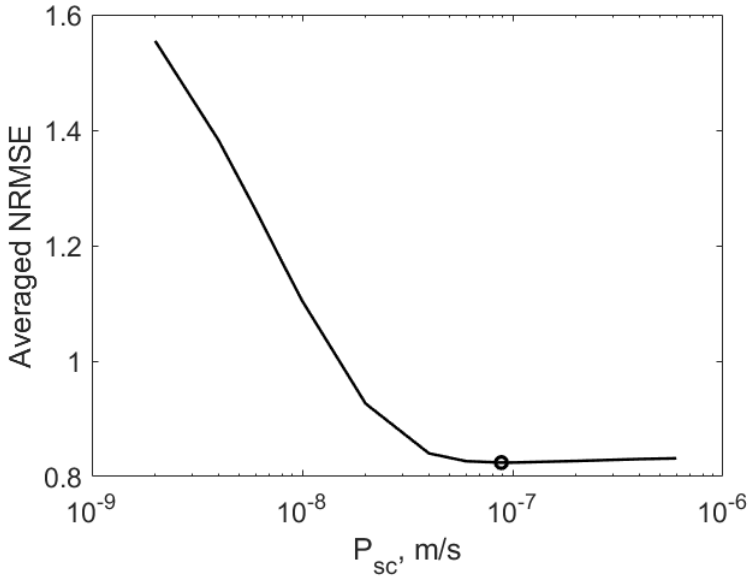

Figure 2.11: The normalised root mean squared error (NRMSE) calculated for 13 different permeation constants, P_{sc}, between the values of 1×10^{-9} m^2/s and 6×10^{-7} m^2/s. The permeation constant calculated using Equation 2.4, and the permeation constant which minimises the NRMSE is highlighted (black circle).

The permeation constant which minimises the error is the value for the 15010 mM concentration, is the value initially predicted. Looking at Figure 2.12, we see a relatively poor fit when compared to the same chemical with a smaller initial concentration in the donor phase. This is due to the maximum concentration imposed on the stratum corneum by C_{sat} in the saturating function on the DP/SC boundary. It is clear that the flux predicted is lower than that observed. Similarly, the maximum concentration observed within the stratum corneum is much higher then predicted. As discussed in Section 2.3.4, the value of C_{sat} is a lower bound, and therefore may be

higher than predicted. Furthermore, as described by Wang et al. [51, 52], there may be variation in the volume fractions of the various phases of the stratum corneum, with the lipid volume fraction, ϕ_{lip}, ranging between 0.0352 for a fully hydrated SC, and 0.11 for a partially hydrated SC. This change in lipid content may explain a change in C_{sat}. Water gradients across the stratum corneum have also been reported by both Bouwstra et al. [93], and Warner et al. [94]. This is due to the layers of desquamated cells in the outer layer of the stratum corneum. As described by Pellett et al. [95], this leads to an increased saturation in these layers, which increases the concentration, as it now driven by both the concentration in the vehicle and C_{sat}. This may explain a poorer model fit for the higher concentration of cinnamyl alcohol.

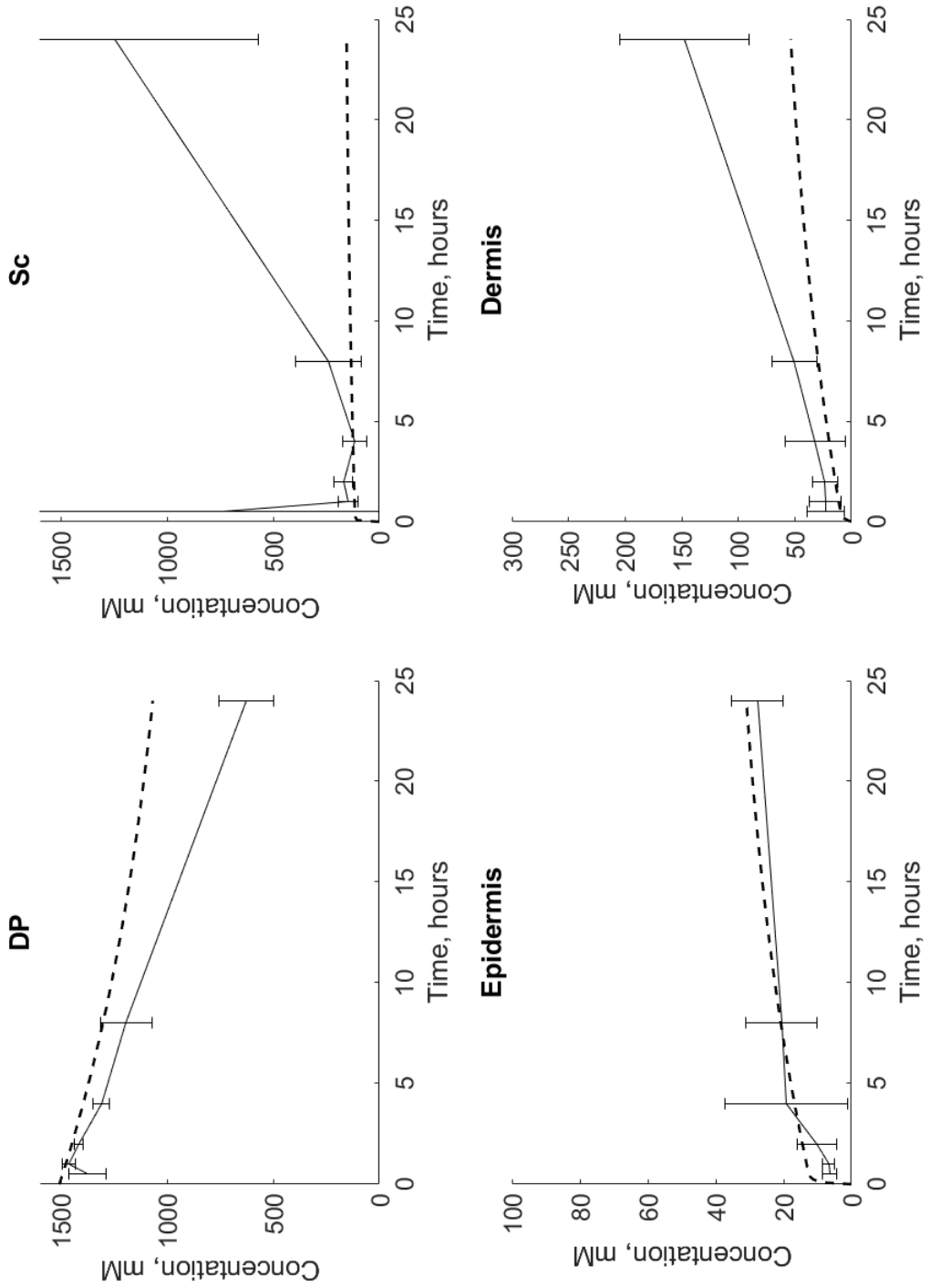

Figure 2.12: The temporal distribution of cinnamic alcohol in the four simulated layers. The black-dashed plot corresponds to the permeation constant calculated using Equation 2.4, which was also the permeation constant which minimised the error.

2.4.2 1-4-Dihydroquione

The next chemical we will validated the model with is 1-4-Dihydroquione, which again will be simulated and compared to *in-vitro* at two initial concentrations. The $\log P$ of 1-4-Dihydroquione, as given in Table 2.2 is 0.59, meaning it will be less soluble in the stratum corneum and lower layers in the epidermis when compared to cinnamic alcohol in the previous section. This results in a lower value for C_{sat}, and reduced diffusion coefficients when compared to cinnamic alcohol.

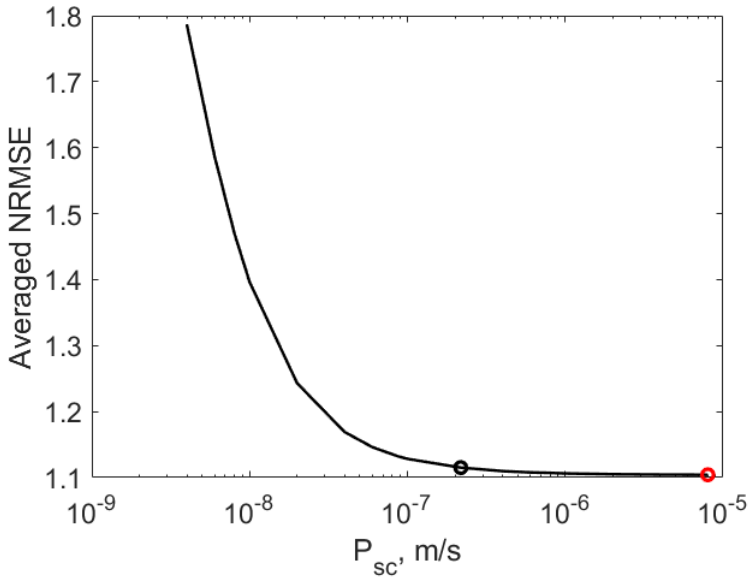

Figure 2.13: The normalised root mean squared error (NRMSE) calculated for 18 different permeation constants, P_{sc}, between the values of 1×10^{-9} m/s and 6×10^{-7} m/s for 1,4-Dihydroquinone dosed at 76 mM. Highlighted in red is the permeation constant which minimize the NRMSE, corresponding to the same colour plots show in Figure 2.14. Highlighted in black is the permeation constant which was calculated using Equation 2.4.

Figure 2.13 shows the error calculated for different permeation constants. The value which minimises the error is shown in red, only reduces the error by 1% when compared to the estimated permeation constant. As shown in Figure 2.14, there is very

little change in the dynamics between the two values of the permeation constant. While an increase in the permeation constant should increase the flux on the DP/SC boundary, the maximum concentration within the stratum corneum is still governed by C_{sat}, which is low for this chemical due to its reduced lipophilicity. Therefore, increasing the permeation constant results in very little change in the concentration in the stratum corneum.

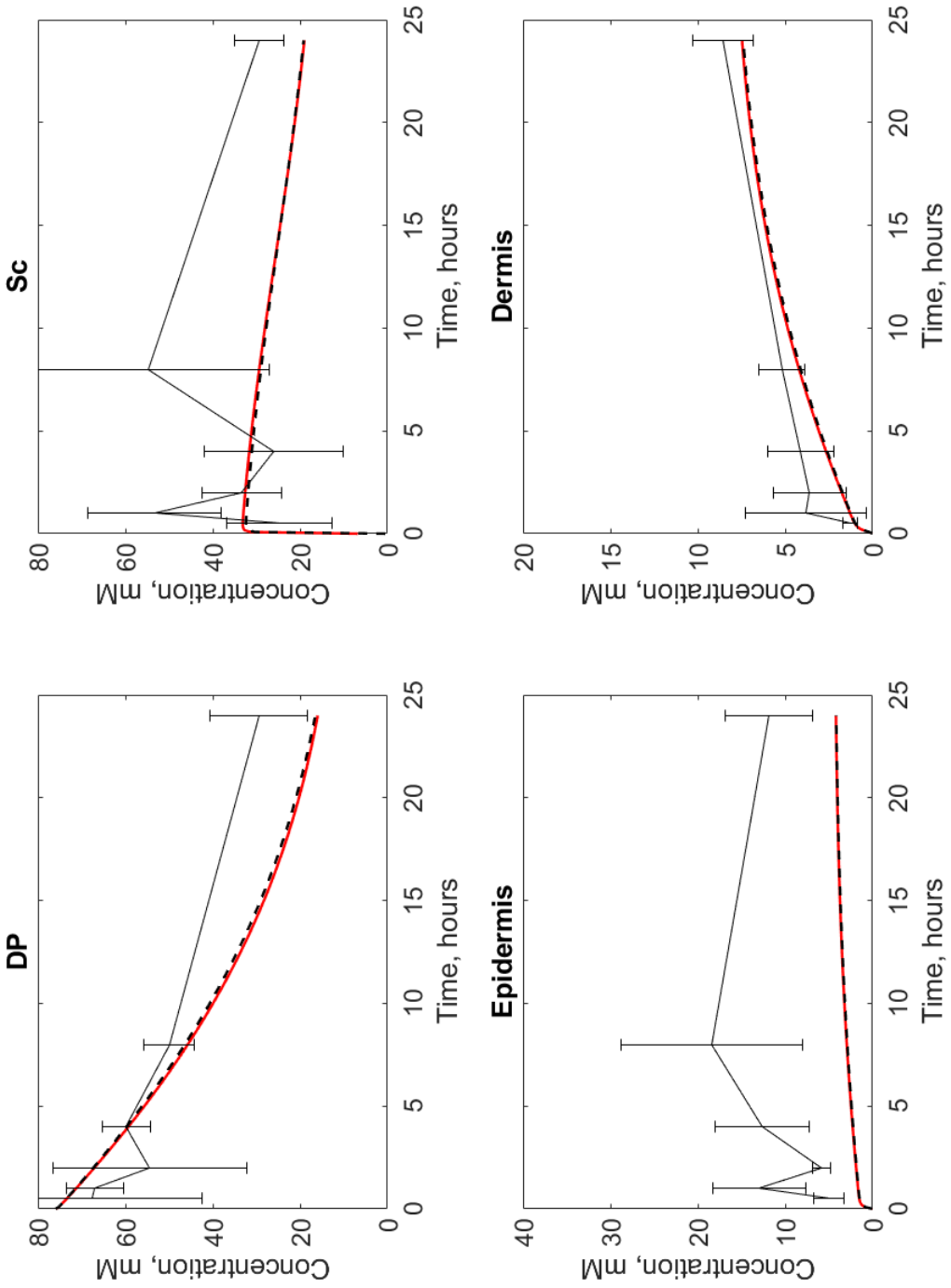

Figure 2.14: The temporal distribution of 1,4-Dihydroquinone dosed at 76 mM in the four simulated layers. The red plot correspond to the values of the permeation constant which minimise the NRMSE in Figure 2.13, while the black-dashed plot corresponds to the permeation constant calculated using Equation 2.4.

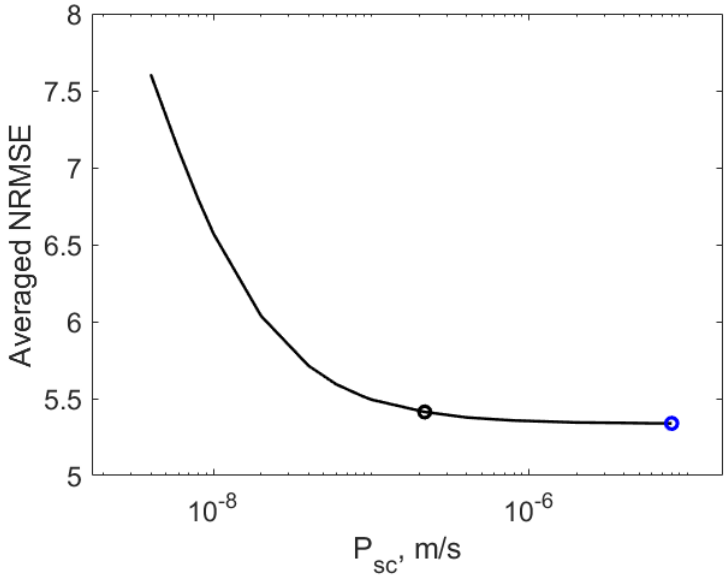

Figure 2.15: The normalised root mean squared error (NRMSE) calculated for 18 different permeation constants, P_{sc}, between the values of 1×10^{-9} m/s and 6×10^{-7} m/s for 1,4-Dihydroquinone dosed at 191 mM. Highlighted in blue is the permeation constant which minimize the NRMSE. Highlighted in black is the permeation constant which was calculated using Equation 2.4.

Figure 2.15 shows very similar results to what was found with the lower initial concentration for the same chemical. While some improvement in error could be found by changing the permeation constant, it only amounted to a 1.01% decrease. This again can be related to very little increase in flux by increasing the permeation constant due to the effect of C_{sat}. The similarities between the distribution of 1,4-Dihydroquinone for the two partition coefficients is shown in Figure 2.16.

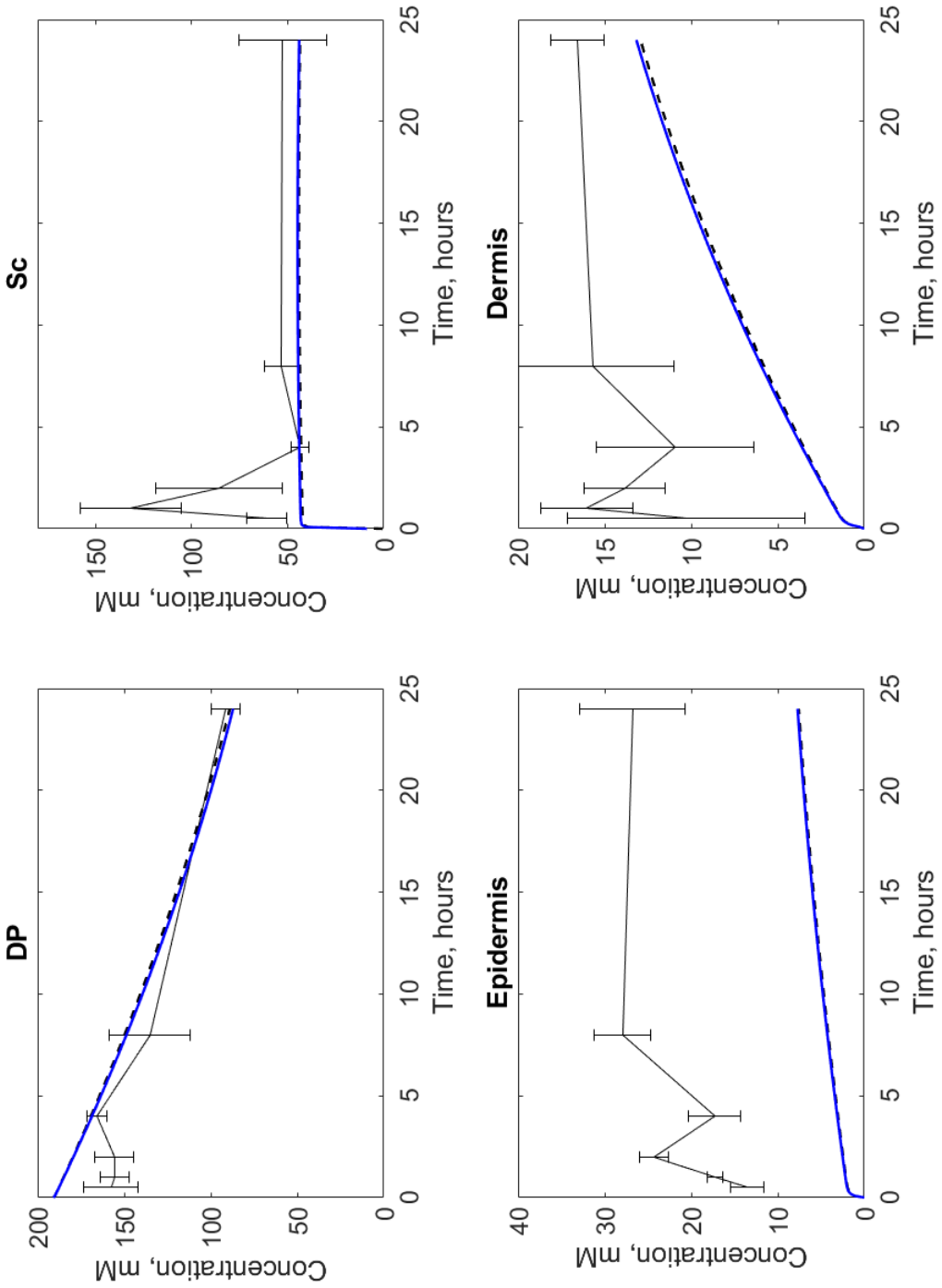

Figure 2.16: The temporal distribution of 1,4-Dihydroquinone dosed at 191 mM in the four simulated layers. The red plot correspond to the values of the permeation constant which minimise the NRMSE in Figure 2.13, while the black-dashed plot corresponds to the permeation constant calculated using Equation 2.4.

2.4.3 2,4-Dinitrochlorobenzene (DNCB)

The final chemical we will simulate in order to validate the model is 2,4-Dinitrochlorobenzene (DNCB), which is commonly used for the treatment of warts, by causing an immune response to the virus responsible [96]. While the log P value of DNCB would suggest that it would be a better candidate for percutaneous absorption, it also has a greater molecular weight when compared to the other chemicals simulated in this chapter, which has been shown to have a negative impact on a compound's ability to permeate the skin [97].

Figure 2.17 and 2.18 show the change in error by perturbing P_{sc}. The error dynamics are very similar to what was found for 1-4-Dihydroquione. It shows small improvements of 0.1046% for the 99 mM simulation and 0.1899% for the 189 mM simulation. Like found with 1-4-Dihydroquione in Section 2.4.2, an increase in the permeation coefficient resulted in very little change for the model dynamics due to the effect of C_{sat} as shown in Figures 2.17 and 2.18. However, the error for this compound is low for both concentrations simulated. This is due to the compounds lipophilicity increasing the solubility in the stratum corneum, paired with initial concentrations close to the estimated C_{sat} value.

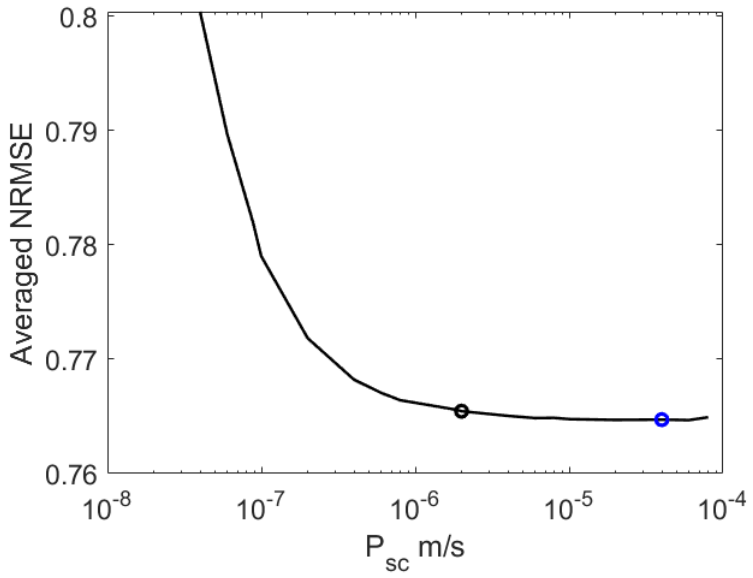

Figure 2.17: The NRMSE calculated for 18 different permeation constants, P_{sc}, between the values of 1×10^{-9} m/s and 6×10^{-7} m/s for 2,4-Dinitrochlorobenzene dosed at 99 mM. Highlighted in blue is the permeation constant which minimises the NRMSE, while in black is the constant initially estimated.

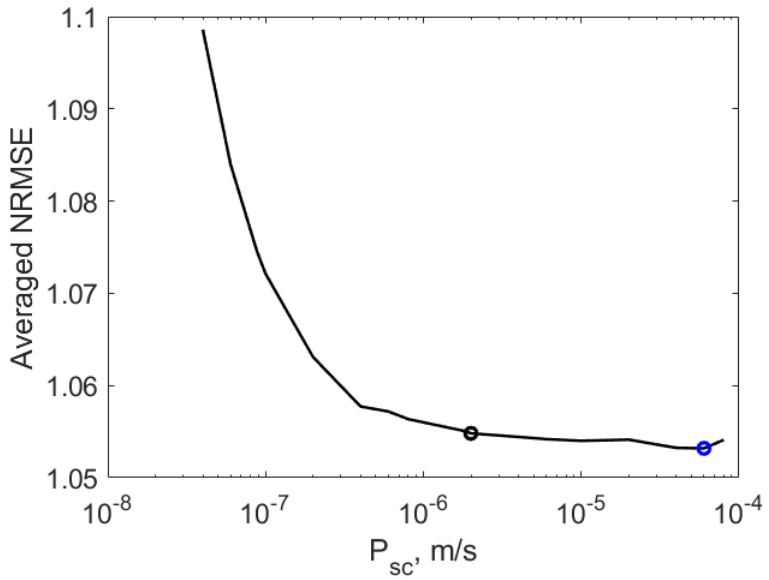

Figure 2.18: The NRMSE calculated for 18 different permeation constants, P_{sc}, between the values of 1×10^{-9} m/s and 6×10^{-7} m/s for 2,4-Dinitrochlorobenzene dosed at 189 mM. Highlighted in blue is the permeation constant which minimises the NRMSE, while in black is the constant initially estimated.

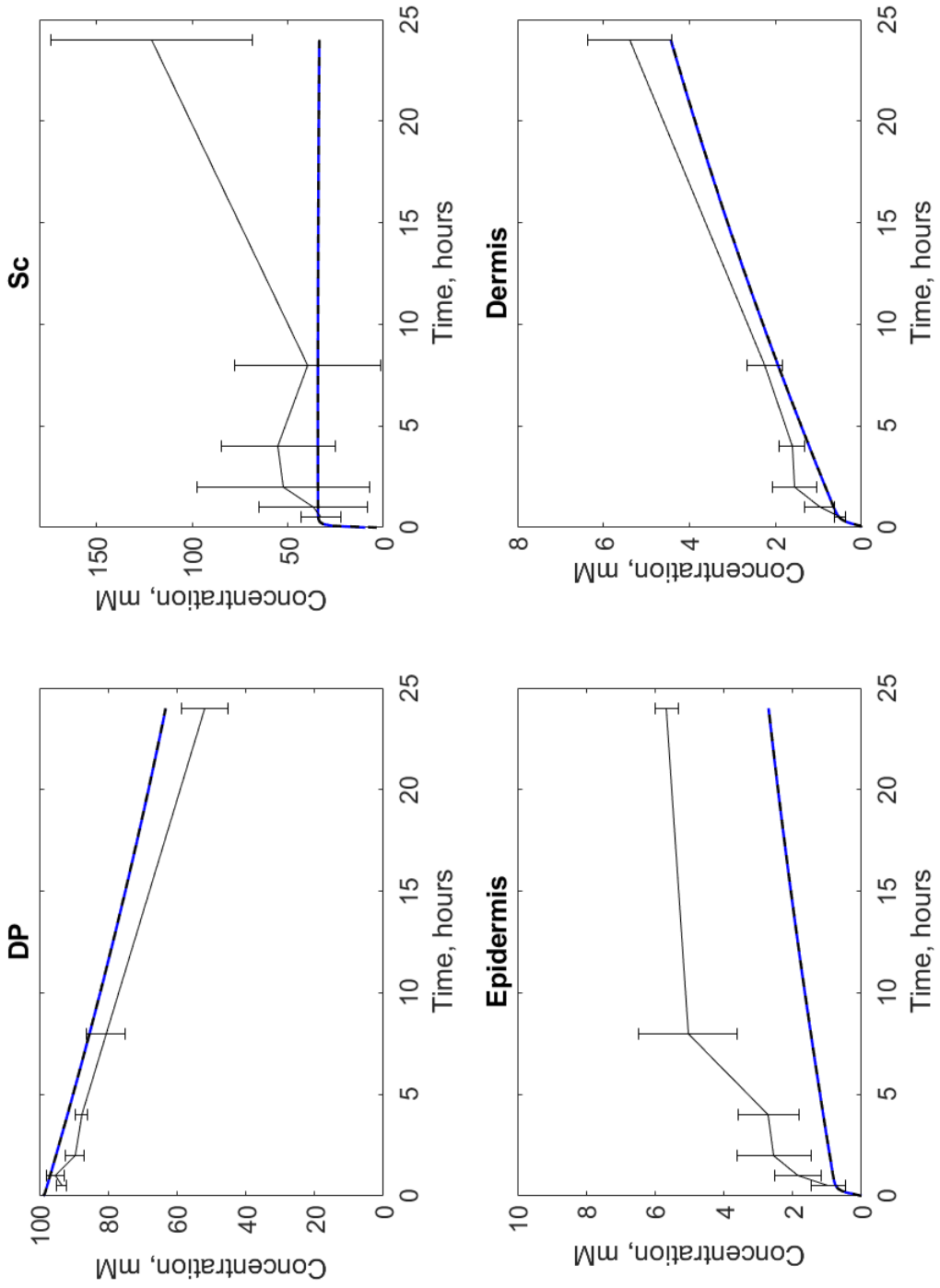

Figure 2.19: The temporal distribution of 2,4-Dinitrochlorobenzene dosed at 99 mM in the four simulated layers. The red plot correspond to the values of the permeation constant which minimise the NRMSE in Figure 2.17, while the black-dashed plot corresponds to the permeation constant calculated using Equation 2.4.

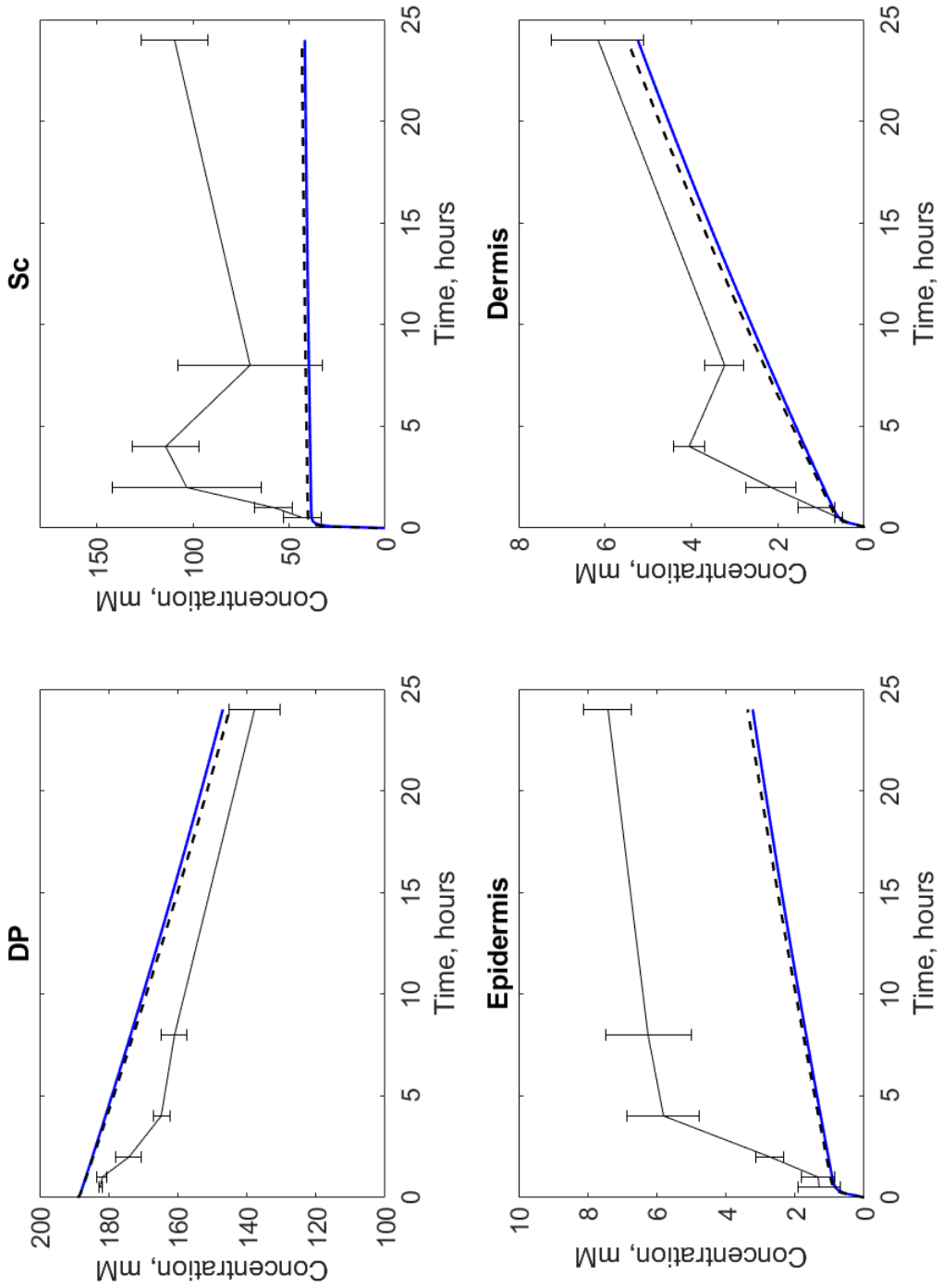

Figure 2.20: The temporal distribution of 2,4-Dinitrochlorobenzene dosed at 189 mM in the four simulated layers. The blue plot correspond to the values of the permeation constant which minimise the NRMSE in Figure 2.18, while the black-dashed plot corresponds to the permeation constant calculated using Equation 2.4.

2.5 Chapter discussion

The advancement of computing power has enabled the development of more complex models that more closely mimic skin physiology. Methods for predicting percutaneous absorption have seen incremental changes from simple permeation models, which predict delivery solely based on a permeation constant, concentration and path length [27]; to compartmental models; to finite-difference approaches to compartmental models [29]. In more recent years, models that are now also dependent on space as well as time have been developed, such as those described in a publications by Kattou et al. [54], and Chen et al. [55]. While these models are a big step forward from the more simple compartmental models of the past, they still fail to include some key features of the skin. These features have a large contribution to the skins ability to act as a barrier: the evolving shape of the keratinocytes, which become flattened, increasing the tortuous path taken by many lipophilic compounds across the skin; the low solubility of many compounds within the stratum-corneum; the barrier property about as a result of the densely packed lipid-protein matrix which exists within the stratum corneum, which includes binding proteins such as filaggrin [56], which reduces the flux across the stratum corneum; and the heterogeneous thickness of the different layers of the skin.

The work within this chapter had three motives: to create a model which encapsulates more of the physiological features of the skin then has previously been published; to predict the spatio-temporal distribution of a compound based solely on its physico-chemical properties; and to fit all *in-vitro* data well, instead of predicting

the distribution of a single compound exceptionally. The use of histology to create the geometry ensured that the tortuous path taken by many lipophilic compounds during transdermal drug delivery is physiologically relevant. It also accounted for the heterogeneous thickness of the different layers found *in-vivo*. For each phase of the model, a diffusion coefficient, partition coefficient, and boundary condition were calculated, based upon previously published models for diffusivity validated against experimental data. This ensured that the model was able to perform well for a variety of different physicochemical inputs.

The model was validated against *in-vitro* data for a variety of chemicals taken from work by Davies et al. [29]. The model was shown to perform well for the initial doses which were close to the estimated maximum stratum corneum concentration, C_{sat}. However, for initial doses with concentrations that were significantly higher than the calculated C_{sat}, the model underperformed. In Section 2.4.1, we discussed a variety of reasons which we believe may contribute to this. These included that C_{sat}, as described by Dancik et al. [87], is a lower bound; however, its value could be greater. It would be difficult to make an adjustment to the value of C_{sat} without any data. The other reason is the saturation of the outermost layers of the stratum corneum, consisting of desquamated cells, which may lead to the concentration in the stratum corneum being greater than C_{sat} due to a high concentration in the vehicle. However, this is difficult to incorporate in our model as it would require the addition of an extra layer within the stratum corneum. There is also uncertainty in the thickness of this desquamated layer, and the layer is unnecessary when modelling compounds where the initial concentration within the vehicle is close to the estimated C_{sat} value.

When modelling *in-vivo* and *in-vitro* set-ups using this model, the problem encountered with high initial concentrations when compared to C_{sat}, would be less of an issue. For use in therapeutic modelling, candidate compounds would be lipophilic with $\log P$ values between 1 and 3 [98], leading to a higher C_{sat} value. Furthermore, pharmaceuticals which are delivered transdermally tend to be potent, with therapeutic doses below 20 mg IV dose/day [99]. When modelling the exposure to chemicals, such as house-hold cleaning products and cosmetics, for the most part, we generally see very small amounts of a compound applied to the skin, and therefore, the concentration in the stratum corneum may not reach C_{sat}.

Chapter 3

Physiologically-based pharmacokinetic modelling

3.1 Background

Physiologically based pharmacokinetic (PBPK) modelling is a powerful, multi compartmental, mathematical method for describing the absorption, distribution, metabolism and excretion (ADME) of substances in living organisms [100]. This is achieved by utilising physiological properties of a chosen organism, such as organ volume and flow rates, as well as accounting for any metabolism or excretion. With knowledge of the composition of different organs, such as the volume fractions of proteins, lipids and water, the concentration of a xenobioitc in different organs may be calculated for its physiochemical properties. This information be used to model the time-dependent distribution of a xenobiotic in the given compartments, representing the various organs/tissues in the body.

PBPK models come in varying degrees of complexity, with simple models following the anatomical structure of the given organism such that each compartment represents a given organ [101]. These organs are often assumed to be homogeneous, well-stirred compartments with transfer between compartments governed by perfusion limited kinetics [102]. In recent years however, there has been a large drive by the pharmaceutical industry to derive more detailed, mechanistic PBPK models, to account for a wide array of biological features and human physiology in drug development and regulatory decision-making [103]. Examples of commercially available PBPK software include *Simcyp PBPK Modelling and Simulation*, *Gastroplus*, and *PKSIM*. These platforms are commonly used by large pharmaceutical companies in all stages of drug development, and are seen to be the gold standard in PBPK modelling today.

PBPK modelling be differentiated from the more traditional pharmacokinetic (PK) modelling through the inclusion of detailed physiological processes, and known physicochemical information about the compounds to be modelled in order to predict complex biological properties [104]. This is of particular importance in the pharmaceutical industry where drug development requires information related to both drug distribution within the body, and the subsequent metabolism. Furthermore, unlike in PK modelling, parameters in PBPK models may have a direct physical or biochemical meaning, which can lead to a more intuitive mechanistic understanding.

A key issue with PBPK modelling is the varying physiological properties of the population. For example, fluctuations in people's weight and size, which leads to varying volumes of organs, varying flow rates, varying enzyme concentration and elimination

rates. This has lead to the developments of population based methods, where physiological parameters are instead described with distributions which span the range of measured values [105, 106]. However, due to the large number of parameters in a typical PBPK model, it can be difficult adequately covering the parameter space.

For a PBPK model with fixed physiological parameters, the xenobiotics physiochemical properties coupled with the anatomical features of the host is what determines its distribution in different organs. The properties include molecular weight, (MW), lipophilicity (measured using partition coefficient, log P), and the acid dissociation constant, (pKa). These values influence the concentration in various compartments. There are numerous examples of PBPK models in the literature which follow similar methodologies, which summarised in a systematic review by Sager et al. [102]. The PBPK model within this chapter is based upon publications by Peters [104, 107]. As with many PBPK models, it is assumed that: each of the tissues are considered to be a single, well-stirred compartment with spatially uniform concentration; and drug distribution is based upon perfusion-limited kinetics. Perfusion-limited kinetics dictate that blood flow to tissue is the limiting process in the model. That is, when in steady state, the drug concentration within circulation and in tissues is at equilibrium, where the concentration is governed by the partition coefficient of the drug in each tissue [108]. An alternate approach, for larger, polar molecules, is permeability limited kinetics, where the limiting factor is permeability across the cell membrane. This requires each tissue to be split into two compartments, representing extracellular and intracellular space. The time taken to reach steady state with permeability limited kinetics, is then a function of a drug's ability to permeate the cells membrane.

There are numerous examples of PBPK models which account for gastric and intestinal absorption, arterial infusion, and intravenous dose as these are the main route for administering therapeutic agents. The complexity of these models varies hugely, from simple models, to models with multiple compartments for single organs with parameter values instead described by distributions. However, while there are examples of PBPK models that account for percutaneous absorption [57, 58, 59, 60, 61, 62], they tend to be developed to model a specific chemical, where complexity in percutaneous absorption is lacking.

3.2 Model parameters

3.2.1 Partition Coefficients in PBPK

Due to the change in physiological properties in organs and tissues found in humans, compounds will have different solubilities in each. Within PBPK, it is generally assumed that the drug may distribute in one of three ways: in the plasma unbound; in the plasma bound; and bound to red blood cells. However, pharmacokinetic parameters are calculated by analysis of drug concentration in the plasma unbound. Therefore, there a number of parameters which describe the distribution in these three phases. The first is the blood-to-plasma concentration ratio, commonly denoted as R, which accounts for the distribution of a drug between plasma and red blood cells. There are a number of drugs that have a greater binding affinity to erythrocytes (i.e. R is greater then 1), for which, clearance may be overestimated if the blood-to-plasma ration is not included. This is because only unbound compound

may be metabolised or excreted. Next, the fraction unbound in plasma commonly denoted as $f_{u(p)}$, describes the fraction of the drug unbound in the plasma. This, along with the unbound tissue partition coefficient, $K_{pu}(t)$, may be used to calculate a tissue-specific partition coefficient, K_p, with the following, $f_{u(p)} \times K_{pu}(t) = K_p$. Subsequently, this may then be used to described the tissue-blood concentration with the following, K_p/R.

Calculation of the tissue specific partition coefficients depend on a number of physicochemical properties including log P, pKa, pH and fraction of free drug in the plasma, as well as tissue specific properties. In separate bodies of work by both Poulin and Thiel [109], and Rodgers and Rowlands [110, 111], tissues are defined in terms of the volume fraction of of water, lipids, and phospholipids. The drug-tissue specific partition coefficient could therefore be calculated as a function of the drugs physicochemical properties, and the volume fraction of the various components of the tissue. Increasing drug-tissue specific partition coefficient would lead to more drug partitioning into the tissue. On the contrary, decreasing the drug-tissue specific partition coefficient would lead to less drug partitioning into the tissue.

3.2.2 Estimating tissue partition coefficients

Partition coefficients in the PBPK model were estimated based upon the work of Rodgers and Rowlands [110, 111]. In order to calculate the partition coefficient, there are a number of physico-chemical properties that need to be known: the acid dissociation constant, pK_a; the base dissociation constant, pK_b; the partition coefficient, $\log P$; the blood plasma concentration ratio, R; and the fraction of unbound

drug in the plasma, $f_{u(p)}$. The partition coefficients can then be calculated using a modified form of the Henderson-Hasselbalch equations,

$$K_{pu} = \left[f_{ew} + \left(\frac{1 + 10^{pK_a - pH_{IW}}}{1 + 10^{pK_a - pH_p}} \times f_{IW} \right) + \left(\frac{K_a [AP^-]_T \, 10^{pK_a - pH_{IW}}}{1 + 10^{pK_a - pH_p}} \right) + \left(\frac{P f_{NL} + (0.3P + 0.7) f_{NP}}{1 + 10^{pK_a - pH_p}} \right) \right], \quad (3.1)$$

where pH describes how acidic or basic the phase is, f denotes the volume fraction of a phase, P describes the antilog of $\log P$, and $[AP^-]_T$ describes the concentration of acidic phospholipids in the given tissue. The subscript ew denotes extracellular water, IW denotes intracellular water, NP denotes neutral lipids, and NP denotes neutral phospholipids. Levels of these various components are reported by Rodgers and Rowland [110]. However, values of K_a in Equation 3.1 are not readily available. One approach is to estimate K_a for the blood cells, by rearranging Equation 3.1. To do so, we must recognise that blood cells do not posses any extracellular space, and therefore $f_{ew} = 0$. The partition coefficient K_{puBC} is the blood cell to plasma water concentration ratio, for which, values are redly available in the literature, or can be measured *in-vitro* from the blood-to-plasma concentration-ratio, fraction of unbound drug in the plasma and hematocrit [112]. This leads to the following,

$$K_{aBC} = \left[K_{puBC} - \left(\frac{1 + 10^{pK_a - pH_{BC}}}{1 + 10^{pK_a - pH_p}} \times f_{IWBC} \right) - \left(\frac{P f_{NLBC} + (0.3P + 0.7) f_{NPBC}}{1 + 10^{pK_a - pH_p}} \right) - \left(\frac{1 + 10^{pK_a - pH_p}}{K_a [AP^-]_{BC} \, 10^{pK_a - pH_{BC}}} \right) \right], \quad (3.2)$$

where the BC subscript denotes the blood cells. The assumption is then made that K_{aBC} is representative of the K_a in all tissues, therefore, by substituting Equation 3.2 in Equation 3.1, we may calculate tissue specific partition coefficients.

3.2.3 Metabolism and excretion

Pharmacokinetics are determined by both the movement of the drug, and distribution throughout the body, as well as how it may be cleared by the body through metabolism and excretion. Generally, the assumption is made that drug metabolism primarily takes place within the liver, due to the nature of the liver being responsible for the first-pass metabolism. Metabolism is generally modelled with a first-order term; however, case-specific examples can be found where the user has tailored the metabolism equation to model specific metabolism pathways through the use of multiple metabolism terms [113, 114].

Renal elimation via the urine is also accounted for in many PBPK models. Like with metabolism, renal elimination is generally modelled with a first order term [115]. This allows the user to account for non-hepatic clearance, which is important for some compounds. The rate of renal clearance is estimated in one of two ways: fitting to PK data to ensure a good fit; or using predictive models. There are a number of examples of models within the literature which may be used to predict renal clearance as a first-order elimination based on the glomerular filtration rate (GMR), which have been summarised in work by Florkowski et al. [116]. More sophisticated models has also been developed, such as work by Neuhoff et al. who created a dynamic model which simultaneously could account for passive permeability, metabolism and various

transport processes [117]. A comprehensive review of the more complex approaches to modelling renal clearance are discussed in a publication by Scotcher et al. [118].

3.2.4 Model development

The basic Peters PBPK model has 16 compartments, and follows the schematic diagram shown in Figure 3.1. Flow rates into, and out of tissue and organs are denoted by Q, while organ volumes are denoted V. Both are followed by a subscript specific to the given tissue or organ.

A summary of each of the flow rates into the organs and tissues, as well as their respective volumes, is given in Table 3.1.

Organ/tissue	**Flow rate, Q, (mL/min)**	**Volume, V, (mL)**
Brain	700	1450
Gut	1100	1650
Spleen	77	192
Pancreas	133	77
Stomach	38	154
Liver	1650	1690
Kindey	1100	280
Heart	150	310
Lungs	5233	1172
Muscle	750	35000
Adipose	260	10000
Skin	300	7800
Bone	250	4579
Thymus	80	29
Hepatic artery	302	-
Arterial blood	-	1698
Venous blood	-	3396

Table 3.1: Description of the flow rates and volumes of each of the tissues present for a human weighing 70 kg, taken from Peters [104].

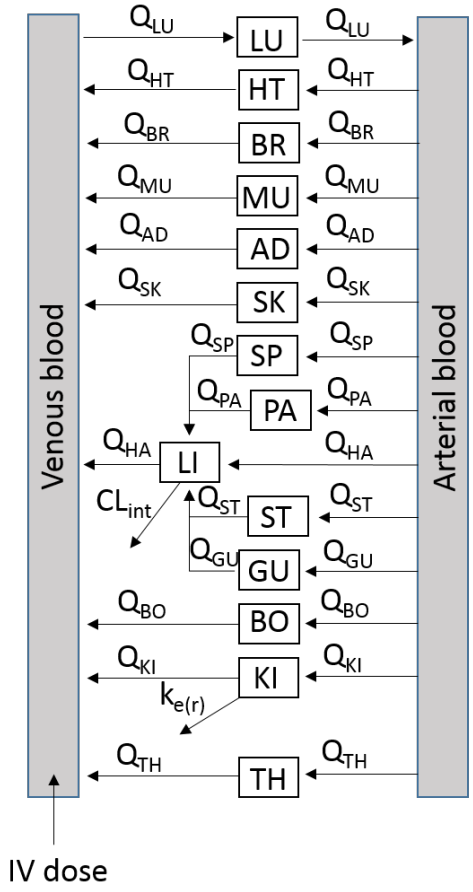

Figure 3.1: Schematic diagram of the basic Peters PBPK model, described in this section. The compartments are as follows: lungs (LU), heart (HT), brain (BR), muscle (MU), adipose (AD), skin (SK), spleen (SP), pancreas (PA), liver (LI), stomach (ST), gut (GU), bone (BO), kidney (KI) and thymus (TH). Flow rates into, and out of an organ are given by Q, followed by the subscript given above.

The rate of change of concentration in the lung, C_{LU}, is calculated as follows,

$$\frac{dC_{LU}}{dt} = \frac{Q_{LU}}{V_{LU}}\left(C_{VE} - \frac{C_{LU} \times R}{f_{u(p)} \times K_{pu(LU)}}\right), \tag{3.3}$$

where R is the blood:plasma concentration ratio, $f_{u(p)}$ is the fraction unbound in plasma, and K_{pu} is the unbound partition coefficient of the lung. The first term represents flow from the venous compartment to the lungs and therefore is positive,

while the second term represents distribution into the tissue, and flow from the lungs to the arterial compartment, and therefore is negative.

The rate of change in the arterial blood compartment is given as,

$$\frac{dC_{AR}}{dt} = \frac{1}{V_{AR}}\left(\frac{Q_{LU} \times C_{LU} \times R}{f_{u(p)} \times K_{pu(LU)}} - \sum Q_j C_{AR} + AIR\right), \tag{3.4}$$

where j represents each of the 13 organs that flow from the arterial compartment, and AIR is the arterial infusion rate, which represents the infusion of drug over a period of time into some artery. The rate of change in venous blood is given as,

$$\frac{dC_{VE}}{dt} = \frac{1}{V_{VE}}\left(\sum \frac{Q_T \times C_T \times R}{f_{u(p)} \times K_{pu(T)}} - Q_{LU} C_{VE} + VIR\right), \tag{3.5}$$

where T represents all organs and tissues, except for the gut, pancreas, spleen, stomach, and lungs, and VIR is the venous infusion rate, which represents a standard IV dose over some given time period. A generalised form can be given for all non-elimating organs, i, except for the stomach, gut, kidney, liver and lungs,

$$\frac{dC_i}{dt} = \frac{Q_i}{V_i}\left(C_{AR} - \frac{C_i \times R}{f_{u(p)} \times K_{pu(i)}}\right). \tag{3.6}$$

Unlike the lung calculation in Equation 3.3, the first term represents flow from the arterial compartment into the tissue, and the second term represents flow from the tissue to the venous compartment. For the stomach, we have,

$$\frac{dC_{ST}}{dt} = \frac{1}{V_{st}}\left[Q_{ST}\left(C_{AR} - \frac{C_{ST} \times R}{f_{u(p)} \times K_{pu(ST)}}\right) + gastric\ absorption\right]. \tag{3.7}$$

Within the Peters model, there are an additional nine gastrointestinal compartments linking the stomach to the colon representing subsequent stages of the intestine, where transfer is modelled using a first order term. Each consist of 4 ODEs for the following variables; amount of undissolved drug, amount of dissolved drug, amount of degraded drug, and amount absorbed. The drug absorbed in the stomach gives us our gastric absorption in Equation 3.7, and the total intestinal absorption, TIA in Equation 3.8, is the sum of the amount absorbed in the subsequent eight compartments. However, as we are interested in transdermal infusion, we may set gastric absorption, AIR, VIR, and TIA equal to 0. For the gut, we have,

$$\frac{dC_{GU}}{dt} = \frac{1}{V_{GU}}\left[Q_{GU}\left(C_{AR} - \frac{C_{GU} \times R}{f_{u(p)} \times K_{pu(GU)}}\right) + TIA\right], \tag{3.8}$$

where TIA is the total intestinal absorption. For the kidneys, we have,

$$\frac{dC_{KI}}{dt} = \frac{1}{V_{KI}}\left[Q_{KI}\left(C_{AR} - \frac{C_{KI} \times R}{f_{u(p)} \times K_{pu(KI)}}\right)\right] - \frac{C_{KI} \times k_{e(r)}}{K_{pu(KI)}}, \tag{3.9}$$

where $k_{e(r)}$ is the renal elimination rate constant. Finally, the rate of change in the liver is given as follows,

$$\frac{dC_{LI}}{dt} = \frac{1}{V_{LI}}\left(Q_{HA} \times C_{ART} + \sum \frac{Q_j \times C_j \times R}{f_{u(p)} \times K_{pu(j)}} - \frac{Q_{LI} \times C_{LI} \times R}{f_{u(p)} \times K_{pu(LI)}} - \frac{C_{LI} \times CL_{int}}{K_{pu(LI)}}\right) \tag{3.10}$$

where j represents the gut, pancreas, spleen and stomach, and CL_{int} is a constant for hepatic metabolism with units 1/min, representing intrinsic clearance.

3.3 Model replication

PBPK models are today one of the key tools in early drug development. One of the key strengths of PBPK models is the ability to make predictions outside a sampled population, therefore reducing uncertainty [119]. This can aid the preclinical stage of drug development by generating a greater understanding of the mechanisms which drive ADME *in-vivo*. The prevalence of PBPK was highlighted by both the European Medicines Agency, and the Food and Drugs Administration in the USA, who both published guidelines on the use of PBPK in drug submissions [120, 121]. It clear from both these sets of guidelines, that model validation is a key aspect in the use of PBPK models. However, the scope of the model validation must correlate with the intended use of the PBPK model. For the prediction of the ADME of a drug, comparison with time-course blood plasma data would suffice, whereas, for the prediction of a new potential drug or chemical, the validation must be far more comprehensive, as outlined in report written by Simcyp Consortium members [122].

For the purpose of the work in these sections, comparison against time-course blood plasma concentrations will be adequate for ensure the model is replicating the results first described in the Peters publication. The paper, from which the PBPK model in this chapter is based upon, also provides time-course blood plasma data for a number of different drugs, over different time frames and different initial doses. Both the drugs to be modelled, and their doses are summarised in Table 3.2.

Drug	Dose (IV) (mg)
Bisoprolol	10
Chlorpropamidel	50
Mebendazole	1.18
Theophylline	267

Table 3.2: The four drugs along with their IV doses that will be used to validate the PBPK model taken from Peters [104].

A summary of the physico-chemical properties used to estimate the partition coefficients of the drug are summarised in Table 3.3.

Property	Bisoprolol	Chlorpropamide	Mebendazole	Theophylline
Molecular weight	325.4	276.7	295.3	180
$\log P$	1.83	2.35	3.08	-0.03
Ionization type	Base	Acid	Weak base	Base
pKa	9.15	4.87	5	8.81
Free drug in plasma	0.7	0.04	0.073	0.44
K_p factor	2.5	50	5	1.3

Table 3.3: The physico-chemical properties of the four drugs that will be used to validate the model taken from a publication by Peters [104]. These properties are used for the calculation of tissue specific partition coefficients as described in Section 3.2.2.

Figures 3.2 and 3.3 shows the model prediction (as a solid line) and observed plasma concentrations (as an asterisk) for the four compounds described in Table 3.2. The K_p factor described in Table 3.3 is also used to alter the partition coefficients to ensure a better fit to the *in-vivo* data. The model is shown to fit the data well for all drugs except for mebendazole, shown in Figure 3.3. While the predicted maximum plasma concentration is close the observed, it appears that mebendazole is being cleared either by metabolism or renal excretion. However, as Peters estimates renal excretion by fitting and neither metabolism or intrinsic clearance values are reported, we assumed them to be zero. Inclusion of these terms would lead to a better fit for

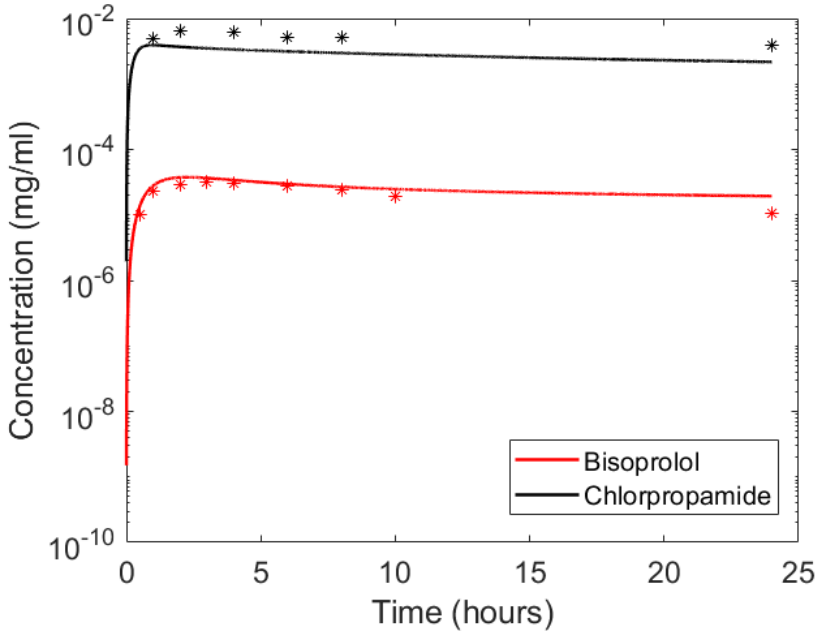

Figure 3.2: The predicted and observed plasma concentration of bisoproplol (in red) and chlorpropamide (in black). Data taken from Peters et al. [104]. Clearance is assumed negligable over this timescale

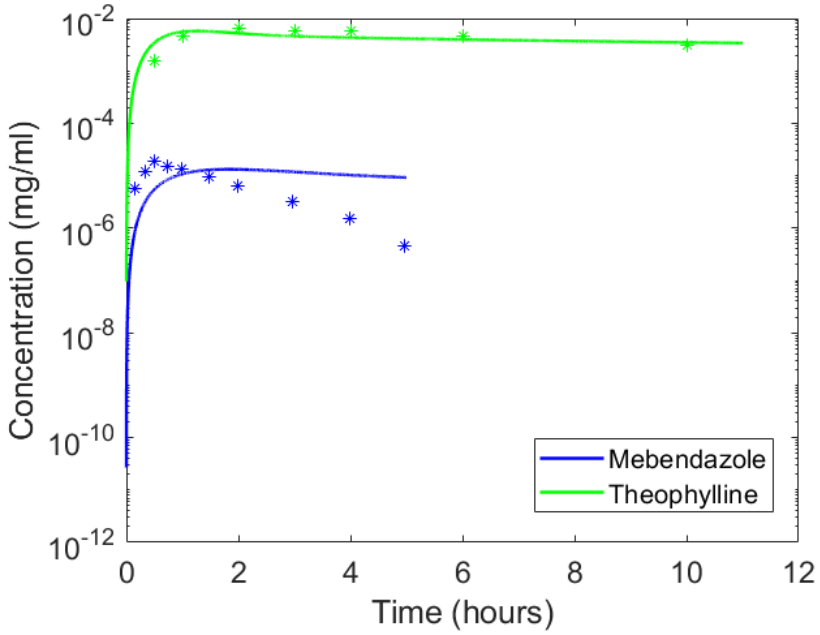

Figure 3.3: The predicted and observed plasma concentration of mebendazole (in blue) and theophylline (in green). Data taken from Peters et al. [104].

drugs which are cleared quickly either by the kidney or liver, like mebendazole.

3.4 PBPK with percutaneous absorption

In order to pair this model with the output from the skin model in Chapter 2, we modify the equation for the skin compartment to account for a transdermal infusion. To begin we first need to understand how we calculated the rate of infusion. A previously referenced piece of work by Danick et al. [87] outlines a method for modelling systemic clearance within the dermis. Clearance through the capillaries is modelled as a 1st order elimination term given as,

$$k_{free} = \left[(P_{cap} S)^{-1} + Q^{-1} \right]^{-1}, \tag{3.11}$$

where S is the capillary surface area, and Q is the *in-vivo* blood flow estimated to be $Q = 2.2 \times 10^{-3}$ s^{-1} by Kretsos et al. [76], and P_{cap} is the capillary permeability. It must be noted that the units of Q were originally volume of blood, per volume of tissue, per second, while the units of S are cm^2/g tissue [76]. The units of S were converted to cm^2/cm^3 by multiplying by the density of dermis, as given by Kretos et al. [123]. This leads to k_{free} being a first order constant, where the value only changes based up on differing physico-chemical properties of the solute permeating the capillaries. A method for estimating P_{cap} is given by Ibrahim et al. [124] as follows,

$$\frac{1}{P_{cap}} = \frac{1}{P_{mem}} + \frac{1}{Paq}, \tag{3.12}$$

where P_{mem} describes the permeability across the endothelial wall, and P_{aq} is the permeability of the aqueous boundary layer adjacent to the membrane. A regression model based upon phospholipid bilayer membrane data is given as,

$$\log P_{mem} = 1.64 \log K_{oct} - 1.37 MW^{1/3} + 2.82r. \tag{3.13}$$

This has been shown to be the primary route of uptake for highly diffuseable lipid-soluble solutes [125]. The inclusion of P_{aq} is important to ensure the limiting of permeation for small, highly lipophilic solutes, which would otherwise be overestimated [126]. A value of P_{aq} may be calculated as follows,

$$P_{aq} = \frac{D_{aq}}{h_{aq}}, \tag{3.14}$$

where D_{aq} is the diffusion coefficient through water and h_{aq} is the thickness of the boundary layer, estimated for small solutes to be around 1×10^{-8} cm.

By multiplying Equation 3.11 by the drug concentration in the dermis, C_{de}, we are able to calculate a time dependent uptake rate. As the solute may only be enter systemic circulation via the dermis, in the region whereby the solute is applied, we must account for this in our uptake term, which is calculated as follows,

$$Uptake = \frac{V_{de}}{V_{sk}}(k_{free} \times C_{de})/bf, \tag{3.15}$$

where V_{sk} is the volume of the skin, as given in Table 3.1, V_{de} is the volume of the dermis of the area of application, and bf is the binding factor, which accounts for the

fraction of non-ionized solute available to the tissues, dervied by Kreetos et al. [76]. This leads to the final form of the rate of change of concentration of the solute in the skin to be,

$$\frac{dC_{sk}}{dt} = \frac{Q_{sk}}{V_{sk}}\left(C_{AR} - \frac{C_{sk} \times R}{f_{u(p)} \times K_{pu(i)}}\right) + \frac{V_{de}}{V_{sk}}(k_{free} \times C_{de})/bf. \tag{3.16}$$

3.5 Lidocaine

Lidocaine is a drug used commonly in medical practice for a variety of situations, administered in a number of different ways: intra-venously (IV); as a patch; and as a topical cream. The pharmacokinetics of lidocaine are well documented for IV administration, making an excellent compound to model. In order to calculate the partition coefficients as outlined in Section 3.2.2 we require the a number of physico-chemical properties.

The acid dissociation constant, pKa, and base dissociation constant, pKb were estimated to be 13.78 and 7.75 using the ChemAxon prediction tool (available at *chemaxon.com/products/calculators-and-predictors-pka*). The partition coefficient, $\log P = 2.26$, was estimated by Hansch et al. [127]. The fraction of unbound drug in the plasma, $f_{u(p)} = 0.3521$, was calculated using a machine learning model by Wantanabe et al. [128], which was parametrised using a large dataset of 2,738 experimental values.

The majority of lidocaine metabolism takes place within the liver by the cytochrome P450 enzyme, CYP3A4. As the value ofDerby K_m is much greater then the concen-

tration in the liver, C_{LI}, the Michaelis-Menten term stays within the linear range, and we may therefore assume it to be a first-order kinetic term, $CL_{int} = V_{max}/K_m$. *In-vitro* values given by Li et al. [129] are as follows; $V_{max} = 10$ pmol/min/10^6 cells and $K_m = 77\,\mu$M. To keep units consistent, we must rescale both the V_{max} and K_m values. To rescale V_{max}, we require the volume of 10^6 cells of human liver, which is reported as [value], and the mass of a picomole of lidocaine, which may be calculated from the molecular weight to be 2.3434×10^{-7} mg/pmol. We may rescale K_m by multiplying by the mass of a micromole of lidocaine, give as 0.2343 mg/μmol, and the number of litres in a millilitre, given as $1 \times 10^{-3} L/mL$. This leads to the following rescaled values; $V_{max} = 6.892 \times 10^{-4}$ mg/min/mL, and $K_m = 0.018$ mg/mL. The final step is to account for change seen between *in-vitro* and *in-vivo* intrinsic clearance rates or *in-vitro-in-vivo-extrapolation* (IVIVE). This is due to to the difference in cytochrome P450 metabolism activity, between cryopreserved and human hepatocytes. Methods for scaling between to two have been discussed in a number of publications, [130, 131], including work by Hallifax et al. [132], who provide an IVIVE scaling factor for lidocaine as 0.7516.

Values for the drug blood-to-plasma ratio, R, and the renal elimination rate, $k_{e(r)}$ are unknown and must be calculated by fitting to experimental data. Additionally, a K_p factor will be calculated, which is a multiplicative scaling factor which alters partition coefficients in each of the compartments to make the model better fit experimental data.

Experimental data of IV lidocaine pharmacokinetics was digitized from work by Ochs et al. [133] using WebPlotDigitizer, a tool for extracting data from figures. In the

paper, seven volunteers were each given three does of lidocaine; 25 mg, 75 mg and 100 mg IV, and serum lidocaine concentrations were measured at various time points for 10 hours.

We fit the model to the experimental data using the non-linear optimisation function, *fminsearch* in Matlab. The *fminsearch* function finds the minimum value of an unconstrained multi-variable function using a derivative-free method; the Nelder-Mead simplex algorithm [134]. The function we look to minimise is the normalised-root-mean-squared-error, which is a normalised error metric, ideal when dealing with datasets with multiple starting doses. The fit provided the parameter values given in Table 3.4.

Parameter	**Nomenclature**	**Value**
Blood-to-plasma ratio	R	7.9977
Renal elimation rate	$k_{e(r)}$	1663
K_p factor	-	0.0431

Table 3.4: PBPK model parameters estimated by fitting to the experimental data taken from Ochs et al. [133].

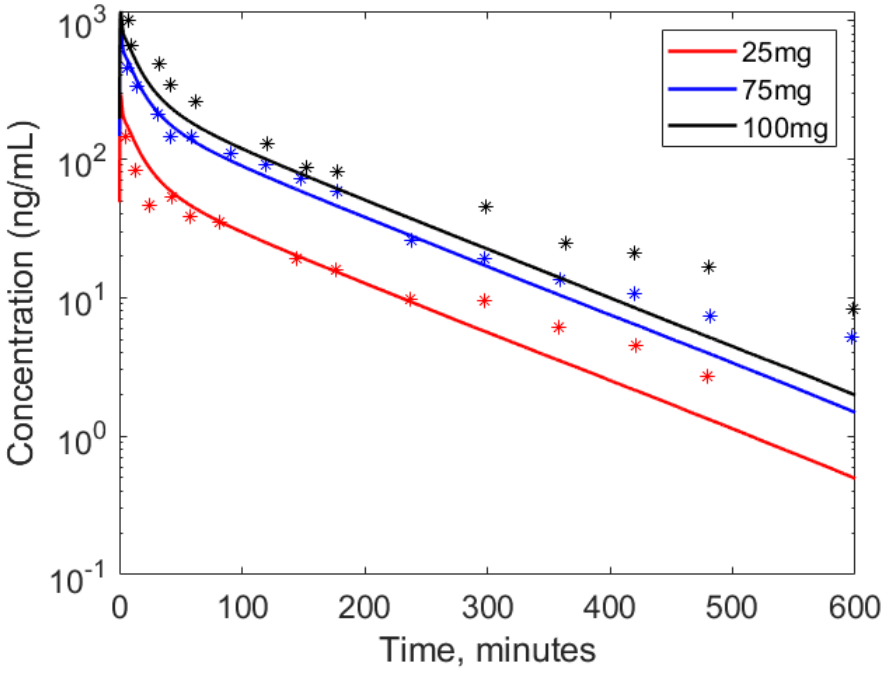

Figure 3.4: Experimental data for three different concentrations of IV lidocaine taken from Ochs et al. [133], shown as points. The model prediction using the fitted parameters is shown as a solid line, where the same colour represents the same dose.

Figure 3.4 shows the predicted time-course profile of three different starting concentrations of IV lidocaine, along with experimental data of the same starting concentrations taken from Ochs et al. [133]. At early time points, the model fits both the 25 mg and 75 mg doses well, while under-estimating the $100mg$ profile. However, after five hours, the model over-estimates the clearance for all three doses. After two hours, we predict that plasma concentration will be in quasi-steady-state, where a reduction in concentration will be governed exclusively by the first order kinetic elimination rates in the liver and kidneys. This leads to the plasma concentration reducing linearly on a log scale, as shown in Figure 3.4. This would suggest a reduction in clearance terms would better fit the data at later time points; however, the model would not then fit the earlier time points as well, increasing the value of the error metric.

3.5.1 Percutaneous absorption of lidocaine

With a fully parametrised PBPK model for lidocaine, we are now able to model its permeation and uptake. We begin by calculating diffusion coefficients as described in Sections 2.3.1 and 2.3.2, partition coefficients as described in Section 2.3.3. The boundary condition on the SC/DP interface is the same as previously described in Section 2.3.4, where the permeation constant is calculated using Equation 2.4, and the maximum concentration in the stratum corneum, C_{sat}, is calculated as follows,

$$C_{sat} = K_{sc/w} S_w, \tag{3.17}$$

where $K_{sc/w}$ is the partition coefficient between the stratum corneum and water, and S_w is the solubility of the lidocaine in water. A summary of these values are given in Table 3.5.

Next, we need to create the geometry which will represent than patch in the skin model. An example of a lidocaine patch made by Endo pharmaceuticals has a trade name LIDODERM. The patch has a surface area of 140 cm^2, and contains 700 mg of lidocaine at 5%w/w. We can therefore infer that a patch has a volume of 14 cm^3 and a depth of 0.1 cm, with an initial concentration of 213.36 mol/m^3. Without the ability to measure experimentally, to calculate the vehicle partition coefficient, it is assumed that the vehicle for which the lidocaine is suspended in is water. While in reality they may use a different vehicle, we believe this will have very little effect on the partition coefficient. However, if it was found there was a large error between the

predicted and actual partition coefficient, this could have a large carry over effect on the simulation. If we overestimated the partition coefficient, the model would predict less drug permeating the stratum corneum than in reality. On the contrary, if we underestimated the partition coefficient for the vehicle, we may instead overestimate permeation, and subsequently the blood-plasma concentration.

Parameter	**Value**	**Units**
D_{veh}	2.70×10^{-11}	m^2/s
D_{sc}	5.4187×10^{-14}	m^2/s
D_{gran}	2.9898×10^{-12}	m^2/s
D_{ex}	2.3958×10^{-11}	m^2/s
D_{int}	1.1174×10^{-11}	m^2/s
Q	1.57×10^{-13}	m^2/s
D_{derm}	8.9759×10^{-11}	m^2/s
D_{aq}	2.7707×10^{-7}	m^2/s
K_{veh}	1.0087	–
K_{sc}	1.3870	–
K_{ed}	0.3966	–
K_{de}	0.7437	–
C_{sat}	55.81	mol/m^3
P_{sc}	8.9374×10^{-6}	m/s

Table 3.5: Skin model parameters for lidocaine. Parameters beginning with D denote diffusion coefficients and parameters beginning with K describe partition coefficients. Q and P_{sc} describe permeability coefficients across cell membrane and the stratum corneum respectively, and C_{sat} is the maximum concentration in the stratum corneum, as defined in Equation 2.24.

Using the information on the patch, and the parameters from Table 3.5, uptake may be calculated as described in Equation 3.11.

Figure 3.5 shows two related plots: in blue, we have the cumulative uptake, measured across the 24 hour time period; and in black is the time dependent uptake rate, which may be calculated as the gradient at each time point of the cumulative plot, using MATLAB's *gradient* function. It is important to note that both of these values are

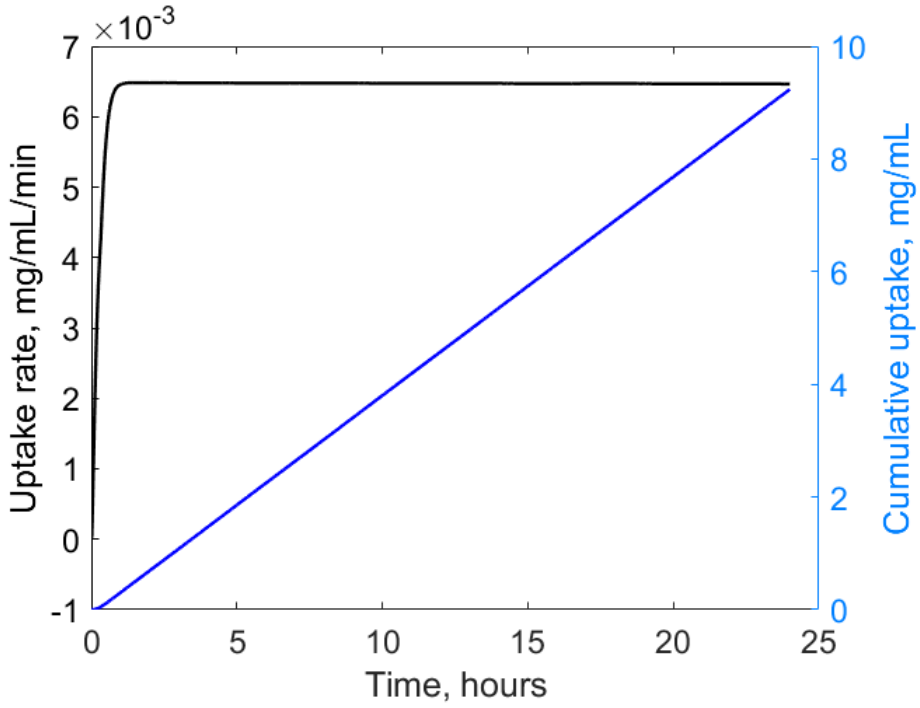

Figure 3.5: Predicted uptake of 700 mg applied over a 24 hour period. The rate of uptake may be derived by calculating the gradient of the cumulative uptake at each time point.

concentrations, and therefore are not dependent on the surface area of the patch. In order to account for the surface area the lidocaine it is applied to, we next calculate V_{derm} from Equation 3.16. It is assumed that the dermis has a constant thickness of 300 μm, and therefore $V_{derm} = 4.2$mL for one patch. Finally, we take $V_{sk} = 7800$ mL as given in Table 3.1, which can be used to calculate the systemic clearance from the dermis at each time point.

Figure 3.6 shows patch plasma concentration as reported by the US Food and Drugs Administration [135] along with our prediction. A comparison between the predicted and observed values of a three different metrics are compared in Table 3.6 for three lidocaine patches, removed after 12 hours. It is clear from Figure 3.6 that our model overestimates both the rate of absorption and rate of clearance when compared to

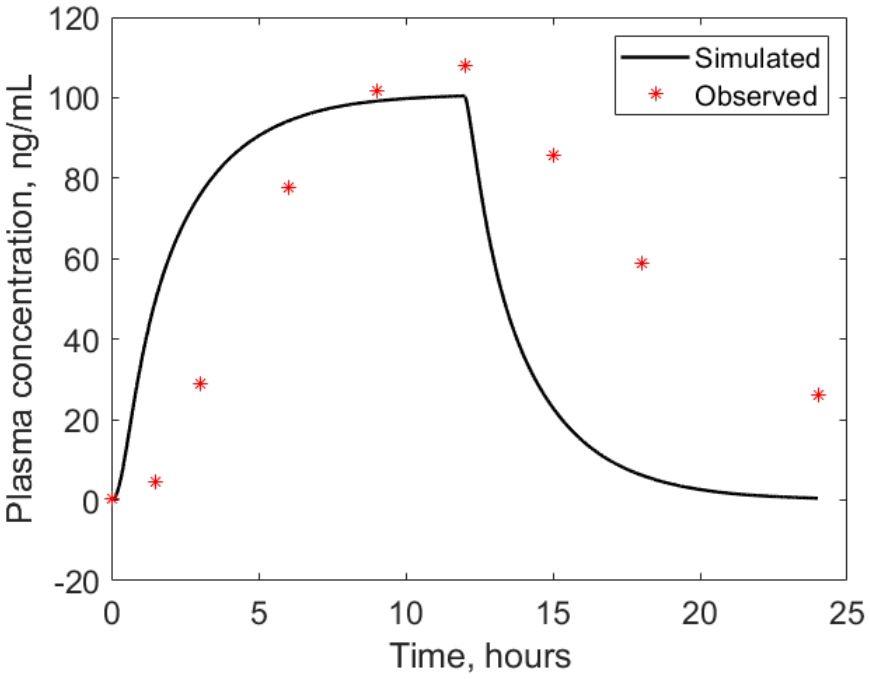

Figure 3.6: Comparison of predicted and observed plasma concentration for three 700 mg lidocaine patches, which are removed after 12 hours.

Parameter	Observed	Predicted	Error
C_{max}	$108.1\,\mu$g/mL	$100.5\,\mu$g/mL	7%
AUC	9.21×10^4 min μg/mL	7.14×10^4 min μg/mL	22.4%
Total absorbed	64 ± 32 mg	57.67 mg	9.89%

Table 3.6: A comparison between the observed and predicted PK metrics, for three 700 mg patches of lidocaine which are removed after 12 hours.

the *in-vivo* data. However, as reported in Table 3.6, the error between observed and predicted values for the maximum plasma concentration and total absorbed are within an acceptable range. The total absorbed metric is particularly important, as it is the only value that can be measured independently of the total mass of the subject for which the patch is applied. The assumption of the PBPK model is that the person is a 70kg, white male, and therefore, any deviation from this assumption may lead to discrepancies between predicted and observed plasma concentration. However, the

information on patients weights, gender and ethnicity was not provided in the FDA report. Furthermore, it was assumption that no drug would enter systemic circulation after 12 hours, and therefore does not account for the drug left in the dermis and epidermis. Accounting for this may lead to a more gradual elimination after 12 hours, leading to a better fit of the data.

3.6 Investigating model parameters

3.6.1 Varying stratum corneum thickness

The thickness of the stratum corneum varies across the body. In regions of the body such as feet, hands and the elbows, the skin has an additional layer named the statum lucidum which consists of keratinocytes. Additionally, the stratum corneum thickness is increased, reaching up to 40 μm [136]. As the stratum corneum is the primary barrier of the skin, increasing its thickness will lead to reduced permeation of xenobioitcs, however, the extent of which has not yet been quantified. This is particularly important in modelling exposure style scenarios, whereby, different parts of the body may be exposed to a xenobioitc. The part of the body which is exposed will influence how much of the xenobiotic enters systemic circulation.

We will assume that the cells within the stratum lucidum are similar to those found in the stratum corneum, and therefore, the stratum lucidum and stratum corneum may be treated as a single homogeneous compartment. We may therefore explore how percutaneous absorption varies across the body, by varying the thickness of the stratum corneum only.

Figure 3.7 shows the predicted change in plasma concentration by altering the thickness of the stratum corneum between 6 μm and 40 μm. Lidocaine applied to skin with a stratum corneum with a thickness of 40 μm has a 43.5% reduction in plasma concentration when compared to 6 μm skin after 12 hours. The increased thickness reduces concentration within the stratum corneum, which in turn reduces the concentration in the epidermis and dermis, due to reduced concentration gradients. This leads to a reduced uptake rate and a lower plasma concentration.

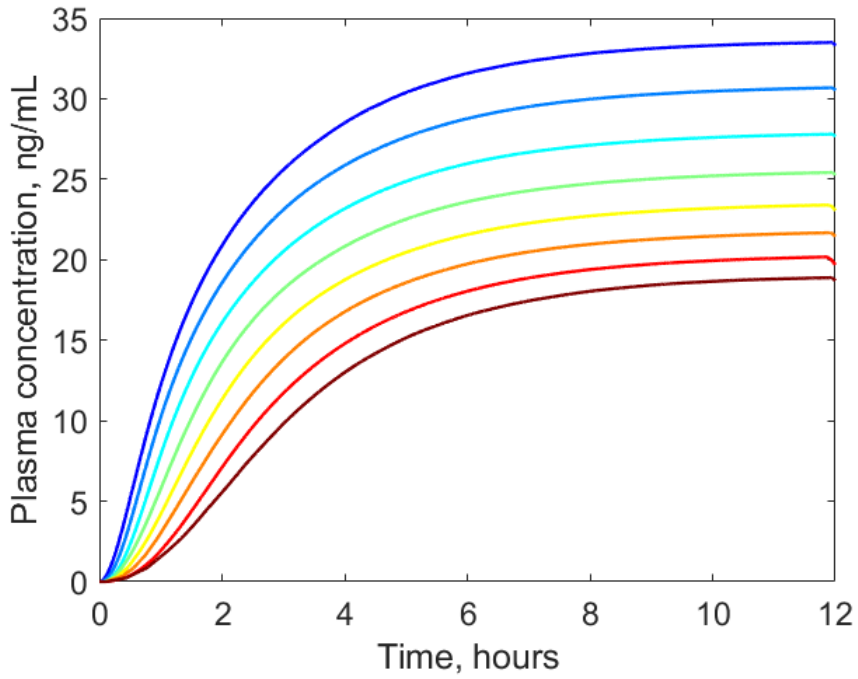

Figure 3.7: The change in plasma concentration when one 700mg lidocaine patch is applied to skin with different stratum corneum thickness's. The stratum corneum thickness is evenly varied between 6 μm (in blue) and 40 μm (in red).

When modelling the same system with small changes, there will be some relation between the C_{max} and AUC as shown in Figure 3.8. As K_m is far greater then the concentration in the liver and therefore within the linear range of the Michaelis-Menten term , the metabolism, excretion and uptake terms are all first order kinetics

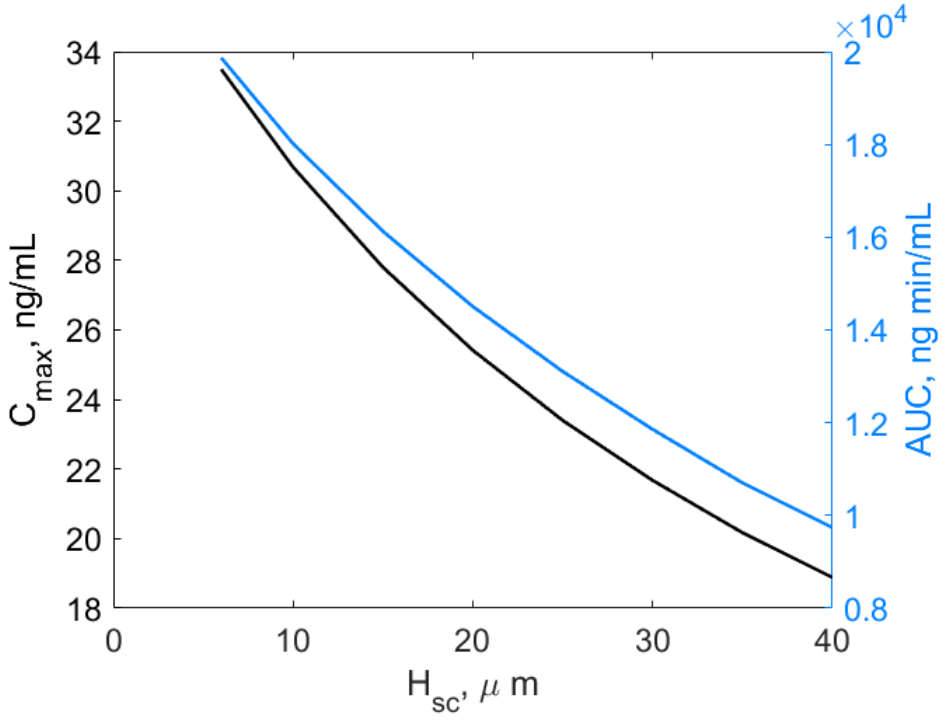

Figure 3.8: The change in the maximum plasma concentration (black) of lidocaine, and area under the curve (blue) after 12 hours, from varying the thickness of the stratum corneum.

terms. This leads to similar dynamics between simulations, and therefore, an increase in C_{max} is going to lead to a similar increase in the area under the curve. A stratum corneum with a thickness of 6 μm, leads to a 2-fold increase in the AUC, and a 75% increase in the maximum concentration in the plasma when compared to one of with a thickness of 40 μm. These changes will be greater for compounds less soluble in the SC, and reduced for compounds which are more soluble due to the barrier function of the stratum corneum.

3.6.2 Varying the vehicle concentration

Perhaps the most obvious way to increase the amount of compound permeating the skin, is to increase the concentration of the initial dose. When pharmaceutical compa-

nies are looking at patch or cream formulation, it may be economically advantageous to increase the concentration in order to reduce the cost of any secondary materials required. In order to gain a greater understanding on the relationship between the initial concentration and uptake, we varied our simulated patch concentration, to see the change in plasma concentration.

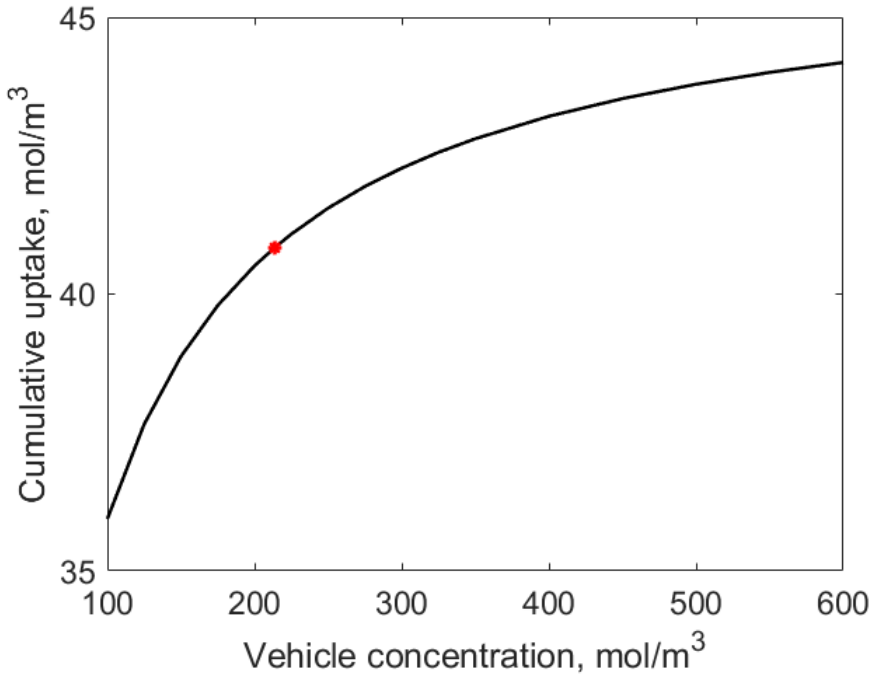

Figure 3.9: The change in cumulative uptake from the dermis after 12 hours, predicted for initial vehicle concentrations between 100 mol/m^3 and 500 mol/m^3. Highlighted in red is the vehicle concentration currently used in medical practice in patches.

Figure 3.9 shows the relationship between starting vehicle concentration and the cumulative uptake after 12 hours.

As uptake is modelled using first order kinetics, the rate of uptake and cumulative uptake share similar dynamics. Highlighted in red is the current concentration used in medical patches, 213.36 mol/m^3. It is particularly interesting to note that a two-fold increase in patch concentration only increases the cumulative uptake by 5% and

an almost three-fold increase in patch concentration only increases uptake by 7.5%. This may be attributed to the solubility of lidocaine in the skin, and its relation to C_{sat}, and therefore, an increase in vehicle concentration does not increase the concentration in the SC by an equal fraction. It was found for each of the starting vehicle concentrations, that steady-state was reached between the layers of the skin after three hours. Therefore, an increase in SC concentration will lead to an increase in both epidermis, and dermis concentrations, which in turn leads to an increase in uptake.

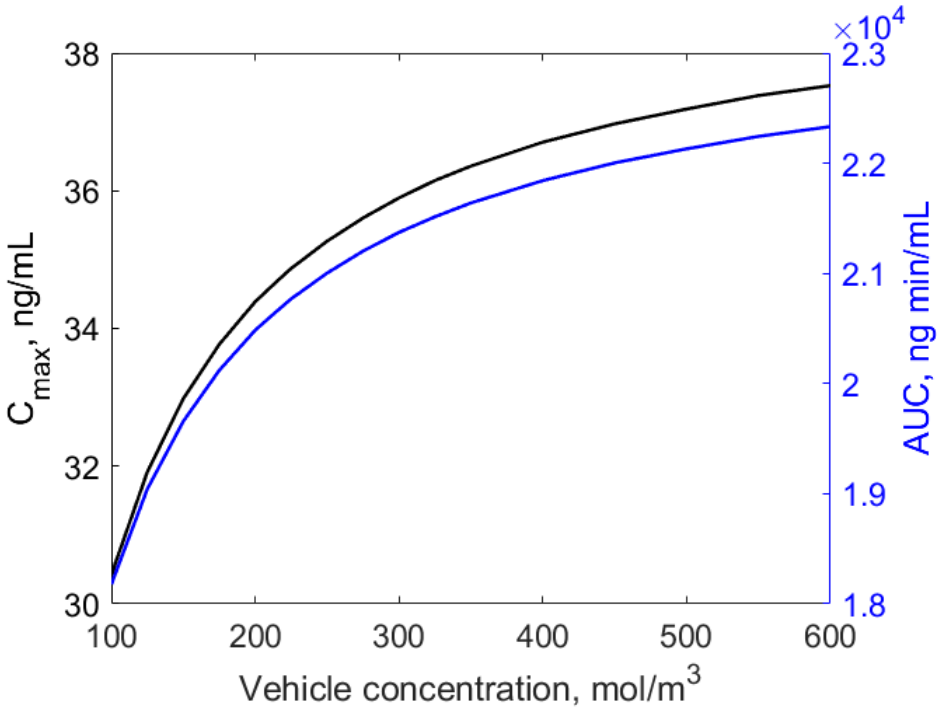

Figure 3.10: The change in the maximum plasma concentration (black), and area under the curve (blue) after 12 hours, from varying concentration of the vehicle.

Similar to what was found with the cumulative uptake, increasing the initial concentration from what is found in medical practice by three-fold only increases both the maximum plasma concentration and area under the curve by 8%. Again, this

may attributed to the lower value of C_{sat} as defined in Equation 2.24, calculated for lidocaine, causing a small increase in stratum corneum concentration for a large increase in vehicle concentration. As the concentration in the patches for medical use are already close to four times the calculated C_{sat}, the increase in stratum corneum, and in turn, plasma concentration will diminish. However, for compounds which have higher solubility in the stratum corneum, and therefore a greater C_{sat} value, increasing vehicle concentration will have a far greater effect on stratum corneum and plasma concentrations.

3.6.3 Atopic dermatitis

Atopic dermatitis (AD) is a chronic inflammatory skin disease which causes hyper-reactivity to environmental triggers [137, 138], with the most common form being eczema. The cause of AD is complex, and can be linked to a number of different immunologic and inflammatory pathways. AD has been linked to changes in groups of genes that are responsible for encoding proteins [139]. One of the key loss-of-function mutations is found with the FLG gene responsible for encoding the structural protein, filaggrin [140]. An increase in protease activity, and decreased sythesis of the lipid lamellae lead to a reduction in the dermal barrier property. This is due to an elevated stratum corneum pH, which inhibits enzyme activity for both of these processes.

In Section 2.3.4, we argued that the presence of the binding protein filaggrin leads to the need for a saturation function on the vehicle-stratum-corneum boundary due to its link with barrier function. However, as discussed above, in the case of atopic dermatitis, we find greatly reduced levels of filaggrin in the stratum corneum. In

order to model atopic dermatitis, we may therefore remove this saturation function, replacing it instead with a continuity of flux style boundary condition, as described in Section 2.3.3.

The investigation of the effects of atopic dermatitis is particularly important, as compounds that were previously found not to reach levels which cause toxicity, either in the skin or when entering systemic circulation, may in-fact now reach these levels due to the reduced barrier function. It is therefore important to quantify the difference between normal functioning skin, and skin affected by atopic dermatitis. While there is some evidence that AD has some impact on the diffusivity [141], this has not been quantified in the literature, and we believe the that alteration of the boundary condition encapsulates what is happening physiologically.

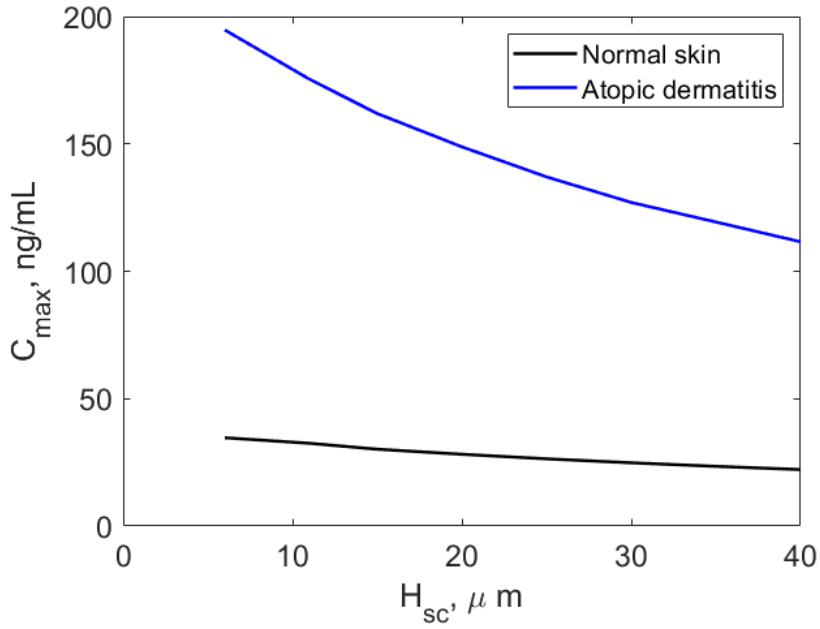

Figure 3.11: The change in the maximum plasma concentration predicted for skin with and without atopic dermatitis with SC thickness, (H_{sc}), varying in the physiological range.

Figures 3.11 and 3.12 show the change in maximum concentration and area under the curve respectively achieved by altering the thickness of the stratum corneum. Like found in Figures 3.8 and 3.10, the dynamics between C_{max} and the AUC are very similar for atopic dermatitis. As discussed in Section 3.6.1, this may be attributed to the first-order rate kinetics for infusion, excretion, and metabolism. With normal skin, we see a two-fold increase in the AUC and a 75% increase in maximum plasma concentration from varying the stratum corneum thickness from 40 μm to 6 μm. Likewise, with atopic dermatitis, we see the same two-fold increase in AUC, and 75% increase in C_{max}. Atopic dermatitis leads to around a five-fold increase in both the maximum plasma concentration and AUC for all thickness's when compared to normal skin. Next, we investigate the effect of changing vehicle concentration on skin with atopic dermatitis.

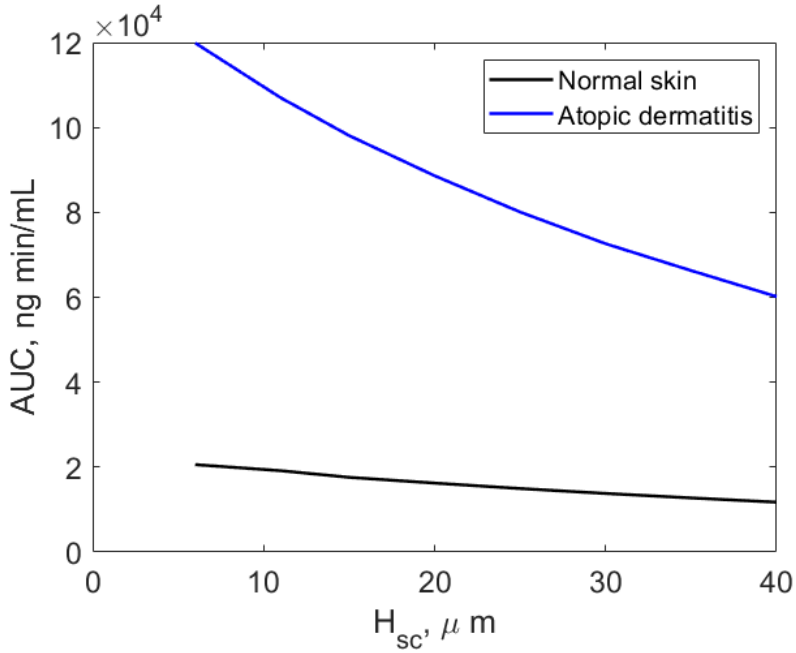

Figure 3.12: The change in the area under the curve (AUC) predicted for skin with and without atopic dermatitis with SC thickness varying in the physiological range. The model is simulated between 0 and 12 hours.

It is clear from Figures 3.13 and 3.14 that increasing vehicle concentration has a significant impact on both the maximum plasma concentration and AUC. With the removal of the saturation function on the DP/SC boundary due to the reduced presence of filaggrin found with atopic dermatitis, concentration in all layers of the skin increase proportionally with the concentrations in the vehicle. This increase in dermis concentration leads to increased uptake, resulting in increased plasma concentration. Both C_{max} and AUC increase linearly with increasing vehicle concentration. A two-fold increase in vehicle concentration from what is currently used medically results in a two-fold increase in both C_{max} and the AUC for skin with AD, compared to 5% increase for both without atopic dermatitis.

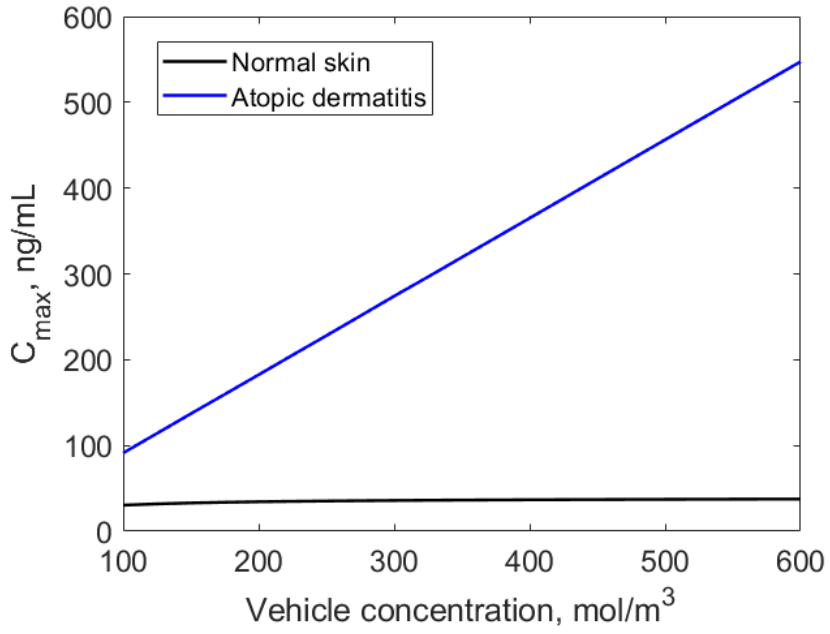

Figure 3.13: The change in the maximum plasma concentration predicted for skin with and without atopic dermatitis with the initial concentration in the vehicle varying between 100 mM and 500 mM.

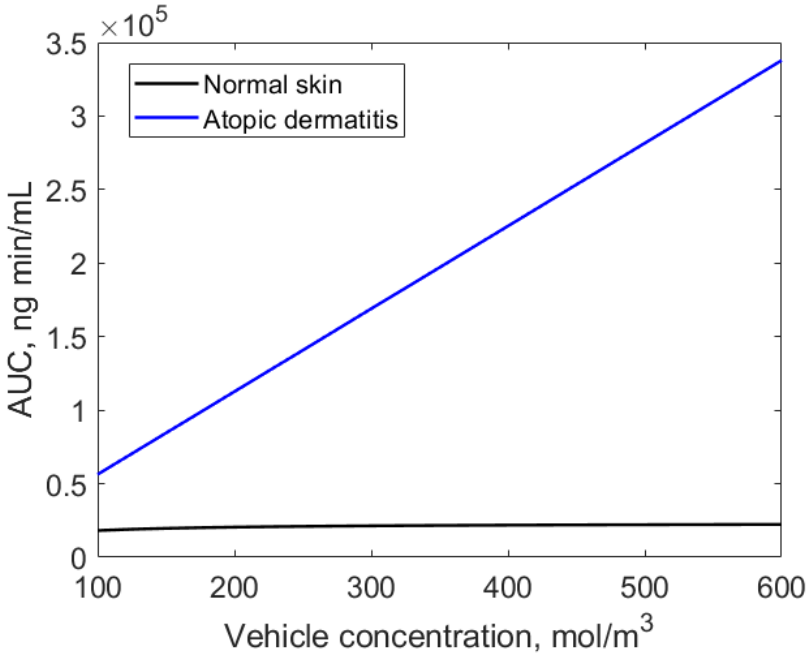

Figure 3.14: The change in the area under the curve (AUC) predicted for skin with and without atopic dermatitis with the initial concentration in the vehicle varying between 100 mM and 500 mM.

3.7 Chapter discussion

This chapter describes the combination of the complex skin model from Chapter 2, with a whole-body PBPK model, which may be used to describe the entire process from uptake to removal via metabolism or renal excretion. Unlike many of the currently published PBPK models which account for percutaneous absorption [57, 58, 59, 60, 61, 62], uptake in this model is driven by the compounds ability to passively diffuse across the capillaries present in the dermis, rather than a difference style term (i.e. rate of uptake governed by the concentration gradient between the dermis and blood). This is particularly advantageous, as the permeation of the endothelial wall, and a compounds $\log P$ and molecular weight has been shown to be

related [125]. It also ensures that the permeation of small, highly lipophilic solutes is not overestimated as reported by Cussler et al. [126].

The PBPK model was initially validated against intravenous (IV) data for four compounds with varying physico-chemical properties taken from work by Peters [104]. This validation highlighted the need for the inclusion of a K_p factor, which either increases or decreases the partition coefficient of each organ by a given scaling factor in order to better fit the IV data. For each of the compounds simulated, a different k_p factor was required in order to better fit the IV data. The model was shown to fit the IV data well, except for mebendazole, which would require a value for the excretion term. As discussed by Peters in the publication, the renal excretion value was fitted to the data in order to minimise the error; however, it was not reported and therefore assumed to be 0.

We also fit the model to IV lidocaine data to estimate values for the blood-to-plasma ratio, R, renal elimination rate, $K_{e(r)}$ and the k_p factor. This was an important step as none of these parameters had values available within the literature and the estimated plasma concentration was sensitive to all three. With both the skin model from Chapter 2, and the PBPK model parametrised, we were now able to explore how changes to the model affect the plasma concentration.

The purpose of a model like that described in this chapter may be used to answer two key questions: how much drug enters systemic circulation; and what is the rate at which the drug enters circulation? Two factors that affect the answer to these questions is the concentration of drug applied, and where it is applied to. It was found for lidocaine that increasing the concentration in the vehicle had little effect on

the plasma concentration due to the value of C_{sat} estimated for lidocaine. However, for compounds with a greater lipophilicity, increasing the vehicle concentration will have a greater effect due to an increase in the value of C_{sat}. Increasing the thickness of the skin showed far greater effects on the plasma concentration for two reasons: a thicker stratum corneum means a greater distance for the compound to travel to the dermis; and a greater amount of the compound is required to reach the saturating concentration. This reduces the concentration in both the epidermis and dermis leading to reduced uptake.

Atopic dermatitis was modelled through the removal of the saturation function on the SC/DP boundary. This was particularly important to quantify for exposure style scenarios, whereby, a reduction in barrier properties could potentially lead to toxic levels of a compound entering systemic circulation when the normal barrier properties of skin would have prevented it. We estimated that for all thicknesses of stratum corneum, atopic dermatitis leads to a five-fold increase in the maximum plasma concentration. The more important factor for atopic dermatitis was shown to be the concentration in the vehicle. The removal of the barrier property, along with doubling the vehicle concentration from that found in current medical patches, resulted in a two-fold increase in plasma concentration, compared with a 5% increase for skin without atopic dermatitis. However, what was particularly interesting was that the increase in concentration due to the removal of barrier properties, paired with an increased vehicle concentration, leads to a multiplicative effect on the plasma concentration i.e. both changes increase plasma concentration, but when paired together show a greater increase then the sum of their individual effects.

Chapter 4

Mathematical modelling of nanoparticle delivery to cancer cells

4.1 Background

A malignant tumour is characterised by uncontrolled growth of abnormal cells which have undergone epigenetic changes escaping the normal cell cycle to form a mass within solid tissue (muscle, organ, bone) [142]. Cancer is a more broad term, used to describe the group of different malignant tumours which may form throughout the body. There are currently over 200 types of known cancers, arising in different areas of the body caused by genetic changes in the DNA of a cell [143]. Within the UK, around 300,000 people are diagnosed with some form of cancer each year [144], with 5 year mortality rates ranging from 3% for skin cancer, to 94.8% for pancreatic cancer [145]. The majority of tumours are treated via surgery, radiotherapy, chemotherapy, or some combination of these methods [146]. Surgery aims to remove all of the tu-

mour cells; however, when unsuccessful, more aggressive treatments in radiotherapy and chemotherapy are both options [147]. Radiotherapy makes use of ionizing radiation which damages the DNA within the tumour cells [148], killing these cells and reducing the size of the tumour. However, this often elicits the side effect of damaging nearby tissue. Chemotherapy is the name given to a set of treatments, which interrupts various stages of the mitosis pathway, reducing or stopping the spread and growth of rapidly dividing cancerous cells [149]. Chemotherapeutic drugs may be used simultaneously and are delivered systemically. However, the effectiveness of changing, or mixing the chemotherapeutic will largely depend on the type and stage of development of the cancer. In a survey by Carelle et al. [150], patients undergoing chemotherapy reported 82 physical and non-physical side effects, including fatigue, nausea, hair loss, emesis and diarrhoea.

One particular area of research aims to avoid the adverse effects of chemotherapy, and increase its efficacy through the use of polymersomes which encapsulate therapeutic agents. The vascular nature of tumours causes an accumulation of anticancer molecules due to elution of the drug [47, 151]. Polymersomes are nano-sized vesicles constructed using amphiphilic synthetic block copolymers to create a membrane [152], which may be used to house a therapeutic agent [153, 154]. Due to the synthetic nature of the membranes, they may be altered to have more desirable properties. For example, it has been shown that polymersomes may enter the cells via the endocytotic pathway [155, 156], and therefore, one desirable property may be pH-sensitive membrane. Membranes constructed of poly-2-(methacryloyloxy) ethyl phosphorylcholine (PMPC), or poly- 2-(diisopropylamino)ethyl methacrylate (PDPA) have been shown

to self assemble in neutral environments, but disassemble in enviroments with a pH less than 6.44 [157, 158]. When the polymersomes enter the endosome, the acidic environment causes the membrane of the polymersome to disassemble, releasing the therapeutic agent. The increase in osmotic pressure then causes the endosome to rupture, releasing the therapeutic agent intra-cellularly [159].

In the development of new cancer treatments, it is important for the treatment to reach the targeted cells at the correct therapeutic dose. The use of polymersomes also adds the complication of ensuring the formation of bonds between the polymersome and cell surface receptors. A mathematical model allows us to study the interactions between the cells and polymersomes, to ascertain the key properties affecting this binding and uptake. This allows us to inform the experimentalist how to better formulate the synthetic membranes of the polymersomes, and to ensure maximized uptake.

In this chapter, we begin by looking at a previously published, time-dependent model of polymersome uptake by cancer cells. The model is parametrised against experimental data of the uptake of polymersomes by monolayers of cancer cells, and provides us with a detailed framework to build a more physiologically relevant model. We then show that, with certain assumptions, model complexity may be greatly reduced, while maintaining all relevant outputs, through the use of statistical moments. We then modify the aforementioned model, with the addition of spatial dimensions, to more closely mimic what would be found in a 3D *in-vitro* experiment. Finally, we make use of fluorescence data of polymersome uptake within spheroids, to parametrise values related to the geometry of the spheroid. We then have a fully parametrised spatio-

temporal model, which can be analysed, to understand the key factors which affect the penetration and uptake of polymersomes by cancer cells.

4.2 Binding model

We begin by looking at published model by Sorrell et al. [63], on which all models within this chapter will be based upon. A schematic of the binding process is given in Figure 4.1. This schematic describes how an unbound polymersome with ligands specific to a cell type may bind to receptors on a cell surface. Once bound, it may disassociate, form subsequent bonds or enter the cell via endocytosis. The model is comprised of $n + 4$ ordinary differential equations (ODEs), where n is the maximum number of bonds that can form between a polymersome and receptors on the cell surface. The polymersomes can therefore either be unbound (B_0, Polymersomes mL^{-1}), bound with i bonds (B_i, Polymersomes mL^{-1}), or internalised (B_{in}, Polymersomes mL^{-1}). The remaining 2 variables within the model represent the concentration of receptors that are unbound (F_s, receptors mL^{-1}) and internalised (F_{in}, receptors mL^{-1}). The rate of change over time of the concentration of unbound polymersomes is given as follows,

$$\frac{dB_0}{dt} = -k_{3a} n F_s B_0 + k_d B_1, \tag{4.1}$$

where k_{3a} is the binding association parameter (mL receptors^{-1} min^{-1}), F_s is the number of free cell surface receptors per mL (receptors mL^{-1}), B_1 is the number of polymersomes per mL bound to a cell with one bond (polymersomes mL^{-1}) and k_d is the dissociation rate (min^{-1}). Once the polymersome has bound to a cell, it

is assumed that any subsequent binding with that polymersome may only happen to this cell (i.e, a single polymersome may not bind to two cells at the same time). Therefore, the rate of subsequent binding is dependent on the number of remaining unbound surface receptors for that given cell, given as F_s/M where M is the number of cells per ml. The rate equation for B_1 is then given as:

$$\frac{dB_1}{dt} = k_{3a} n F_s B_0 - k_d B_1 - \frac{k_{2a}}{M}(n-1)F_s B_1 + 2k_d B_2 - k_{in}(1)B_1, \tag{4.2}$$

where k_{2a} is the $2D$ binding association parameter for polymersomes already bound to a cell (cells receptors^{-1} min^{-1}), B_2 is the number of polymersomes bound with two bonds per mL and k_{in} (min^{-1}) is the internalisation rate of the polymersomes, which may be constant or a function of the number of bonds (e.g, $k_{in}(i)$). The rate equation for polymersomes bound with $i = 2, ..., n-1$ bonds is given as,

$$\frac{dB_i}{dt} = \frac{k_{2a}}{M}(n-i+1)F_s B_{i-1} - i k_d B_i - \frac{k_{2a}}{M}(n-i)F_s B_i + (i+1)k_d B_{i+1} - k_{in}(i)B_i. \tag{4.3}$$

The rate equation for the number of polymersomes per mL bound with the maximum number of bonds, n, is given as,

$$\frac{dB_n}{dt} = \frac{k_{2a}}{M} F_s B_{n-1} - n k_d B_n - k_{in}(n)B_n. \tag{4.4}$$

The rate of change of free surface and internalised receptors are given, respectively, as,

$$\frac{dF_s}{dt} = -k_{3a} n F_s B_0 - \frac{k_{2a}}{M} F_s \sum_{i=1}^{n-1} (n-i) B_i + k_d \sum_{i=1}^{n} i B_i + u F_{in}, \tag{4.5}$$

$$\frac{dF_{in}}{dt} = \sum_{i=1}^{n} k_{in}(i) B_i - u F_{in}, \tag{4.6}$$

where u is the rate at which internalised receptors are recycled back to the cell surface (min^{-1}). The final ODE represents the rate of change of internalised polymersomes, namely:

$$\frac{dB_{in}}{dt} = \sum_{i=1}^{n} k_{in}(i) B_i. \tag{4.7}$$

Parameter descriptions, values and units are given in Table 4.1. Initial conditions are given in Table 4.2. Both the paramater values and initial conditions were taken from work by Sorrell et al. [63].

Parameter	Notation	Value	Units
Free binding rate	k_{3a}	1.4×10^{-19}	mL receptors^{-1} min^{-1}
Bound binding rate	k_{2a}	1.9×10^{-3}	cells receptors^{-1} min^{-1}
Internalisation rate (constant case)	k_{in}	0.612	min^{-1}
Dissociation rate	k_d	3.75×10^{-25}	min^{-1}
Maximum number of bonds	n	40	dimensionless
Receptor recycling rate	u	0.1	min^{-1}
Concentration of cells	M	5×10^4	cells mL^{-1}

Table 4.1: Parameter descriptions, values and units taken from work by Sorrell et al. [63].

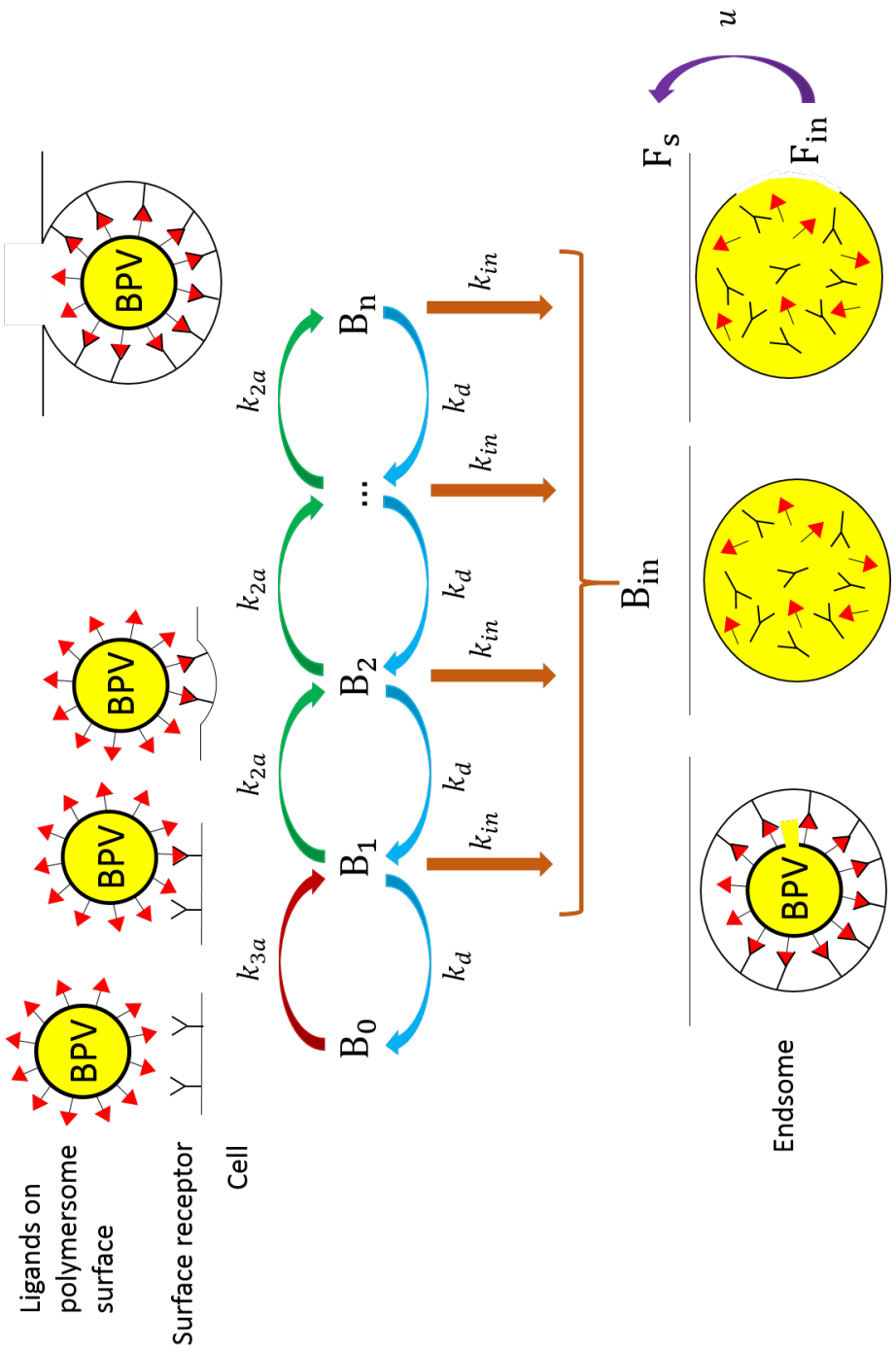

Figure 4.1: A schematic for the internalisation of polymersomes. Key variables are shown in larger font, parameters are given in italics. Initially binding takes place at a rate of k_{3a}, once bound a polymersome may subsequently bind at a rate of k_{2a}, dissociate at a rate k_d, or is internalised at a rate k_{in}. Once internalised, the increased pH within the endosome causes the amphiphilic membrane to rupture, releasing the therapeutic agent within the endosome. The increased osmotic pressure then causes the endosome to burst, releasing the therapeutic agent. Internalised receptors are then returned to the cell surface at a rate u.

Variable	Notation	Initial value	Units
Unbound surface receptors	F_s	1000	Receptors cell^{-1}
Unbound internal receptors	F_{in}	0	Receptors cell^{-1}
Free polymersomes	B_0	6.81×10^{13}	Polymersomes mL $^{-1}$
Bound polymersomes	$B_1, ..., B_n$	0	Polymersomes mL $^{-1}$
Internalised polymersomes	B_{in}	0	Polymersomes mL $^{-1}$

Table 4.2: Variable descriptions, values and units taken from work by Sorrell et al. [63].

4.3 Statistical moments

In Section 4.2, we outlined a model for polymersome uptake by cancer cells. In this section, we show how we can reduce the model complexity, from $n + 4$ equations to 8 through the use of statistical moments. This allows us to look at the effect of increasing the maximum number of bonds, n, without increasing computational power that would have been required due to an increased number of equations. A statistical moment model also provides information on variables of interest such as number of bound polymersomes, total number of bonds, number of internalised polymersomes, number of surface and internalised receptors, as well as quantifying the descriptive statistics of bound polymersomes.

A moment is a measure of the shape of a function. Within statistics, a set of moments can be used to uniquely desribe the distribution of a dataset. The significant moments for the purpose of this work are the mean, which is a raw moment; variance, which is a central moment; and skewness and kurtosis, which are normalised moments [160], as given in Table 4.3. A raw moment is taken about 0, while a central moment is taken around the mean. Normalised moments, are central moments, normalised by the standard deviation in order to render the moment scale invariant. Where X is a

random variable, we may use the following to define a *1st* order raw moment,

$$\mu = \mathbf{E}[X]. \tag{4.8}$$

This is simply the mean (i.e. the expectation), or the average number of bonds formed between cells and polymersomes. The *nth* order centralised moment, about the mean μ, is given as,

$$\mu_n = \mathbf{E}[X - \mu]^n. \tag{4.9}$$

We use this to find our second order moment, variance, (σ^2), which describes the spread of the number of bonds formed between polymersomes and cells. The *nth* order normalised moment is the *n'th* central moment divided by σ^n,

$$\frac{\mu_n}{\sigma^n} = \frac{\mathbf{E}[X - \mu]^n}{\sigma^n}. \tag{4.10}$$

We may use this to find the third and fourth order moments, given as skewness and kurtosis respectively. Skewness describes the asymmetry of the distribution of bonds, while kurtosis is a measure of the combined size of the two tails of distribution of the bonds.

Moment	Order	Nomenclature
Mean	1	μ
Variance	2	σ^2
Skewness	3	γ_1
Kurtosis	4	γ_2

Table 4.3: The first four statistical moments.

In order to make use of the above moments, we must relate it to the model given in

Section 4.2. We define the total number of bound polymersomes to be v_0, and the total number of bonds to be v_1,

$$v_0 = \sum_{i=1}^{n} B_i, \tag{4.11}$$

$$v_1 = \sum_{i=1}^{n} iB_i. \tag{4.12}$$

We are able to define a more general form of the above, in order to find higher order moments of the model from Section 4.2,

$$v_x = \sum_{i=1}^{n} i^x B_i. \tag{4.13}$$

Finally, we may relate our expected value of X, to Eq 4.13 to give,

$$\mathbf{E}[X^n] = \frac{v_n}{v_0}. \tag{4.14}$$

We are now able to quantify our four relevant statistical moments in terms of variables found in section 4.2, and use these to find an averaged model written in terms of these statistical moments.

4.4 An averaged model using statistical moments

We previously defined v_0 in Eq 4.11, to be the total number of bound polymersomes. We are able to find the rate of change of v_0 by taking the summation of equations

4.2-4.4, given as,

$$\frac{dv_0}{dt} = \frac{d}{dt}\left(\sum_{i=1}^{n} B_i\right) = \sum_{i=1}^{n} \frac{dB_i}{dt} = \frac{dB_1}{dt} + \frac{dB_2}{dt} + ... \frac{dB_n}{dt} = k_{3a} n B_0 F_s - \sum_{i=1}^{n} k_{in}(i) B_i - k_d B_1. \tag{4.15}$$

If we assume the internalisation rate k_{in} is constant, i.e, $k_{in}(i) = k_{in}$, then we may re-write equation 4.15 as,

$$\frac{dv_0}{dt} = k_{3a} n B_0 F_s - k_{in} \sum_{i=1}^{n} B_i - k_d B_1. \tag{4.16}$$

To close the system, we assume that the 2D binding rate, (k_{2a}) is fast compared to k_{3a}, such that once a polymersome has bound to a cell, it will quickly form more bonds. Therefore, it is assumed that $k_d B_1$, (the dissociation rate where a polymersome with one bond reverts to being unbound) is very small, and taken to be ≈ 0. This leads to,

$$\frac{dB_0}{dt} = -k_{3a} n B_0 F_s, \tag{4.17}$$

$$\frac{dv_0}{dt} = k_{3a} n B_0 F_s - k_{in} v_0. \tag{4.18}$$

The rate of change of the number of bonds, v_1, is given as,

$$\frac{dv_1}{dt} = \frac{d}{dt}\left(\sum_{i=1}^{n} i B_i\right) = 1\frac{dB_1}{dt} + 2\frac{dB_2}{dt} + ... + n\frac{dB_n}{dt}, \tag{4.19}$$

which leads to,

$$\frac{dv_1}{dt} = F_s\left[k_{3a} n B_0 + \frac{k_{2a}}{M}(n v_0 - v_1)\right] - k_d v_1 - k_{in} v_1. \tag{4.20}$$

Finally, a generalised form to find dv_x/dt is given as,

$$\frac{dv_x}{dt} = F_s\Big[k_{3a}nB_0 + \frac{k_{2a}}{M}\sum_{i=1}^{n}(n-i)\Big[(i+1)^x - i^x\Big]B_i - \sum_{i=1}^{n} i^x k_{in}B_i \\ - \sum_{i=1}^{n}(i^{x+1} - i(i-1)^x)k_d B_i. \tag{4.21}$$

For the purpose of this work, we will calculate up to v_4 to incorporate all the moments outlined in Section 4.3. In order to calculate our averaged equations for our receptor terms F_s and F_{in}, we make use of Equation 4.13, to substitute relevant terms. Similarly, for our internalisation term B_{in}, we may substitute in Equation 4.11 into Equation 4.7 to find its averaged form. This leads to the following system,

$$\frac{dB_0}{dt} = -k_{3a}nB_0F_s, \tag{4.22}$$

$$\frac{dv_0}{dt} = k_{3a}nB_0F_s - k_{in}v_0, \tag{4.23}$$

$$\frac{dv_1}{dt} = F_s\Big[k_{3a}nB_0 + \frac{k_{2a}}{M}(nv_0 - v_1)\Big] - k_d v_1 - k_{in}v_1, \tag{4.24}$$

$$\frac{dv_2}{dt} = F_s\left[k_{3a}nB_0 + \frac{k_{2a}}{M}((2n-1)v_1 - 2v_2 + nv_0)\right] - (2v_1 - v_0)k_d - k_{in}v_2, \tag{4.25}$$

$$\frac{dv_3}{dt} = F_s\left[k_{3a}nB_0 + \frac{k_{2a}}{M}\big(-3v_3 + 3v_2(n-1) + v_1(3n-1) + nv_0\big)\right] \\ - (3v_2 - 3v_1 + v_0)k_d - v_3k_{in}, \tag{4.26}$$

$$\frac{dv_4}{dt} = F_s\Bigg[k_{3a}nB_0 + \frac{k_{2a}}{M}(-4v_4 + v_3(4n-6) + v_2(6n-4) + v_1(4n+1) + \\ nv_0)\Bigg] - (4v_3 - 6v_2 + 4v_1 - v_0)k_d - v_4k_{in}, \tag{4.27}$$

$$\frac{dF_s}{dt} = -F_s\Big[k_{3a}nB_0 + \frac{k_{2a}}{M}(nv_0 - v_1)\Big] + v_1k_d - uF_{in}, \tag{4.28}$$

$$\frac{dF_{in}}{dt} = k_{in}v_1 - uF_{in}. \tag{4.29}$$

We are able show that the above averaged model, is equivalent to the full model from Section 4.2. Figure 4.2 shows the temporal dynamics of both the full and averaged model superimposed upon one another. The dynamics of the full model in blue, are mimicked by the averaged model shown in red. Initial and subsequent bonding rates increase linearly for 1.5 hours before reaching steady state, at which point binding rates and internalisation rates reach an equilibrium.

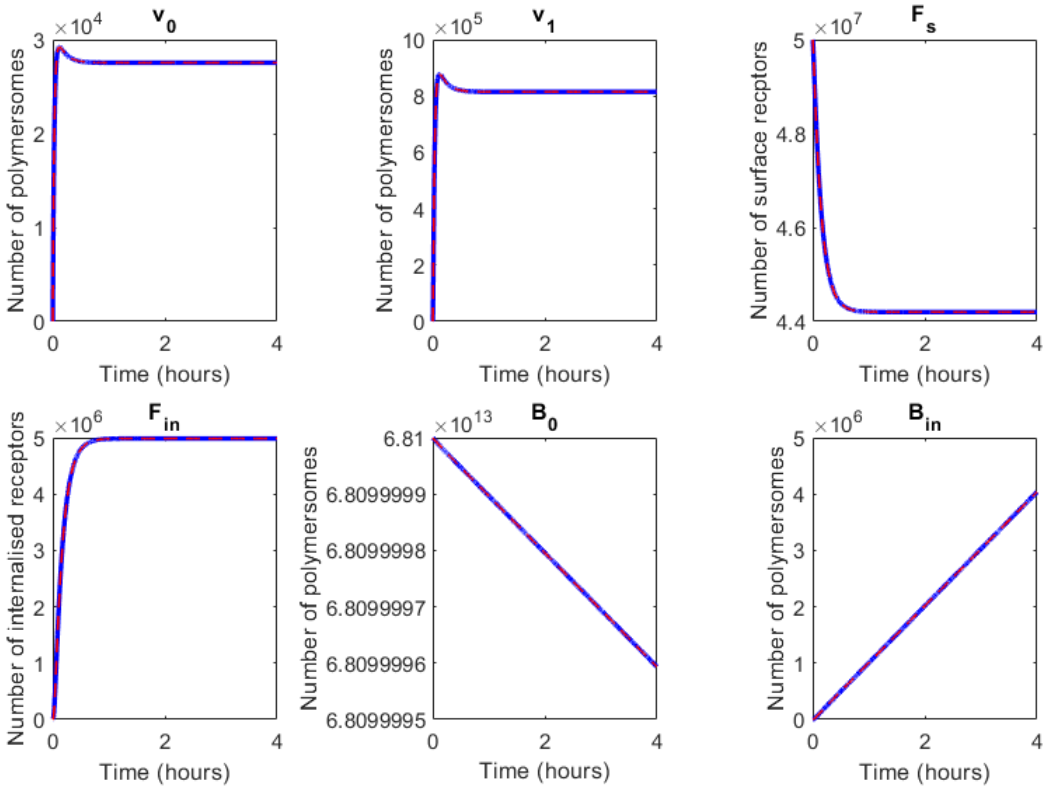

Figure 4.2: Temporal dynamics of the averaged model in red, and full model in blue are shown to be the same for each of the key variables within the model. Steady state is reached at 1 hour, where the binding and internalisation rates reach equilibria.

4.5 Defining aggregation of bond distribution

The use of statistical moment closure in the previous section allowed us to reduce the number of equations required to model the system. The use of the four statistical moments described in Section 4.3 also allows some insight into polymersome distribution, which we gain by calculating metrics which describe the aggregation for a given parameter set. Alongside the statistical moments, this is a beneficial tool to help better design polymersome characteristics in order to optimise delivery. For example, if it was found that bond distribution was aggregating towards a low number of average bonds forming, it may be experimentally desirable to increase binding affinity, to promote subsequent bonding. This could be an issue if it was found that internalisation was correlated with the number of bonds formed for example. On the contrary, if it was found that bond distribution was aggregating towards a large average number of bonds, you may instead wish to look at ways to increase the rate of internalisation vs subsequent binding as a way to promote polymersomes to enter the cells. The purpose of this section is therefore to better understand how the distribution of bound polymersomes changes across the model parameter space.

A number of techniques exist for defining aggregation, where the method of choice will depend up on the type of data. Two methods which are relevant to the work in this chapter were described by Wilson et al [161]; the variance-to-mean ratio, and the coefficient of variation. For the Poisson distribution, the variance (σ^2), and the mean (μ) are equal, whereas for the negative binomial distribution, the variance and

mean are not equal. The variance-to-mean ratio is calculated as follows,

$$D = \frac{\sigma^2}{\mu}. \tag{4.30}$$

Referring back to the example distributions, a Poisson distribution will therefore have a variance-to-mean ratio equal to 1, whereas for a negative binomial distribution it will be greater then 1. We may therefore define an aggregated distribution, as one with $D > 1$, with larger values indicating an increased level of aggregation. A separate, but very similar, scale invariant measure of aggregation may be calculated by dividing the variance-to-mean ratio by the standard deviation, in order to obtain the coefficient of variance, namely,

$$c_v = \frac{\sigma}{\mu}. \tag{4.31}$$

As the measure is relative to the mean, it is particularly useful when comparing distributions on different scales. However, as our data will be on the same scale, we will chose the variance-to-mean ratio as our aggregation metric. We may however encounter an issue during the following scenario related to our model. For a given parameter set, a distribution may follow the shape of a highly aggregated negative binomial distribution, aggregating towards a lower number of bonds. We may also have a distribution which is mirrored and now instead aggregates towards a higher number of bonds due the imposed maximum number of bonds as shown in Figure 4.3.

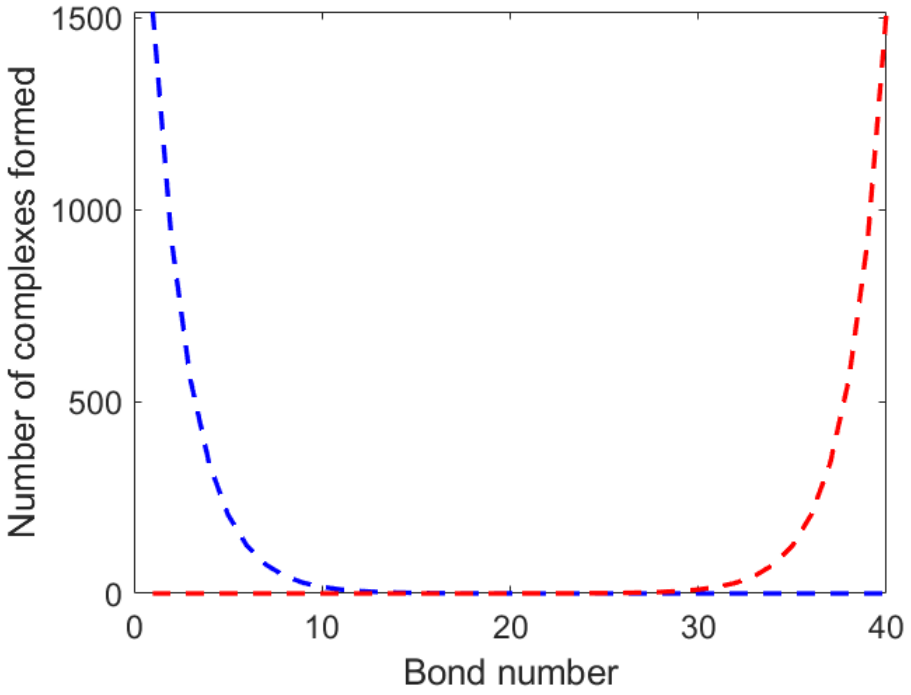

Figure 4.3: Two truncated distributions with equal variances, but different means. This gives different variance-to-mean ratios despite both distributions having equal levels of aggregation.

Both distributions have an equal variance, however the means will vary. This would lead to the distribution aggregated towards the lower bond numbers having a higher variance-to-mean ratio, despite both distributions having equal levels of aggregation. We there calculate a modified variance-to-mean ratio, which alleviates this issue. Where n is the maximum number of bonds from, we have,

$$MVM = \frac{|\mu - n/2|}{\sigma^2}. \tag{4.32}$$

As our distributions are truncated between 1 and 40, this metric ensures that scenarios such as those shown in Figure 4.3 is no longer an issue as equal mirrored distributions will not have the same value for our modified variance-to-mean ratio.

We now perturb relevant parameters in order to quantify their effect on aggregation. Within this section, we do not include k_d, as perturbing k_d in simulations showed little change to model dynamics. Similarly, we also do not perturb n, as the variance-to-mean ratio is not scale invariant, and therefore would not be a suitable metric for investigating n. Firstly, we look to Figures 4.4 and 4.5, which show the change in mean and variance by perturbing parameters between -90% to $+400\%$ of their original value. As discussed in the publication by Sorrell et al. [63], the parameter values estimated were one of a set of parameters which each fit *in-vitro* data. The set of parameters chosen was shown to minimise the error compared to other parameter sets. It is therefore possible, that the true set of parameters may exist out of the scope of this sensitivity analysis. However, without any additional experimental measurements, we must assume the current parameter set is correct. Figures 4.4 and 4.5 show that k_{3a} and u show a relatively small change to the mean and variance across the studied parameter space.

The increase in k_{3a} slightly decreases the mean number of bonds. This is due to an increase in initial binding, reducing the number of surface receptors available for subsequent bonds; however, this effect is minimal. Similarly, a reduction in u shows a decrease in the mean number of bonds, again due to a reduction in the number of surface receptors available to form subsequent bonds. However, an increase in u shows little change to both the mean and variance. For the more sensitive parameters, k_{2a} and k_{in}, we look in particular to Figure 4.6, which shows our modified variance-to-mean ratio.

In order to understand the direction of aggregation in Figure 4.6, we use a dashed

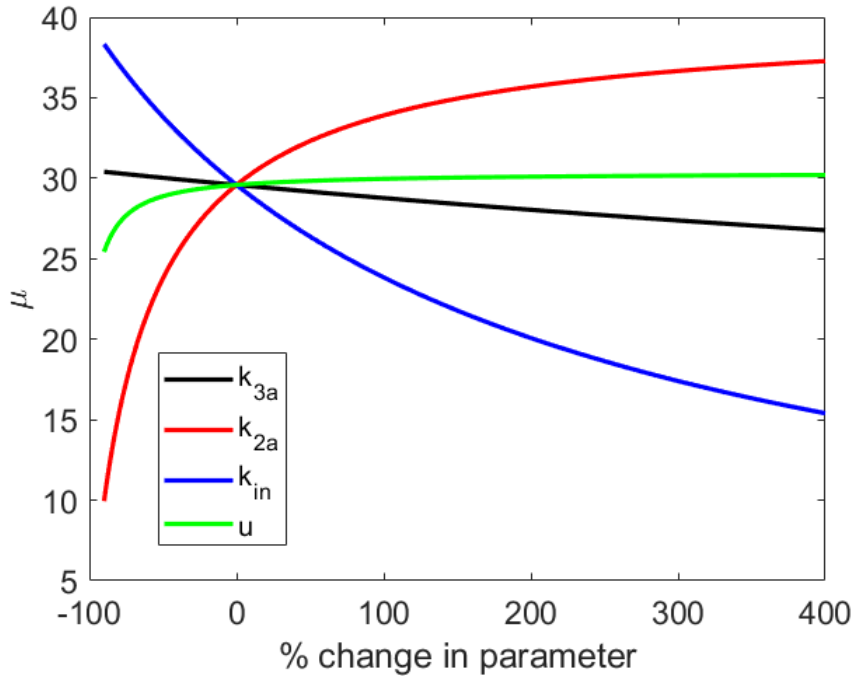

Figure 4.4: The change in the mean number of bonds at steady-state, formed by varying four key parameters between −90% to +400% of their original value.

line to indicate aggregated to the left, i.e. where the mean is less than $n/2$, and a solid line to indicate aggregation towards the right, where the mean is greater then $n/2$. The greatest levels of aggregation occur when k_{in} is reduced by 90%. While the variance is small, the mean is large leading to a large modified variance-to-mean ratio. Figure 4.7 shows the distribution of bonds with the largest level of aggregation. The distribution is heavily aggregated towards the higher number of bonds, with the majority of the complexes formed with the maximum (n=40) number of bonds. A reduction in k_{in}, leads to a reduction in the number of polymersomes internalised. As the rate at which subsequent bonds are formed is far greater than dissociation rate, the number of polymersomes forming subsequent bonds increases, causing the aggregation towards the higher number of bonds.

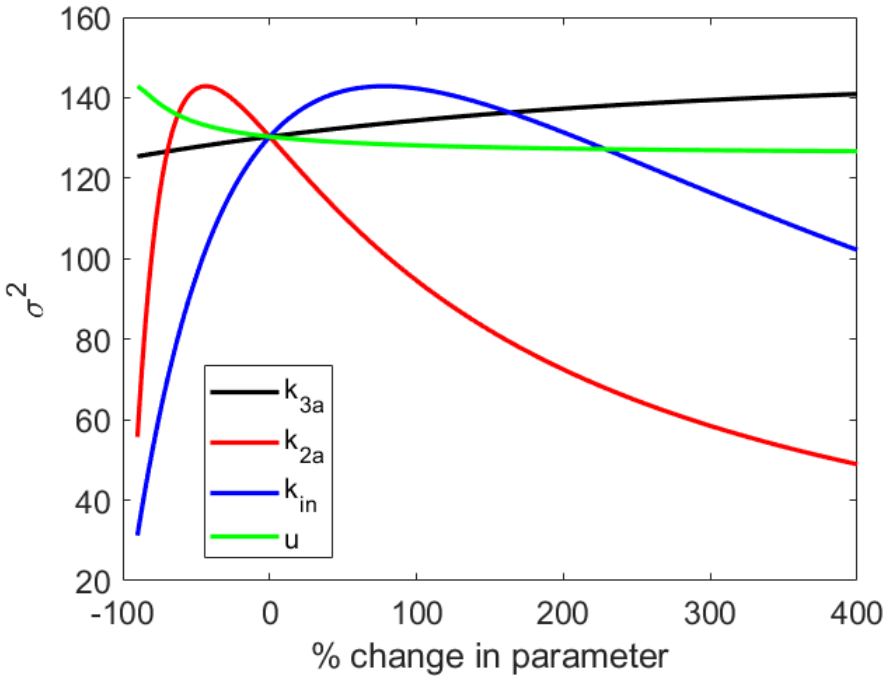

Figure 4.5: The change in the variance at steady-state, in the concentration of bonds formed by varying four key parameters between −90% to +400% of their original value.

Figure 4.7 shows the distribution with the greatest level of aggregation, found when the internalisation rate, k_{in}, is reduced by 90%. A similar shaped, heavily aggregation distribution can be found when increasing the 2D binding rate, k_{2a}. Reducing the internalisation rate leads to a reduction in the number of polymersomes which are internalised, and subsequently, an increase number forming subsequent bonds. Biologically, aggregation to either a lower number, and a higher number of bonds is caused by either polymersomes not binding, or bound polymersomes not being internalised with the exception begin an increase internalisation rate. It would therefore be describable to have a low level of aggregation.

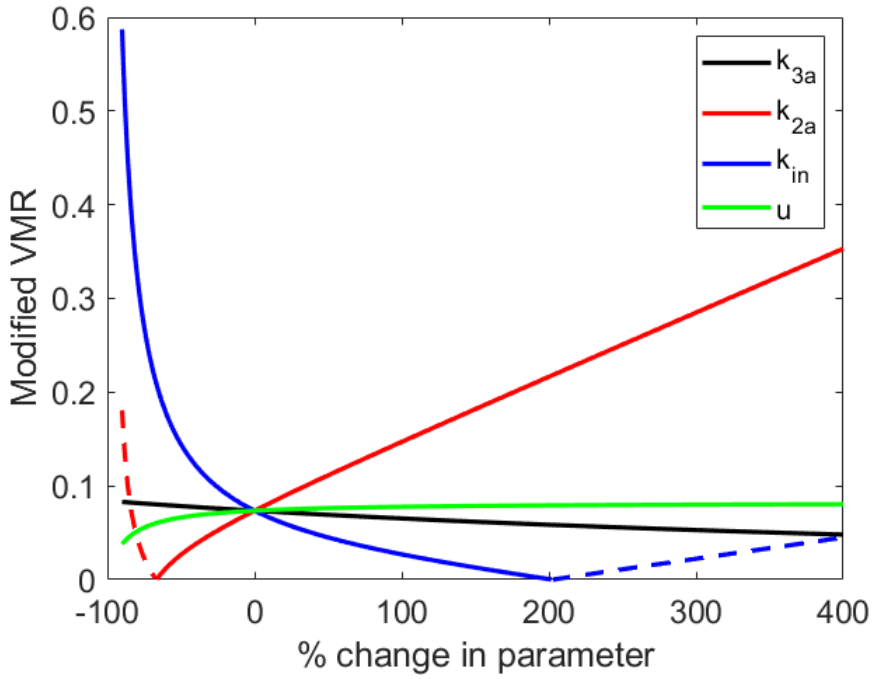

Figure 4.6: The change in the modified variance-to-mean ratio at steady-state, calculated using Equation 4.32. We perturb four key parameters between -90 to $+400$ of their original value. Dashed lines are used for both k_{2a} and k_{in} to distinguish between aggregation to the a lower number of bonds, as opposed to solid lines which indicates aggregation towards a higher number of bonds.

4.6 Spatial application of model

The model for polymersome uptake described in Sections 4.2-4.4 is dependent on time only. This is a suitable simplification for what is observed *in-vitro* with a monolayer culture, i.e. where all cells are exposed to the same concentration of polymersomes. However, it has been shown that 3D cultures exhibit intrinsic properties not found in monocultures, and more closely mimic what would be found *in-vivo* [162, 163, 164, 165]. The success of anti-cancer therapies has been shown to be influenced by structural heterogeneity, and oxygen, glucose and pH gradients, which are found in both tumours and spheroids of cancer cells [166]. This has been highlighted in a

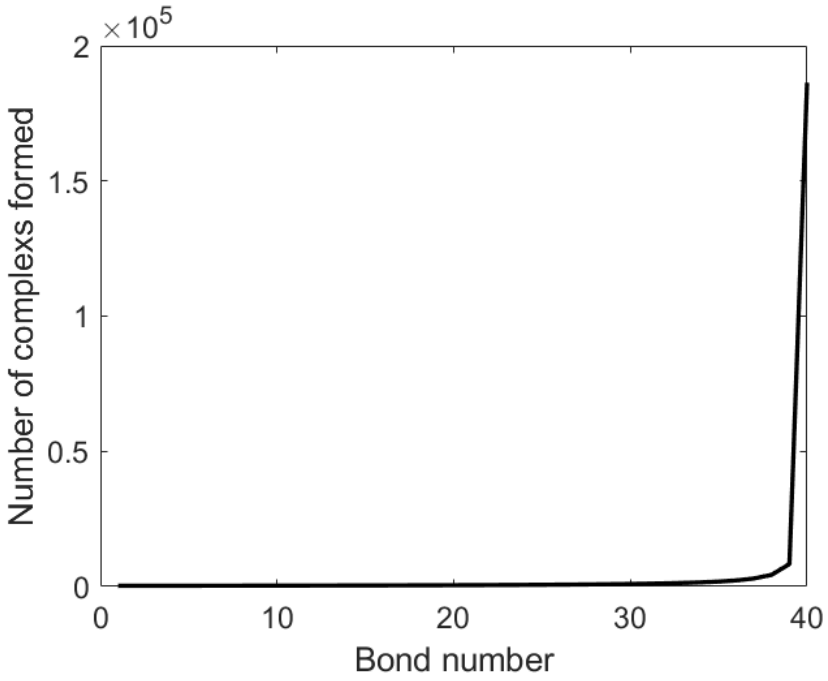

Figure 4.7: The distribution of bonds with the highest level of aggregation. This occurs when k_{in} is reduced by 90%. All other parameters and initial conditions are as described in Tables 4.1 and 4.2 respectively.

number of papers which showed that anti-cancer drugs were less effective on spheroids then monolayer cultures [167, 168], alluding to the fact that features only present in 3D models, such as the aforementioned pH, oxygen and glucose gradients, may affect a drugs efficacy. Another possible limitation of anti-cancer drugs, is the ability to penetrate deep within the tumour, which may only be detected on 3D models rather then monolayer cultures.

In this section, we explore a more physiologically relevant model, with the addition of a spatial element. We begin by introducing the theory, which allows us to modify the model described in Section 4.2. A number of mathematical models for tumours make the assumption of spherical symmetry [13, 14, 15, 16], choosing to only focus on what happens radially. This will reduce the problem to a single spatial dimension

(in r), and we also adopt this simplification.

4.7 A spatio-temporal model of nanoparticle uptake

Goodman et al. [64] published a model on the spatio-temporal modelling of nanoparticle delivery to tumour spheroids. Goodman derived model parameters relating to the spheroid geometry, by taking cross sections of stained tumour spheroids which were assessed using imaging software. The radius of the cell and radius of the spheroid were derived manually, while porosity was derived by setting a threshold of pixel intensity, in order to determine the ratio of intra-and extracellular space. As in section **??**, spherical symmetry was assumed, and therefore diffusion of unbound nanoparticles was governed by an equation similar to Equation 1.14, with one difference; it was assumed that the nanoparticles may only diffuse in the extracellular space (i.e. the gaps between the cells), and therefore the addition of porosity term, ϵ, was considered. The model is comprised of four partial differential equations which describe the spatio-temporal distribution of unbound, bound, and internalised nanoparticles and unbound surface receptors. Model binding parameters were determined by fitting to experimental data.

The first term is the porosity, ϵ, given as the ratio of intracellular to extracellular volume. This term is necessary as larger particles, such as polymersomes, may only diffuse extracellularly. Secondly, it allows us to take into account heterogeneous architecture with respect to radial distance, as shown in Figure 4.8. For example, tortuosity, τ, describes the ratio of the path taken to the Euclidian distance. An ap-

proximated relationship is given by Goodman et al. [64] between ϵ and the tortuosity $\tau(\epsilon)$,

$$\frac{1}{\tau(\epsilon)} = 1 - \frac{2}{3}(1+\epsilon)(1-\epsilon)^{-\frac{2}{3}}. \tag{4.33}$$

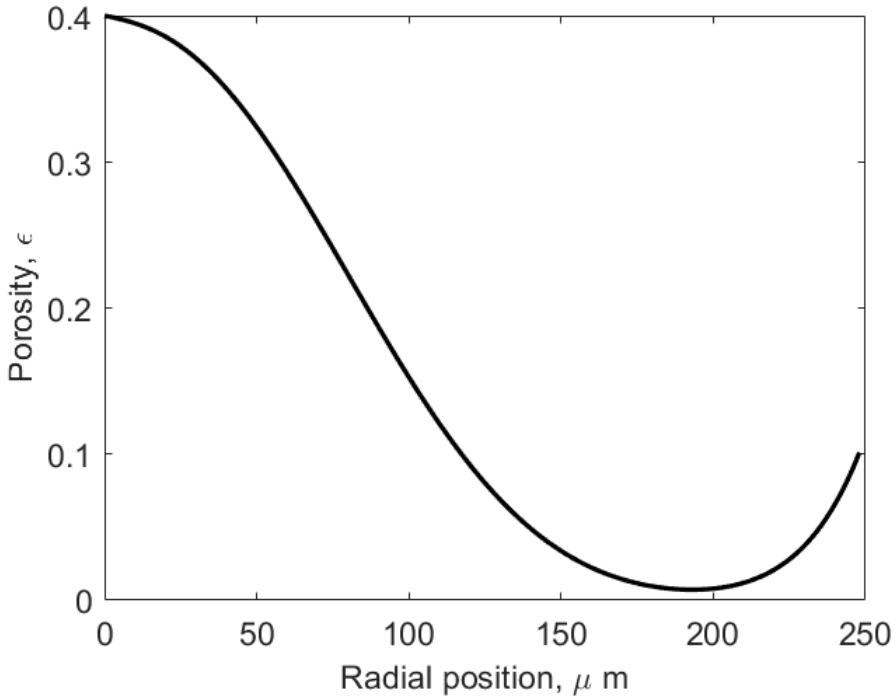

Figure 4.8: The spatial dependency of ϵ, and how it changes with radial position, for a spheroid with a radius of 248 μm taken from Goodman et al. [64].

The next term is $L(\lambda)$, which accounts for the hydrodynamic and steric reduction of the diffusion coefficient. As discussed in a publication by Hansing et al. [169], the extracellular matrix can have an effect of the diffusivity of nanoparticles through both steric, and hydrodynamic interactions. A steric interaction accounts for the collision of diffusing particles with the extracellular matrix fibres, while a hydrodynamic interaction accounts for the slowing of particles due to restricted thermal motion while moving near fibres. Work by Stylianopoulos et al. [170] looked at quantify theses

effects on the diffusivity of particles. The value of λ is as the ratio of the particle radius, α, and pore size, r_p. The idea is that the value of the diffusion coefficient is reduced to 0 if the particle radius, α, is larger then the extracellular pore radius r_p. As the pore radius is found to be spatially dependent, then so is $L(\lambda)$. We define $L(\lambda)$ as follows,

$$L(\lambda) = (1-\lambda)^2(1 - 2.1044\lambda + \lambda^3 - 0.948\lambda^5). \tag{4.34}$$

Figure 4.9 shows how $L(\lambda)$ changes with respect to λ.

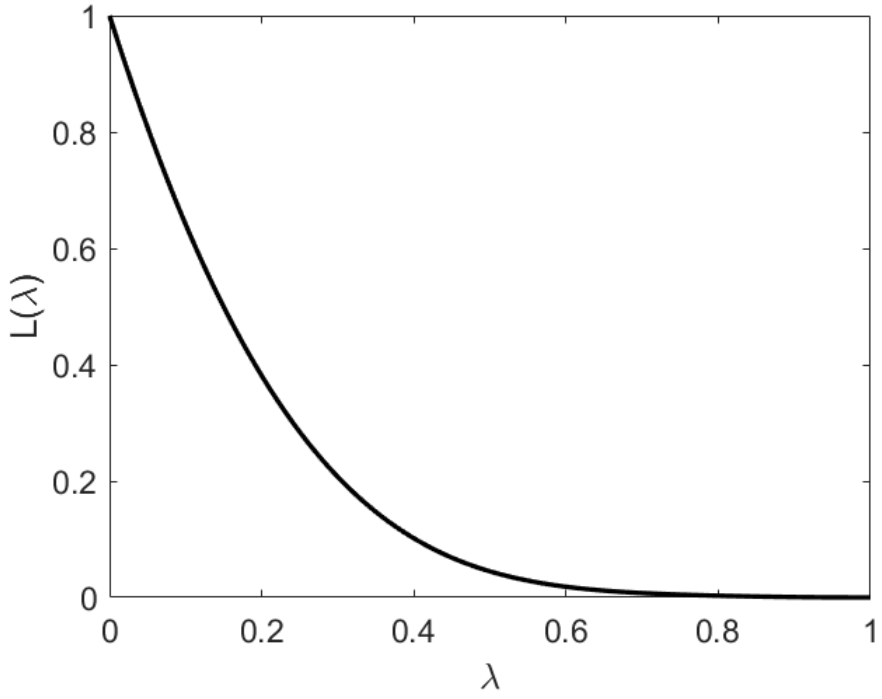

Figure 4.9: The hydrodynamic and steric reduction of the diffusion coefficient changes with different values of λ. As the λ gets close to 1, i.e. the particle radius α is only marginally smaller then pore radius r_p, there is large reduction in the diffusion coefficient.

Finally, Goodman et al. [64] describes a method for calculating an effective diffusion coefficient, D, by utilising Equations 4.33 and 4.34, namely,

$$D = D_0 \frac{L(\lambda)}{\tau(\epsilon)}, \tag{4.35}$$

where the diffusion coefficient, D_0 is calculated using the Stokes-Einstein expression [9], a method for determining the diffusion coefficient of spherical particles through liquids with a low Reynolds number,

$$D_0 = \frac{k_B T}{6\pi\mu\alpha}, \tag{4.36}$$

where k_b is the Boltzman constant, T is absolute temperature, μ is the viscosity and α is the particle size.

Using these ideas we can modify our nanoparticle system to extend it to a radially symmetric spheroid. Additionally, the movement term in Equation 4.37, and 3D binding term in Equations 4.37, 4.38 and 4.41 each contain an ϵ (the ratio of intracellular to extracellular volume), to account for these processes taking place extracellularly. For simplicity, we also rescale a number of terms in the model, i.e. we rescale both receptor terms, F_s, F_{in}. $\tilde{F}_s = F_s M$, where M is the concentration of cells, to change the units from receptors $\mu\mathrm{L}^{-1}$ to receptors/cell for more interpretable results. It is assumed that cells in the spheroid remain static with a fixed radius, and therefore the only equation that will be modified to include the movement term is Equation 4.1, i.e. the rate of change of unbound polymersomes. It is also assumed that the radius

of the spheroid does not change over time. The system may therefore be described as follows,

$$\frac{\partial B_0}{\partial t} = \frac{1}{r^2}\frac{\partial}{\partial r}\Big[D\epsilon r^2 \frac{\partial}{\partial r}\Big(\frac{B_0}{\epsilon}\Big)\Big] - \frac{k_{3a} n B_0 F_s M}{\epsilon} + k_d B_1, \tag{4.37}$$

$$\frac{\partial B_1}{\partial t} = \frac{k_{3a} n B_0 F_s M}{\epsilon} - k_d B_1 - \frac{k_{2a}}{M}(n-1) F_s B_1 + 2k_d B_2 - k_{in} B_1, \tag{4.38}$$

$$\frac{\partial B_i}{\partial t} = \frac{k_{2a}}{M}(n-i+1) F_s B_{i-1} - i k_d B_i - \frac{k_{2a}}{M}(n-i) F_s B_i \tag{4.39}$$

$$+ (i+1) k_d B_{i+1} - k_{in} B_i, \ i = 2, ..., n-1$$

$$\frac{\partial B_n}{\partial t} = \frac{k_{2a}}{M} F_s B_{n-1} - n k_d B_n - k_{in} B_n, \tag{4.40}$$

$$\frac{\partial F_s}{\partial t} = \frac{k_{3a} n B_0 F_s M}{\epsilon} - \frac{k_{2a}}{M} F_s \sum_{i=1}^{n-1}(n-i) B_i + k_d \sum_{i=1}^{n} i B_i + u F_{in}, \tag{4.41}$$

$$\frac{\partial F_{in}}{\partial t} = \sum_{i=1}^{n} k_{in} B_i - u F_{in}, \tag{4.42}$$

$$\frac{\partial B_{in}}{\partial t} = \sum_{i=1}^{n} k_{in} B_i. \tag{4.43}$$

Variable	Initial value	Units
F_s	1000	Receptors cell^{-1}
F_{in}	0	Receptors cell^{-1}
B_0	6.81×10^1	Polymersomes μm^{-3}
B_1,...,B_n	0	Polymersomes μm^{-3}
B_{in}	0	Polymersomes μm^{-3}

Table 4.4: Rescaled initial conditions and units for spatial model.

Parameter	Value	Units
k_{3a}	2.333×10^{-9}	μ m^3 receptors^{-1} sec^{-1}
k_{2a}	3.1667×10^{-5}	cells receptors^{-1} sec^{-1}
k_{in}	0.0102	sec^{-1}
k_d	6.25×10^{-27}	sec^{-1}
n	40	dimensionless
u	0.0017	sec^{-1}
M	2.3873×10^{-4}	cells μ m^{-3}
k_B	1.38×10^{-23}	m^{2}kg s^{-2}K^{-1}
T	273	K
μ	6.92×10^{-4}	kg m^{-1}s^{-1}
α	1×10^{-7}	m

Table 4.5: Rescaled parameter values and units for spatial model.

We can use the set of binding parameters parameters given in Table 4.5, the movement parameters taken from Goodman et al. [64] described in Equations 4.33-4.36, and the initial conditions in Table 4.4 for all points in space except for B_0. For B_0 we initially have,

$$B_0(r, 0) = 0, \tag{4.44}$$

and the following boundary conditions,

$$\frac{\partial B_0}{\partial t} = \frac{\partial B_i}{\partial t} = \frac{\partial F_s}{\partial t} = \frac{\partial F_{in}}{\partial t} = \frac{\partial B_{in}}{\partial t} = 0 \quad \text{at } r = 0, \tag{4.45}$$

and

$$B_0(R, 0) = B_0 \quad \text{at } r = R, \tag{4.46}$$

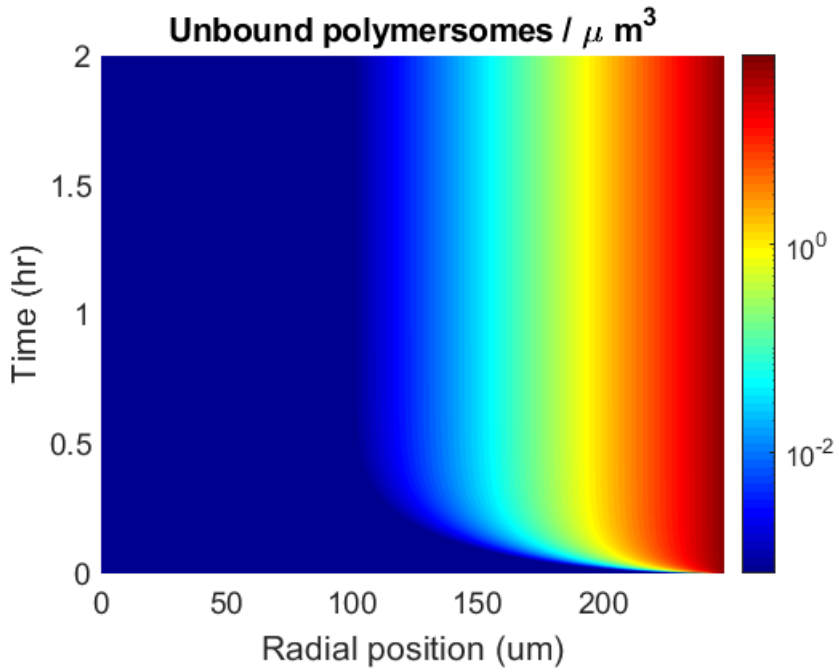

Figure 4.10: The spatio temporal distribution of polymersomes, using parameter and variable values found in Tables 4.5 and 4.4.

Figure 4.10 shows the spatio-temporal distribution of unbound polymersomes in the spheroid interior between 0 and 2 hours. At close to $r = 200\,\mu$m, there is a large reduction in the number of polymersomes. To better understand this, we may refer back to Figure 4.8 which shows the change in porosity, ϵ. We can see, that when ϵ minimises, less unbound polymersomes are present. As the assumption is made that polymersomes may only diffuse extracellularly, a reduction in the volume fraction of extracellular space reduces the polymersomes ability to permeate deeper into the spheroid. This leads to a significant reduction in the number of polymersomes permeating.

4.8 Statistical moment closure for spatial model

In Section 4.4, we showed, for the time-only model, that it was possible to use statistical moment closure in order to reduce the number of equations required to model the system. For the full and averaged model to be equal, we assumed that k_{in} remains constant, and that $k_d B_1 \approx 0$. By again making these assumptions, we are able to create the following reduced system of equations.

$$\frac{\partial B_0}{\partial t} = \frac{1}{r^2}\frac{\partial}{\partial r}\Big[D\epsilon r^2 \frac{\partial}{\partial r}\big(\frac{B_0}{\epsilon}\big)\Big] - \frac{k_{3a} n B_0 F_s M}{\epsilon} \tag{4.47}$$

$$\frac{\partial v_0}{\partial t} = \frac{k_{3a} n B_0 F_s M}{\epsilon} - k_{in} v_0 \tag{4.48}$$

$$\frac{\partial v_1}{\partial t} = F_s M\Big[\frac{k_{3a} n B_0 M}{\epsilon} + \frac{k_{2a}}{M}(n v_0 - v_1)\Big] - k_d v_1 - k_{in} v_1 \tag{4.49}$$

$$\frac{\partial v_2}{\partial t} = F_s M\Big[\frac{k_{3a} n B_0 M}{\epsilon} + \frac{k_{2a}}{M}\Big((2n-1)v_1 - 2v_2 + n v_0\Big)\Big] - (2v_1 - v_0)k_d ... \tag{4.50}$$

$$- k_{in} v_2$$

$$\frac{\partial F_s}{\partial t} = -F_s\Big[\frac{k_{3a} n B_0 M}{\epsilon} + \frac{k_{2a}}{M}(n v_0 - v_1)\Big] - \frac{k_d v_1}{M} + u F_{in} \tag{4.51}$$

$$\frac{\partial F_{in}}{\partial t} = \frac{k_{in}}{M} - u F_{in} \tag{4.52}$$

$$\frac{\partial B_{in}}{\partial t} = k_{in} v_0 \tag{4.53}$$

A comparison of the variables shared between the full model from Section 4.7, and the averaged model from this section are compared using parameters from Table 4.5 and 4.4 in Figure 4.11.

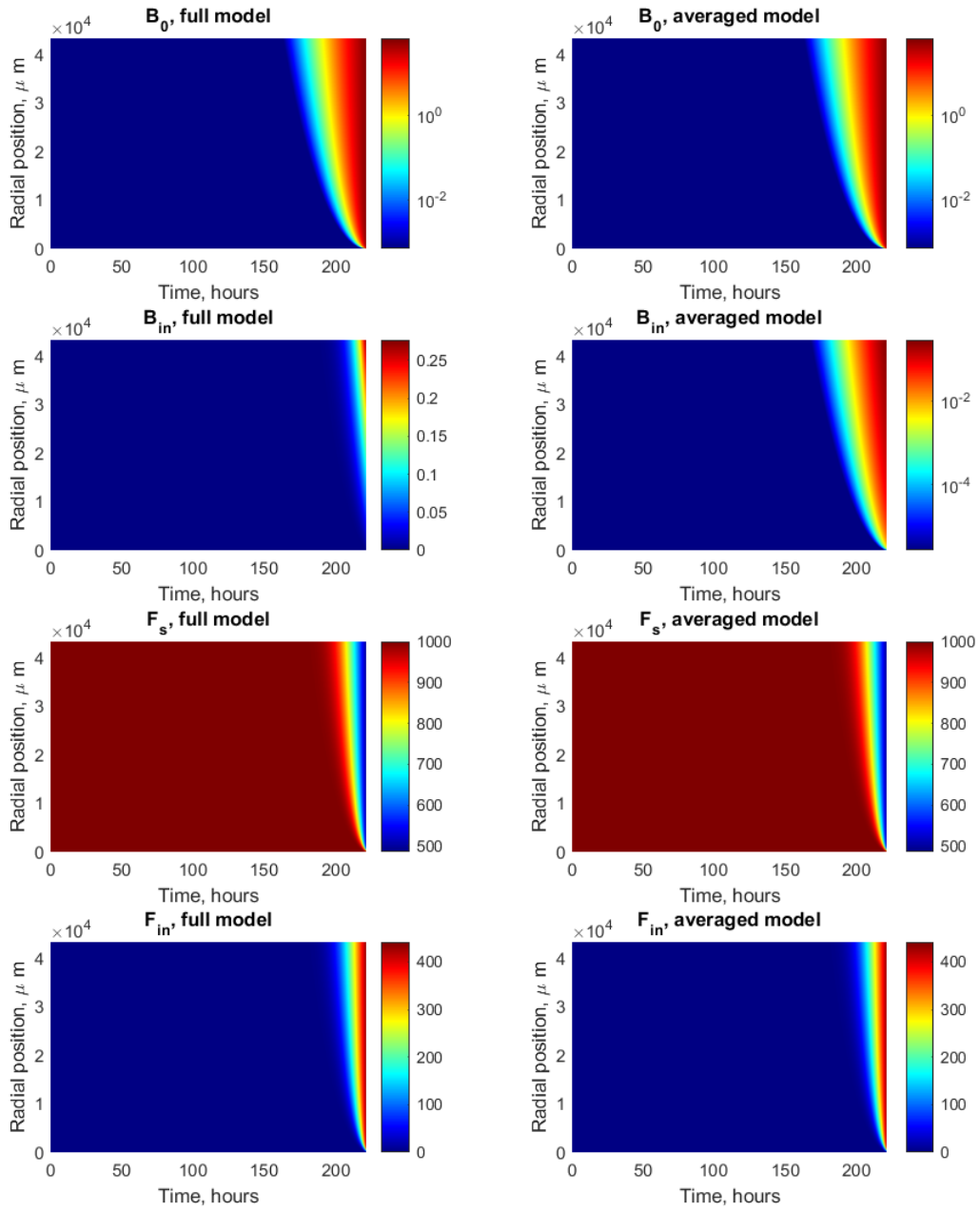

Figure 4.11: A comparison of the full model described in Section 4.7 for the four variables shared between the models. For each of these variables, the models each get the same solutions given the same set of parameters.

4.9 Calculating physiological parameters based on experimental data

Up to now, we have used a combination of parameter values from Goodman et al. [64] and Sorrell et al. [63] in order to predict the diffusion and uptake of the polymersomes. We are now in the position to start making predictions based on three forms of data provided by collaborators at the University of Sheffield as shown in Figures 4.12 and 4.13.

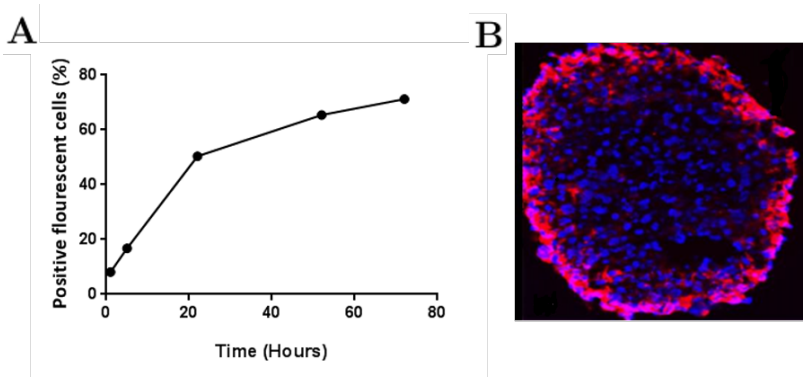

Figure 4.12: Figure A is experimental data showing the uptake of polymersomes into spheroids for a 72 hour time period. Figure B shows florescence staining of of cells containing polymersomes after 24 hours.

Figure 4.12A shows the percentage of FaDu cells which contained polymersomes over 72 hours. A monolayer of FaDu cells, which are pharynx cells with squamous cell carcinoma, were exposed to rhodamine labelled PMPC-PDPA polymersomes over a 72 hour period. The percentage of cells containing polymersomes was assessed by calculating the percentage of cells with a fluorescence above a given intensity. We use this data to compare to our model output, in order to reparametrise physiological parameters previously taken from Goodman [64], that have an effect on the diffusivity

of the polymersome, namely, pore radius, porosity and tortuosity.

Figure 4.12B shows internalised rhodamine labelled polymersomes in red, and counter-stained FaDu cell nuclei in blue. We use this to quantify the depth to which the polymersomes permeate after 24 hours.

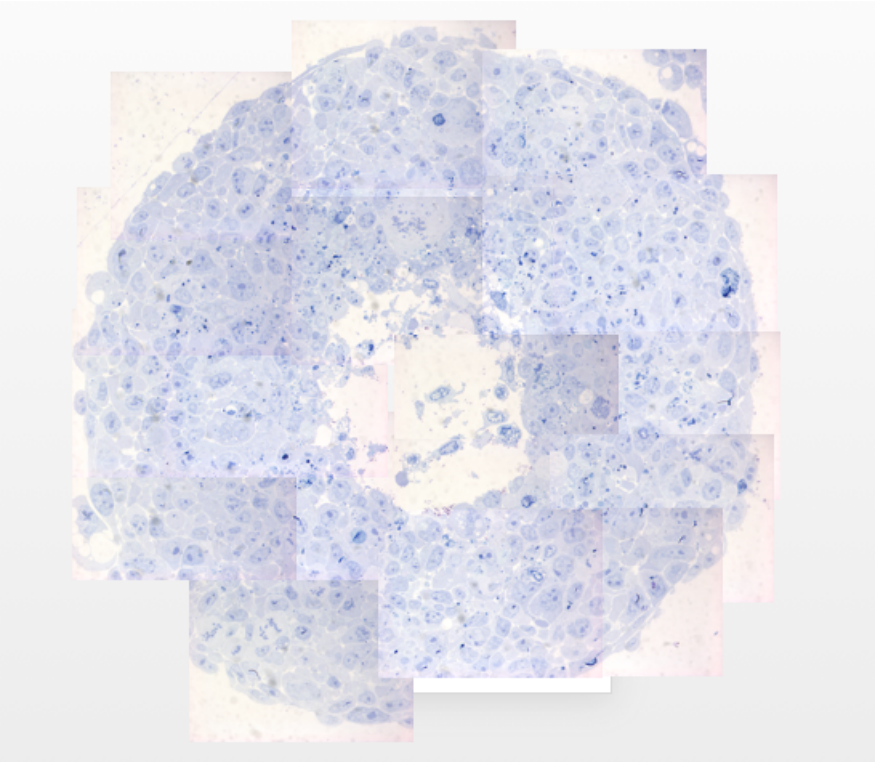

Figure 4.13: Slice of 4 day old methylene blue stained FaDu spheroid provided by collaborators at the University of Sheffield.

Figure 4.13 shows a 100x zoom image of a slice of 4 day old FaDu spheroid which is used to approximate the radius of the spheroid, and necrotic core.

The data provided was conducted on spheroids which appear to have large physilogical difference to that of Goodmans [64]. It is therefore necessary to re-parametrise some terms in the model, namely, porosity ϵ, tortuosity τ, pore size, r_p, and radius, R. Looking at the physiological parameters given by Goodman shows a tortuosity value of 4, which is far higher then upper bounds of estimates from the literature

[171]. A tortuosity value of 4 implies that the distance taken extracellularly, is four times that of the euclidean distance between two points. This would require highly irregular cell shapes, which is not present in cancer spheroids.

To begin, we must define the points which define geometry of the spheroid. To do so, we must find; the outer boundary points, inner boundary points (i.e. where the nectrotic core has formed), and cell nuclei. We are able do this using the image analysis software WebPlotDigitizer. Figure 4.14 shows the geometry created in Matlab, using the inner and outer boundary points, as well as the nuclei of the cells. We are now able to use these points, in order to generate a computational approximation of a spheroid geometry.

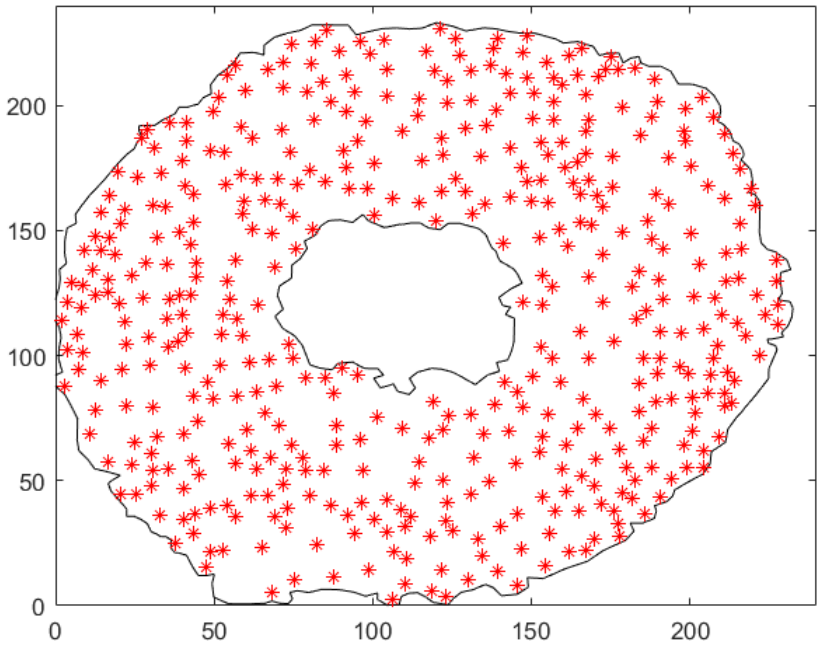

Figure 4.14: A computational representation of the inner and outer boundaries, as well as cell nuceli represented using red asterisks. This was generated using the image of the 4 day spheroid in Figure 4.13.

4.9.1 Voronoi tessellation for cell boundaries

In order to be able to calculate values for tortuosity and porosity, we need to be able to define cell boundaries. The method we chose, was to utilise a Voronoi tessellation, which has been shown to be a more effective method for estimating cell boundaries [172] than alternative methods such as watershed fragmentation [173].

Voronoi tessellation is a method that defines discrete regions in space, by finding the equidistance between neighbouring points in order to create a boundary. If we suppose, we have n nuclei, $2 \leq n < \infty$, in a planar region $X \in \mathbb{R}^2$. We may define our set of cell nuclei by the following,

$$P = \{p_1, p_2, ..., p_n\} \in \mathbb{R}^2. \tag{4.54}$$

Using some distance function d, we may call the Voronoi region, $V(p_i)$, that is generated from some point p_i [174, 175],

$$V(p_i) = \{x \in X | d(x, P_i) \leq d(x, P_j) \forall i \neq j\}. \tag{4.55}$$

To generate the Voronoi diagram, we calculate Equation 4.55 for $p_i \neq p_j$, and $i \neq j, \forall i, j = 1, 2, \ldots, n$. The region generated for $V(p_i)$ may be though of as $n - 1$ half-spaces, which contains p_i, bound by bisectors of p_i and its neighbouring points within P.

Figure 4.15 shows the bisector between two points, p_i, p_j, in order to generate their respective half-spaces $H(p_i, p_j), H(p_j, p_i)$.

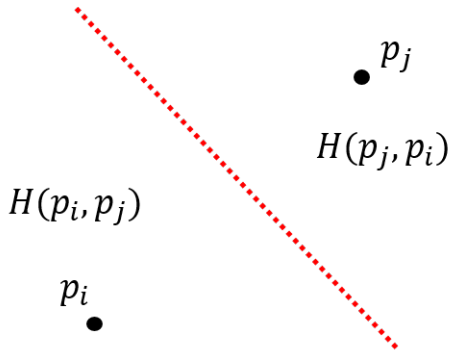

Figure 4.15: The red dotted line, represents the bisector between the two half-spaces $H(p_i, p_j), H(p_j, p_i)$. Each point in $H(p_i, p_j)$ is closer to p_i then p_j.

Looking at Figure 4.16a, where, $n = 3$, we can see that three bisectors are formed, between points p_i, p_j and p_k. Clearly, these bisectors will continue to infinity. Therefore, in order to generate the Voronoi diagram, we must terminate a bisector where it intercepts the bisector of a different pair, or an imposed boundary like in Figure 4.16b in the centre. Using inner and outer boundaries shown in Figure 4.14, we may

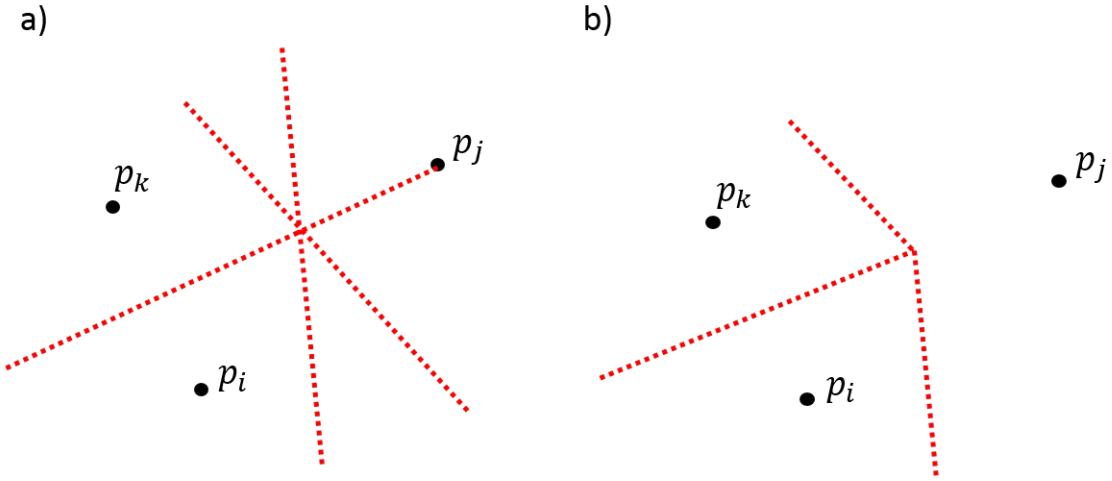

Figure 4.16: The red dotted lines show the 3 bisectors of the points p_i, p_k and p_k. To form the Voronoi diagram, we terminate a bisector at the point it intersects another bisector.

generate the spheroid geometry shown in Figure 4.17.

Now our spheroid geometry is defined, we are able to start estimating tortuosity and

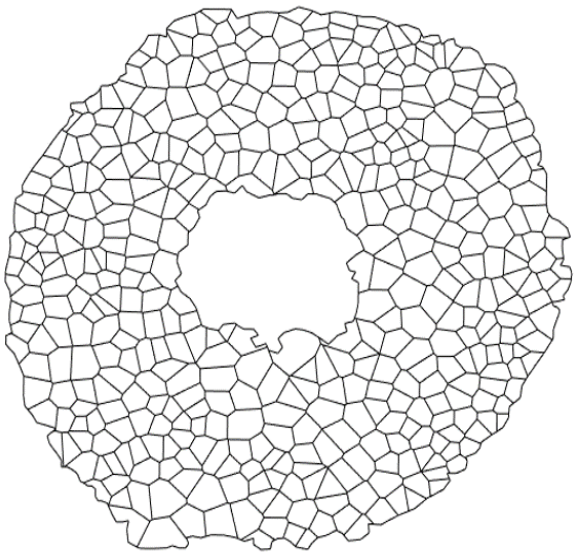

Figure 4.17: An estimation of the of 2D spheroid geometry. Inner and outer boundaries we digitised from spheroid images, as were nuclei points. The boundaries of the cells were then estimated using Voronoi tessellation.

porosity. Firstly, a simple term to calculate are the spheroid radius, R, and the radius of the necrotic core, R_c. Straightforward measurement from the image gives a spheroid radius of R=116.255 μm, and a core radius of R_c = 5.3454 μm.

The second term we will investigate is tortuosity, τ. In order to calculate τ, we make use of the graph that has been generated from the Voronoi tessellation. To do so, we select a node and find all nodes that exist within a given Euclidean radius of it. We then find the shortest distance to all nodes within the selected region, and calculate the tortusoity as a ratio of the Euclidean distance to the path taken. We complete this process for each node within the graph and calculate the tortuosity as a mean of all ratios. Figure 4.18 shows how the tortuosity value changes as we change the Euclidean distance used. We wish to reduce the size of the errors bars while keeping as many points within 1 standard deviation in order to reduce uncertainty. The value chosen was 30 as above, which is approximately twice the size of the largest node (i.e.

longest cell boundary side), while still being smaller then the necrotic core (this can cause abnormally large τ values). For the region radius set to 30 μm, we calculate the tortuosity for all points, and calculate the mean, as shown in Figure 4.19. Figure 4.19 shows each of the ratio's calculated and their respective radial positions. We then set τ equal to a piecewise function, such that,

$$\tau(r) = \begin{cases} 1 & \text{if } r < R_c, \\ 1.2136 & \text{if } r \geq R_c. \end{cases}$$

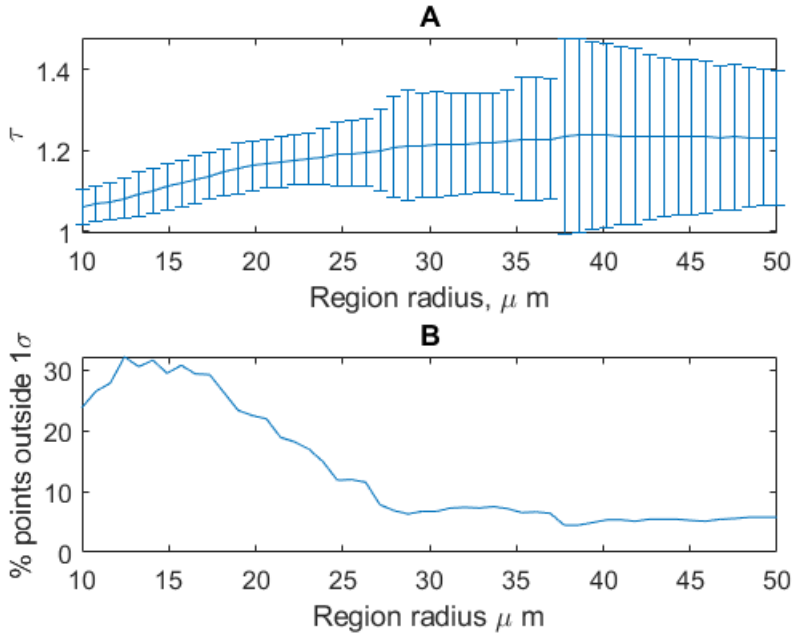

Figure 4.18: Image A shows how the tortuosity, τ changes by selecting different region radii to sample from. Image B then shows, for each of the region radii selected, how many points have tortuosity values which fall outside 1 standard deivation of the tortuosity value calculated.

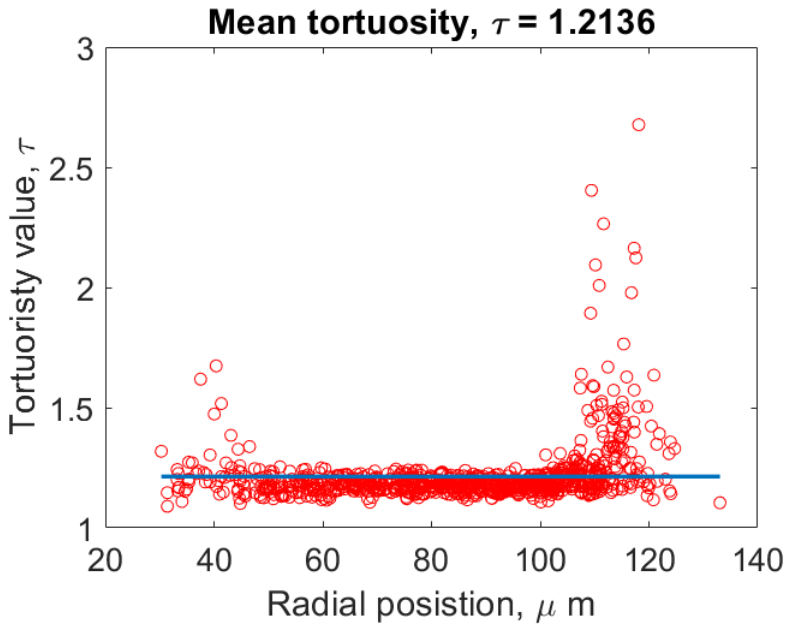

Figure 4.19: All tortuosity values calculated for a region radius of 30 μm with respect to the nodes radial position. A mean tortuosity value could then be calculated which was found to be $\tau = 1.2136$.

4.9.2 Calculation of porosity

The final term we wish to calculate is ϵ, the fraction of the extracellular volume. An assumption is made that a 2D slice is an adequate representation of the spheroid geometry. Using the Voronoi diagram produced in the previous section, we may calculate the area of the spheroid using MATLAB's *PolyArea* function to be 42,234 μm^2. The area excluding the necrotic core accounts for 38,272 μm^2. Again, making use of the Voronoi diagram, the sum of the non boundary edges is 7799.6 μm^2. The value of ϵ can be calculated a piece-wise function, where, if r is less then the radius of the necrotic core, $\epsilon = 1$. If r is greater then, or equal to the radius of the necrotic

core, then we may calculate epsilon as,

$$\epsilon(r) = \frac{2 \times 7799.6 \times r_p}{38272}. \tag{4.56}$$

We must first calculate a value for the radius of the pore, r_p. To do so, we make use of data shown in Figure 4.12 which show the percentage of cells containing polymersomes after over a 72 hour peroid, and the depth permeated after 24 hours. Figures 4.12A and 4.12B were produced from spheroids with a radius of 221 μm, therefore, we increase our model radius to 221 μm and we therefore scale the radius of our necrotic core by a factor of 221/116.2555 (i.e. scaled by the ratio of the radii of the two spheroids).

We begin by splitting our spheroid into q equally spaced points on a straight line from the centre to the boundary r as shown in Figure 4.20. We can use this to create $q-1$ annulus, where a given annulus j exists between points r_j and r_{j+1}.

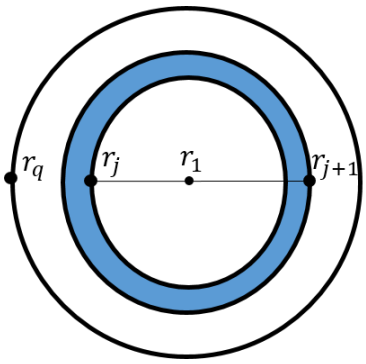

Figure 4.20: In order to estimate the radius of the pore size, r_p, we divide our spheroid into annulus. We have a total of q points which will lead to $q-1$ annulus. The blue area highlighted shows annulus j which is found between points r_j and r_{j+1}

For each annulus, we can calculate $B_{int}(j)$, the number of internalised polymersomes

in a given annulus, and $M_c(j)$ and the number of cells in annulus j, defined as,

$$B_{int}(j,t) = 4\pi \int_{r_j}^{r_{j+1}} r^2 B_{in}(r,t)\, dr, \tag{4.57}$$

$$M_c(x) = 4\pi \int_{r_j}^{r_{j+1}} r^2 m\, dr. \tag{4.58}$$

We are then able to calculate the total number of polymersomes per cell $P(j,t)$ for a given annulus by calculating $B_{int}(x,t)/M_c(x)$. As our calculation for the total number of polymersomes per cell is continuous, we need to assign some type of threshold to say whether cells in a given annulus contains polymersomes. We define a function,

$$h(j,t) = \begin{cases} 0 & \text{if } P(j,t) < \text{threshold}, \\ \\ 1 & \text{if } P(j,t) \geq \text{threshold}. \end{cases}$$

The function $h(j,t)$, is a binarising function that will allow us to calculate the number of cells containing polymersomes, by multiplying $M_c(j) \times h(j,t)$. We may also calculate the number of polymersomes per cell by multiplying $P(j,t) \times h(j,t)$. The percentage of cells containing polymersomes is given as,

$$\%\,\text{cells containing polymersomes} = \frac{\sum_{j=1}^{q} h(j,t) \times M_c(x)}{4\pi \int_0^R r^2 m\, dr}. \tag{4.59}$$

Figure 4.21 shows the sum of squared errors between the output for a given threshold value and r_p when compared to the data from Figure 4.12A. We can see for a given threshold value, we have a pore radius which would be best fitting to the data. With this, we find that the lowest SSE is found for $r_p = 0.1071$ μ m with a threshold value

of 1.6327 polymersomes/cell as highlighted in Figure 4.21.

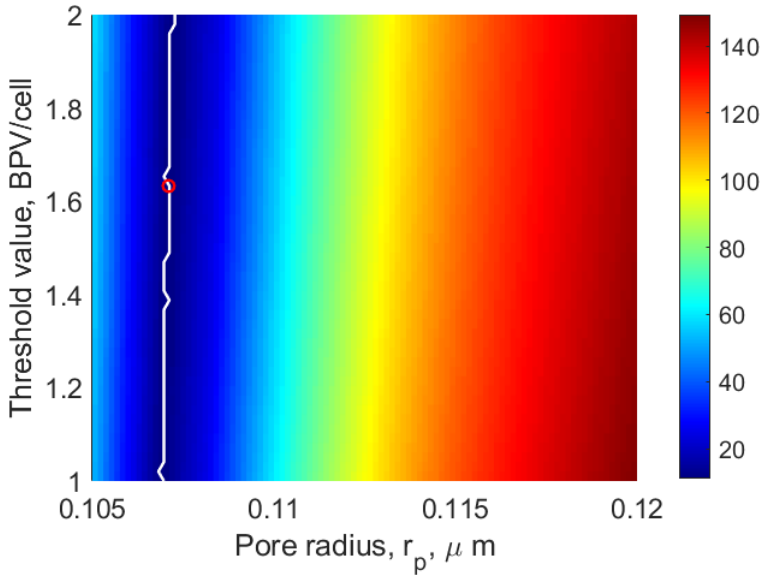

Figure 4.21: How the sum of squared errors changes for differing threshold and pore radii values when compared to data shown in Figure 4.12A. The white line shows the pore radii, which best fits the data for a given threshold value. The pair which minimises the SSE is highlighted in red with $r_p = 0.1071\mu m$, and a threshold value of 1.6327 polymersomes/cell.

We are now able to use the above value of r_p, with equation 4.56 to generate the following piecewise function for ϵ.

$$\epsilon(r) = \begin{cases} 1 & \text{if } r < \text{core boundary}, \\ 0.0115 & \text{if } r \geq \text{core boundary}. \end{cases}$$

Figure 4.22 shows the model output, using the pore radius and threshold values selected in Figure 4.22, with the data points shown in Figure 4.12A. The model predicts that after 72 hours, 74.45% of cells will contain polymersomes, while the data suggests 71.66% cells will contain polymersomes. To better visualise where the binding is taking place, we make use of the the Voronoi diagram generated in Section

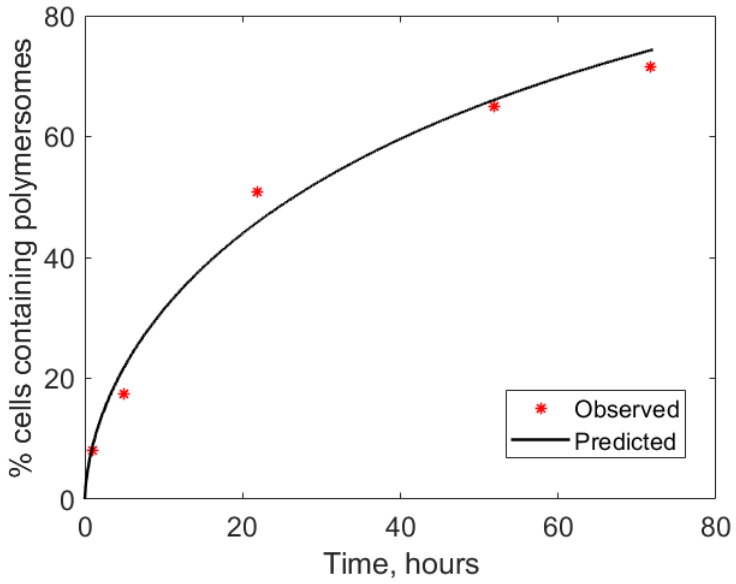

Figure 4.22: Model output using best fitting pore radius (0.1071 μm) and threshold (1.6327 polymersomes/cell) values, along with the data previously shown in figure 4.12A.

4.9.1, along with the model output to generate Figure 4.23. Figure 4.23 shows the total number of internalised polymersomes per cell at six different time points. The number of polymersomes in each of the cells was estimated by calcuating the distance from the cell to the boundary, and assigning it to a specific annulus. Polymersomes per cell in a given annulus can then be calculated using Equations 4.57 and 4.58 for a given time point.

At 1 hour, few polymersomes have permeated the spheroid and therefore only cells on the outer boundary internalise polymersomes. After 24 hours, polymersomes have permeated deeper into the spheroid and have been internalised by cells closer to the core. After 72 hours, a greater number of cells now contain polymersomes, with only cells close to the necrotic core not containing any, while cells on the outer boundary contain approximately 10,000 polymersomes each.

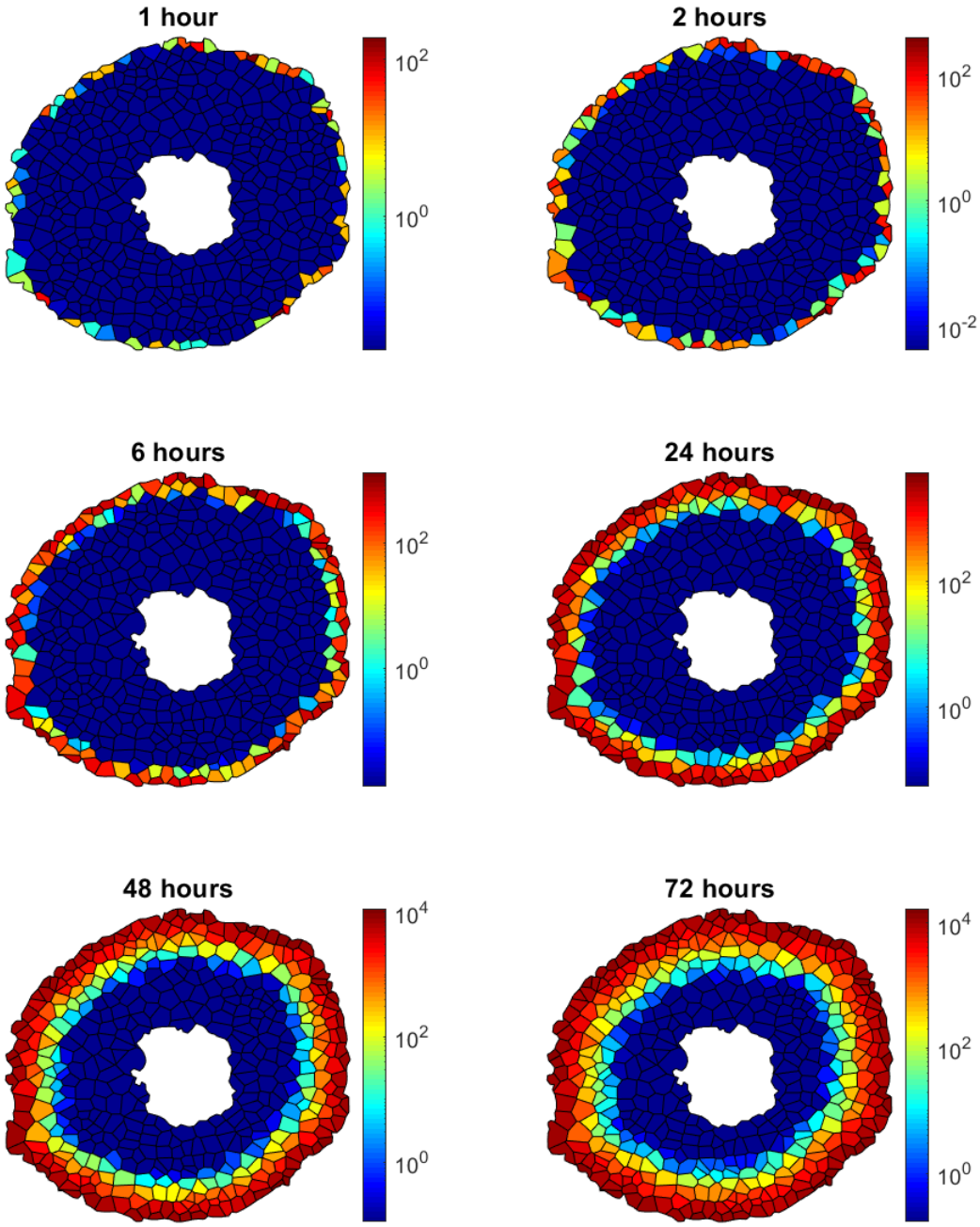

Figure 4.23: Prediction of the number of internalised polymersomes per cell at 6 different time points. The geometry was generated using the Voronoi Tessalation in section 4.9.1. For each cell, the number of internalised polymersomes was predicted by calculating the distance from the cell nucleus to the outer boundary. Units for all images are polymersomes/cell.

4.10 Varying pore radii

It is well understood that the spheroid physiology changes with culture time. During the initial growth stage of the spheroid, growth is limited by the consumption and supply of nutrients and oxygen which enter via diffusion [164]. The increasing spheroid radius leads to hypoxia within the centre, which has been shown to form a necrotic core when the radius > 150 μm [176]. The extracellular matrix (ECM) is subject to constant remodelling by matrix-degrading enzymes released by cells. Further stress may be placed up on the ECM by the cells migrating to regions in which they can proliferate [177]. Cell adhesion and apoptosis are closely linked [178]. It is therefore expected, that older spheroids may have larger extracellular gaps. As the diffusion coefficient in our model is calculated using the Stokes-Einstein equation with a hydrodynamic and steric reduction term, an increase in the size of the gap leads to an increased rate of diffusion. This in turn leads to an increase in the depth to which the polymersomes permeate. In order to quantify what difference this makes, we instead look towards images of spheroids cultured for 7 days.

Due to the scale of intracellular gaps compared to the scale of the overall spheroid, we must use transition electron microscopy (TEM) images of 7-day spheroids in order to assess ranges for the poire radius parameter in the model, r_P. Figure 4.24 shows a TEM image of a 7-day spheroid at 890x zoom. In order to measure the diameter of the extracellular gaps, we utilise *WebPlotDigitizer*'s measurement tool, which allows the user to measure the number of pixels in a reference scale bar. The user may then measure the number of pixels in the intracellular gaps across the image to

approximate the size of the intracellular gap. For Figure 4.24, 46 spatial measurements were taken at various points of the image. It was found that the pore radius, $r_p = 0.1426 \pm 0.296\,\mu$m.

For the purpose of the following simulations, it is assumed that the only characteristic that varies between the 4-and 7-day spheroids is the size of pore radius, r_p. As concentrations of both extracellular and intracellular polymersomes are higher at points closer to the external boundary, a binarising function (like that found in Section 4.9.2) can be used to calculate the depth to which the polymersomes permeate. Figure 4.25 shows the depth to which polymersomes were internalised for r_p values equivalent to 4-and 7-day spheroids. For the 7-day spheroid, we see polymersomes being internalised at a far greater rate when compared to the 4-day spheroid. After 20 hours, we see the depth infiltration levelling off, at the point at which all cells contain polymersomes. This may be confirmed visually by looking at Figure 4.26, which shows a prediction of the number of internalised polymersomes. We can see that at 24 hours, most cells contain polymersomes.

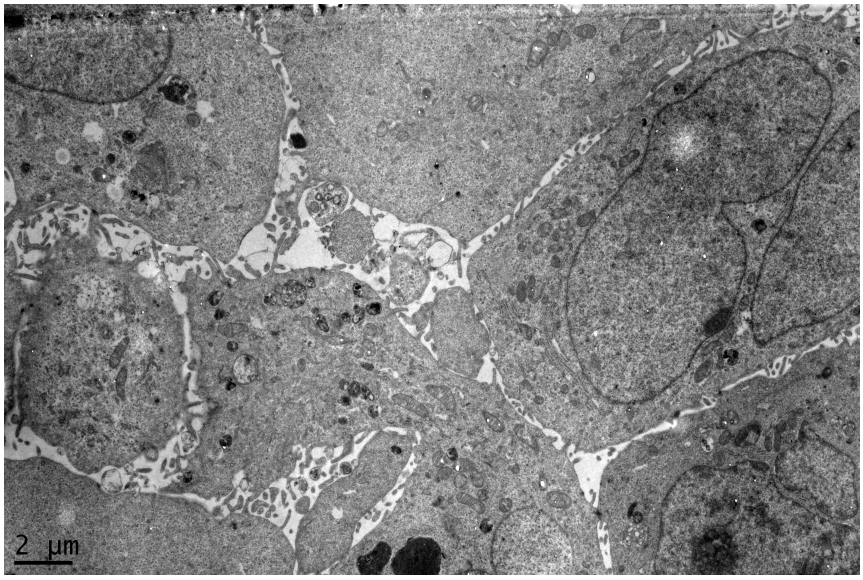

Figure 4.24: TEM image of a 7 day old spheroid at 890x zoom. This may be used to assess the range of intracellular gap radius to calculate a new value for r_p.

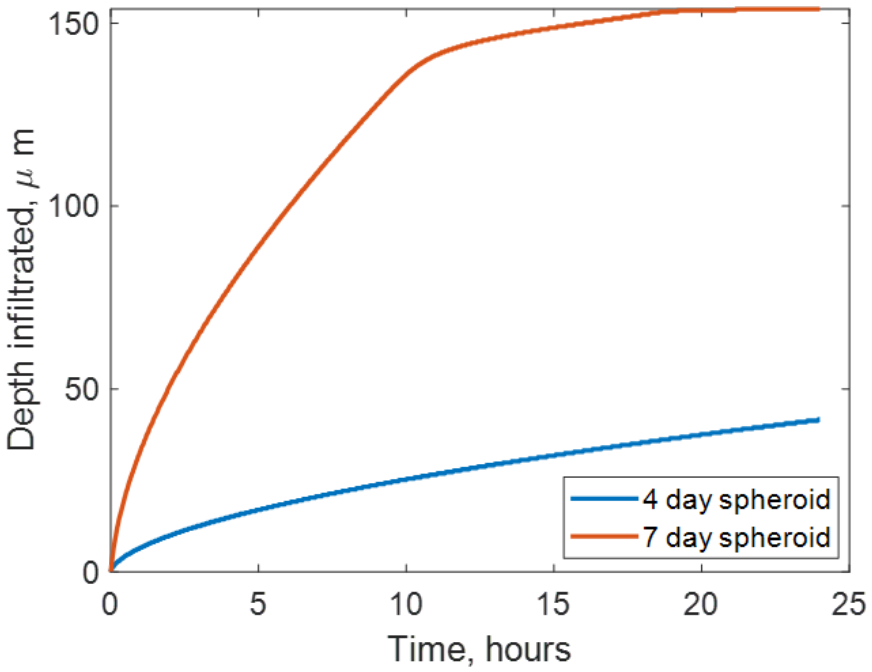

Figure 4.25: A comparison of the depth to which polymersomes permeate for pore sizes equivalent to 4 and 7 day spheroids.

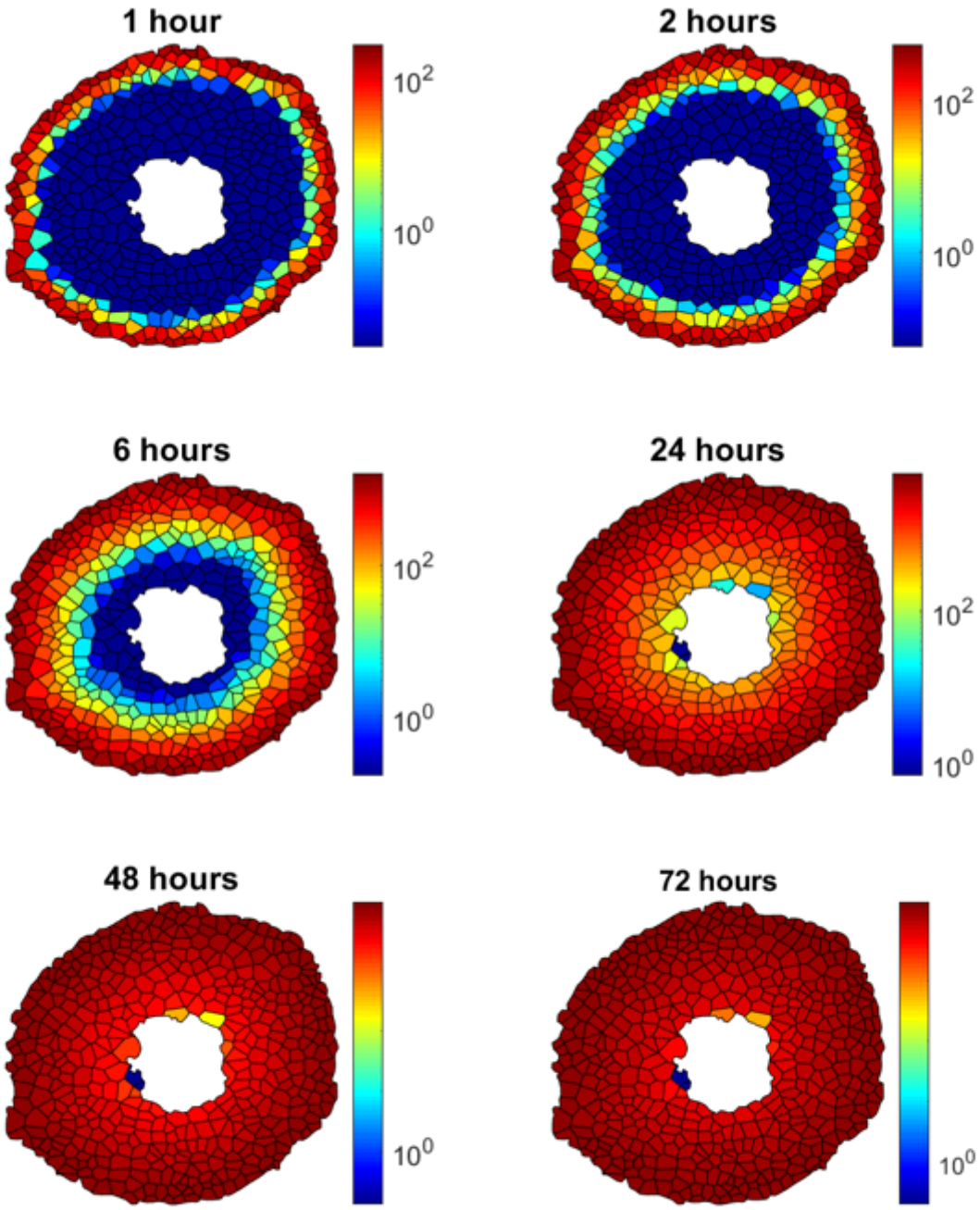

Figure 4.26: A prediction of the total number of internalised polymersomes for a spheroid with a r_p equivalent to that found in a 7 day spheroid. The geometry was generated using the Voronoi Tessalation in section 4.9.1. For each cell, the number of internalised polymersomes was predicted by calculating the distance from the cell nucleus to the outer boundary. Units for all images are polymersomes/cell.

4.11 Optimising the therapeutic dose delivery

Due to the diffusion coefficient being governed by the ratio of the radius of the polymersome and extracellular gap, it is clear that decreasing the polymersome radius will lead to a greater concentration within the spheroid. However, a decreased polymersome radius may also lead to a smaller volume of therapeutic agent being delivered. Therefore, there may exist an optimal polymersome radius to maximize the delivery of the therapeutic agent to different points within the spheroid. The volume of therapeutic agent per cell, V_{ther}, may be related to the number of internalised polymersomes per cell, B_{int} as calculated in Eq 4.57, and the radius of the polymersome, α, through the following relationship,

$$V_{ther} = B_{int}\frac{4\pi\alpha^3}{3}. \tag{4.60}$$

In order to quantify how the volume of therapeutic agent varies across the spheroid, we calculate the dose per cell delivered to 3 points: an outer point on the outer boundary; a mid point, in-between the inner and outer boundaries; and an inner point on the boundary of the necrotic core. We may sample across a range of polymersome radii in order to assess the optimal therapeutic dose.

Figure 4.27 shows the changes in therapeutic dose at the 3 points within the spheroid with differing polymersome radii. The point on the outer boundary is not affected by the reduced permeability, and therefore the optimal size is the greatest volume possible. However, for both the mid and inner points, we see a large decrease in the

volume delivered with large polymersome radius, due to the reduced permeability. In order to optimise the total number of cells containing polymersomes after 24 hours, you would therefore chose the optimal radii for the inner point, i.e. for total spheroid coverage. We are also able to generate a similar plot for a pore size equivalent to a 7 day spheroid, shown in Figure 4.28.

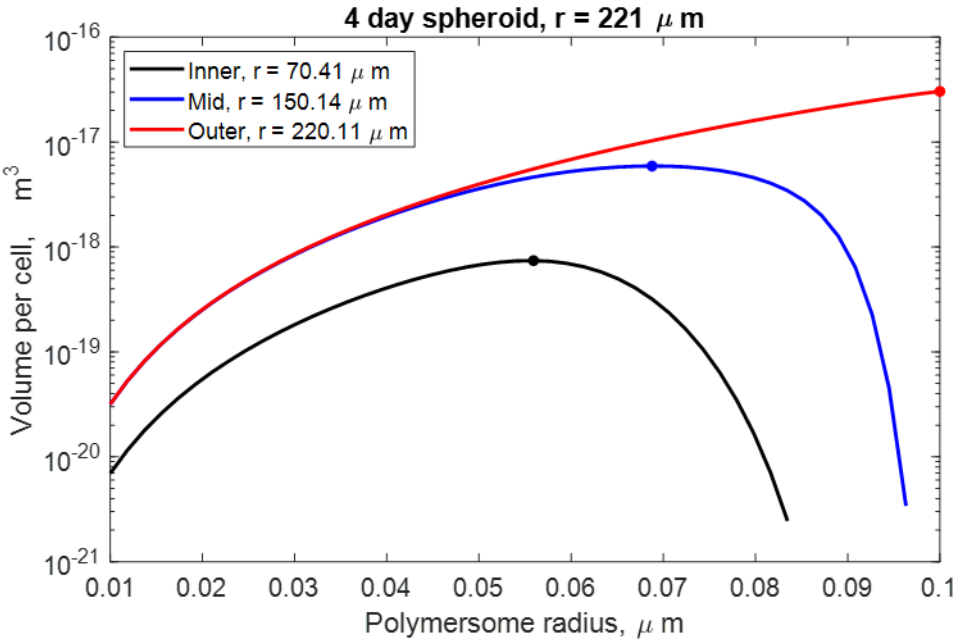

Figure 4.27: The total volume of therapeutic agent delivered to each cell at 3 different points within the spheroid after 24 hours. Optimal radii for each point are marked.

When comparing Figure 4.27 with Figure 4.28, we see an increase in permeation to the mid and inner points with large polymersomes, due to the increased pore size. This leads to a polymersome with a radius around 20% larger predicted to deliver the optimal dose to the inner points of the 7 day spheroid.

By varying both the pore size and radius of the polymersome, we are able to quantify how the optimal polymersome radius changes for each of the three points within the spheroid with respect to different pore sizes.

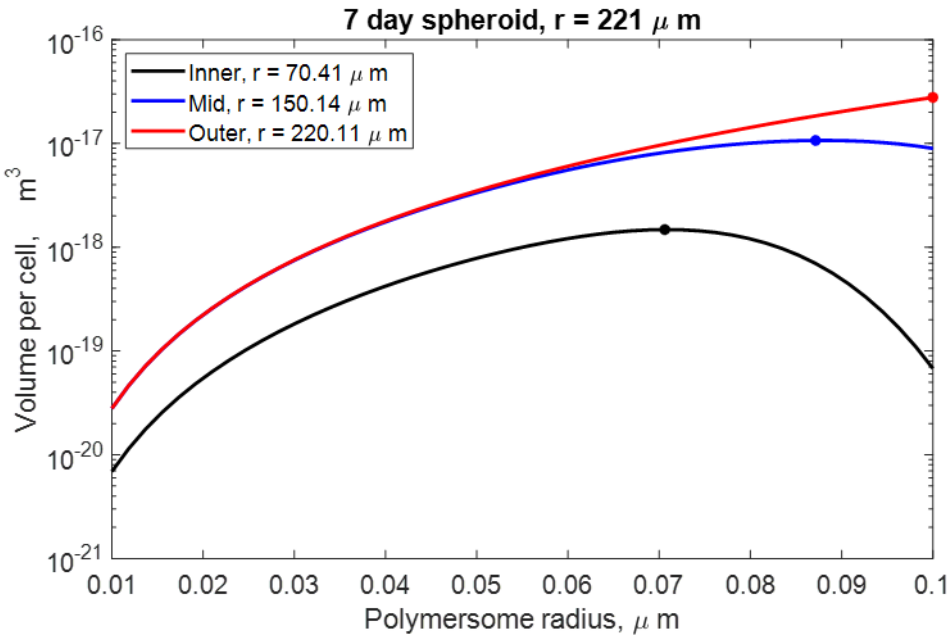

Figure 4.28: The total volume of therapeutic agent delivered to each cell at 3 different points within the spheroid with a pore size equivalent to a 7 day spheroid, after 24 hours. Optimal radii for each point are marked.

Figures 4.29, 4.30 and 4.31 show a series of pore sizes which represent a typical range found in spheroids older then 4 days. Unsurprisingly, as is found in Figures 4.27 and 4.28, the largest size polymersome will deliver the most therapeutic agent to cells on the outer boundary.

In Figure 4.30, we see similar behaviour to the outer point for largest two pore radii, however, for smaller radii, we see the need to reduce the polymersome radii in order to ensure that the optimal dose is delivered. Finally, in Figure 4.31, we see a similar bell shaped curve for smaller r_p values in the mid point. It is clear from this figure, the need to balance the volume of therapeutic agent, with the permeability reduction, that comes from a larger volume of polymersome.

Figure 4.32 shows the the optimal size polymersome for the total volume delivered to cells after 24 hours for the range of pore radii from $0.1076\,\mu$m to $0.1826\,\mu$m.

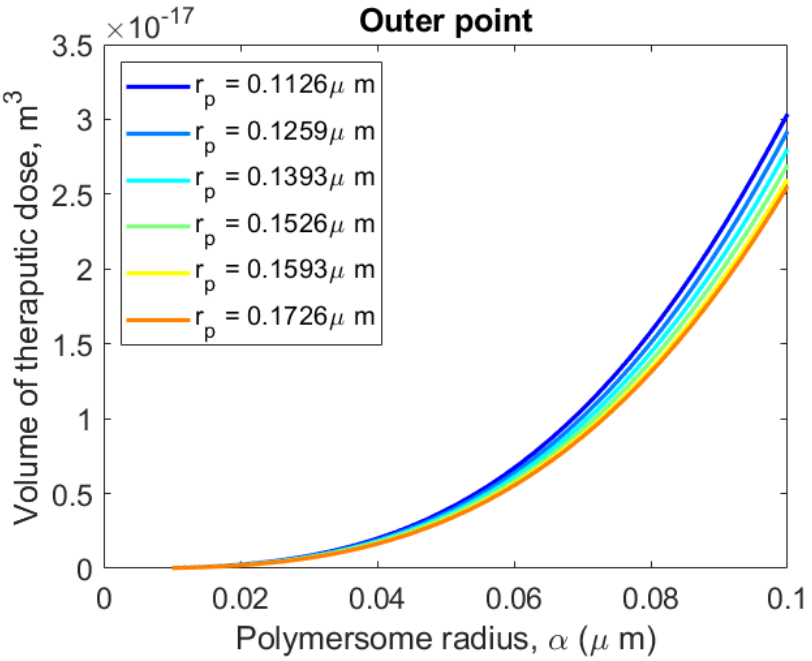

Figure 4.29: The total volume of therapeutic dose delivered to cells on the outer boundary of the spheroid, after 24 hours for varying polymersome and pore radii.

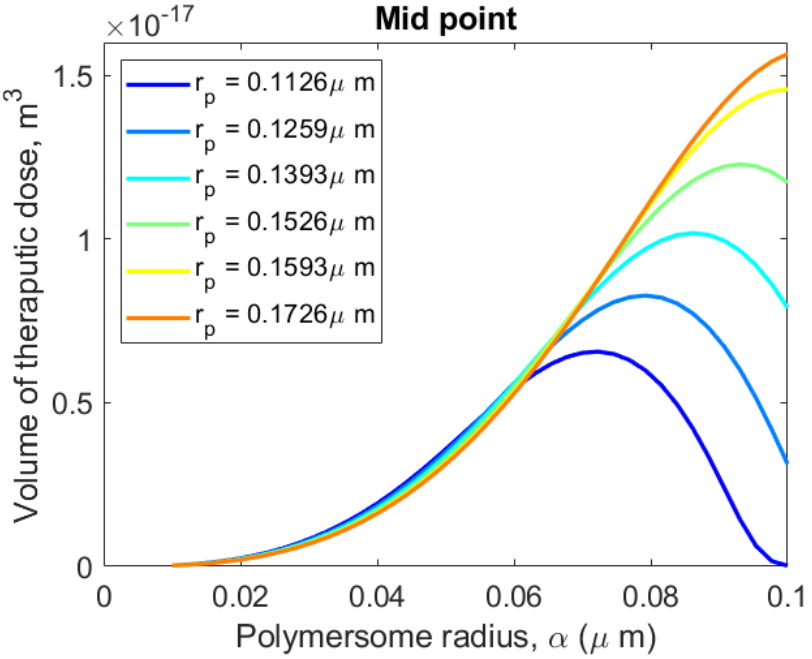

Figure 4.30: The total volume of therapeutic dose delivered to cells on the in the middle of the inner and outer boundaries of the spheroid, after 24 hours for varying polymersome and pore radii.

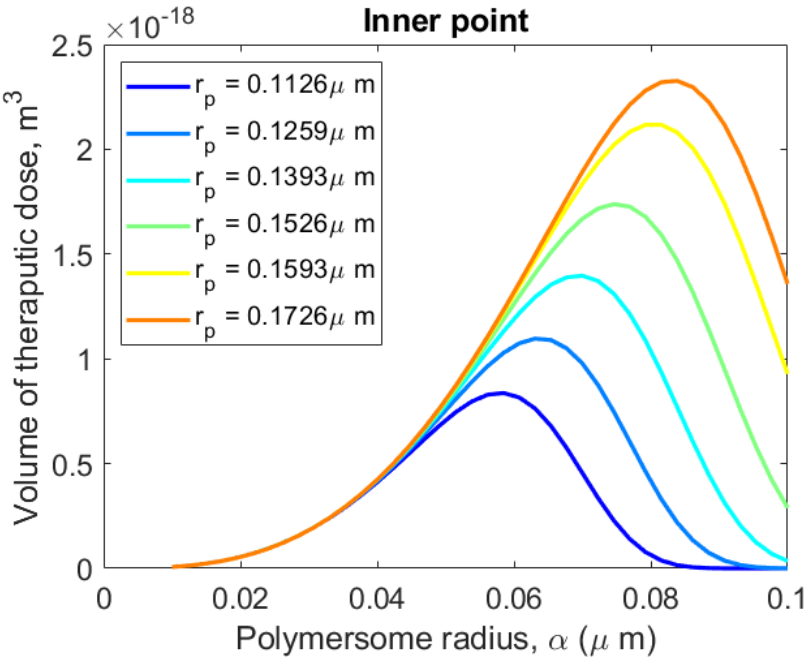

Figure 4.31: The total volume of therapeutic dose delivered to cells on the inner boundary of the spheroid, after 24 hours for varying polymersome and pore radii.

As observed previously, the optimal size for delivery to the outer points will be the largest possible polymersome. For both the mid and inner points, there is an almost linear relationship between the optimal size and pore radii, with the mid and outer points coinciding at around $r_p = 0.165\,\mu$m. This would suggest that permeation to the middle of the spheroid isn't restricted by the size of the polymersome at this point. However, the optimal size polymersome for the inner point doesn't reach this maximum size, suggesting permeation is still a limiting factor when trying to deliver the maximum amount of therapeutic agent deep within the spheroid. This suggests that for larger spheroids, the optimal size of polymersomes may be smaller, in order to increase the overall permeability. Similarly, for smaller sized spheroids, a larger size polymersome may be closer to the optimal size as the depth permeability is not limiting. In a more broad sense, it is therefore clear that delivering the optimal dose

is not only a function of the pore radius and polymersome radius, but also the depth to which the polymersome must penetrate.

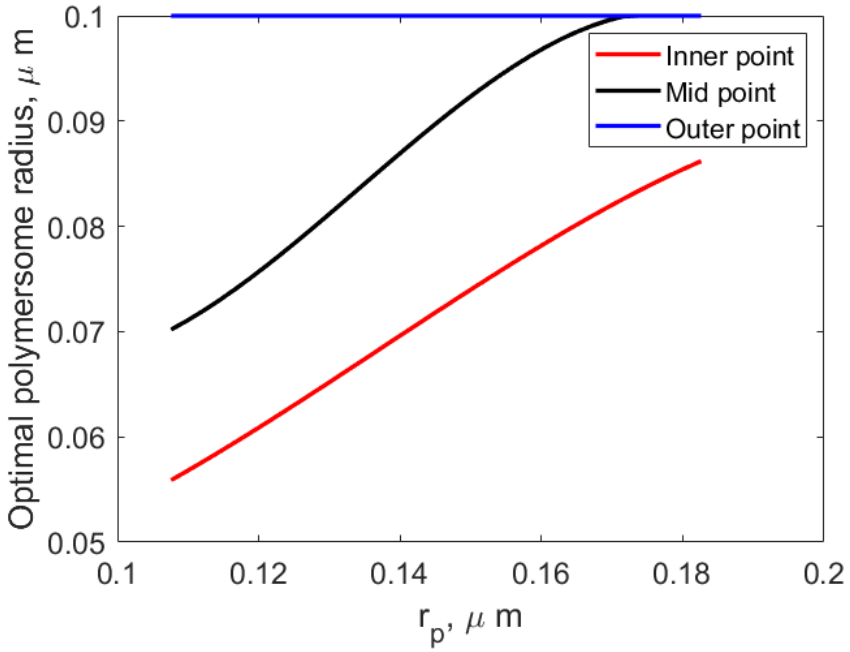

Figure 4.32: The optimal polymersome radius for maximizing the therapeutic dose delivered is shown for different radii of intracellular gaps, r_p, for three points in a 221μm spheroid after 24 hours.

4.12 Global sensitivity analysis

In order to gain a greater understanding of the model, we will explore parameter sensitivity. This will allow us to better understand the relationship between the binding parameters and uptake of the therapeutic agent, which in turn will lead to a increase in therapeutic efficacy. An encompassing approach to take when looking at parameter sensitivity, is global sensitivity analysis, as it allows the user to look at parameter sensitivity by perturbing parameters simultaneously.

During a global sensitivity analysis all parameters are varied simultaneously over predefined ranges which allows the user to evaluate the relative contributions of each individual parameter as well as the interaction between parameters. This is particularly valuable in modelling systems with orders of magnitude differences between model inputs as it allows one to determine from where and how changes will affect the system. A number of methods of Global sensitivity analysis exists, including; partial rank correlation coefficient [179], Fourier amplitude sensitivity analysis (FAST), eFAST [180] which is an extension of the FAST method, and Sobol's method [181]. FAST, eFAST and Sobol's methods are all variance based methods, with the main difference being the algorithm used to perform the multidimensional integration [182]. Variance based methods have been shown to be particularly useful in quantifying not only the effect of each parameter, but the effect of combinations the parameters.

Due to the increase in interaction terms, runtime for higher dimensional models grows exponentially [183], where for the total number of parameters, k, we may calculated $2^k - 1$ interaction terms. Fortunately, we can make use of the COSSAN tool set

(*www.cossan.co.uk*), developed at the University of Liverpools Institute for Risk and Uncertainty to perform our Global sensitivity analysis. COSSAN is an open-source tool set, designed with Matlab interface in order to quantify, mitigate and manage risk and uncertainty.

We begin by generating a probability distribution for each of the parameters we wish to perturb, around the means of the original parameter values. COSSAN then utilises Latin Hypercube Sampling (LHS) to generate N near-random parameter sets, where N is the total number of iterations. At each iteration, the model is solved with a given parameter set, and output is assessed against a predefined baseline output, which was generated using the mean value of each parameter. Parameter sensitivity is then calculated using Sobol's method in order to ascertain the effect of each parameter.

Before looking at the COSSAN output, we will look at the theory and method of generating Sobol indices, used to calculate our sensitivity measures.

4.12.1 Sobol's method

Say we have some function $Y = f(X)$ where our input parameters, $X = (x_1, x_2, ..., x^k)$, are mutually dependent and uniformly distributed on $[0, 1]$ after some rescaling. We have a mean f_0 written as,

$$f_0 = \int_{\mathbb{R}^k} X f(X) dX = \mathbf{E}[Y]. \tag{4.61}$$

We may write $f(X)$ in a decomposed form, known as its Hoeffding-Anova decomposition where we have the following,

$$f(X) = f_0 + \sum_{i=1}^{n} f_i(x_i) + \sum_{i<1}^{n} f_{ij}(x_i, x_j) + ... + f_{12...n}(x_1, x_2, ...x^n). \tag{4.62}$$

Where the factors of the decomposition are given as,

$$f_i = \mathbf{E}[Y \mid x_i] - \mathbf{E}[Y], \tag{4.63}$$

$$f_{ij} = \mathbf{E}[Y \mid x_i, x_j] - f_i - f_j - \mathbf{E}[Y]. \tag{4.64}$$

However, Sobol showed that we can only calculate each term as conditional expectations of the model if each term within the expansion has a 0 mean, as in Equation 4.65,

$$\int_0^1 f_{i_1...i_s}(x_{i_1}, ..., x_{i_s}) dX_k = 0 \quad \text{for } k = i_1, ..., i_s. \tag{4.65}$$

We can also calculate the variance V, given as,

$$V = \int_{\mathbb{R}^k} X^2 f(X) dX - f_0^2 = \mathbf{E}[Y^2] - \mathbf{E}[Y]^2. \tag{4.66}$$

If Equation 4.65 holds true, then squaring by both sides of Equation 4.62 and integrating over $\mathbb{R}^k$ leads to the following, where the decomposed terms are calculated in the same fashion as above:

$$V = \sum_{i=1}^{k} V_i + \sum_{i<j}^{k} V_{ij} + \sum_{i<j<l}^{k} V_{ijl} + ... + V_{1,2,...,k}, \tag{4.67}$$

which represents the total variance of the $f(x)$. In order to quantify each input parameter's contribution we calculate the Sobol indices, which is simply a normalized measure of the variances described in Equation 4.67, and represents all the combinations of sources for a parameters. To calculate, we must divide Equation 4.67 by the total variance, V, to get the following,

$$\sum_{i=1}^{k} S_i + \sum_{i<j}^{k} S_{ij} + \sum_{i<j<l}^{k} S_{ijl} + ... + S_{1,2,...,k} = 1. \tag{4.68}$$

From the above, we can calculate the so-called first order and total effect contributions. The first order contribution S_i quantifies the main effect of each parameter on the output variance. We can also calculate interaction effects, from the higher order terms of the decomposition. Factors are said to have interacted, when the sum of their first order terms is not equal to the total effect. The total effect term S_{Ti}, which is the total effect of a parameter x_i on the variation, given as the sum of first and all higher order terms. In practice, due to the exponential increase in the number of parameter combinations, $(2^k - 1)$, and therefore computational cost, it is common to instead estimate both the first order effects, S_i, and the total effects, S_{Ti} and. Saltelli et al. [184] provides a method that is utilised by COSSAN for estimating both terms.

4.13 Parameter sensitivity

4.13.1 Number of internalised polymersomes

With an understanding of the method which is utilised by COSSAN, we are able to perform a global sensitivity analysis on the spatially dependent model from section 4.8. The first output variable we will investigate is the total number of internalised polymersomes. This will provide information on what parameters have the greatest contribution to the binding and internalisation processes. In order to calculate the total number of internalised polymersomes at each time point, we integrate the number of internalised polymersomes, B_{in} over the volume of the spheroid, for each time point, given as,

$$B_{int}(t) = 4\pi \int_0^R r^2 B_{in}(r,t)\, dr. \tag{4.69}$$

This will generate a cumulative number of internalised polymersomes over time, for the entire volume of spheroid for a given parameter set.

Figure 4.33 shows the normalised first order, and total effect sensitivity measures for each of the parameters. We can see in Figure 4.33 that the parameter which has the largest change on the number of internalised polymersomes is the 3d binding rate k_{3a}. The 3d binding rate is the initial process that subsequent binding and internalisation relies upon. An increase in k_{3a}, leads to greater number of ligand-receptor complexes forming, therefore increasing the number available polymersomes to further bind or be internalised. Similarly, a decrease in k_{3a}, results in fewer ligand-receptor complexes forming, reducing then number of polymersomes available for internalisation.

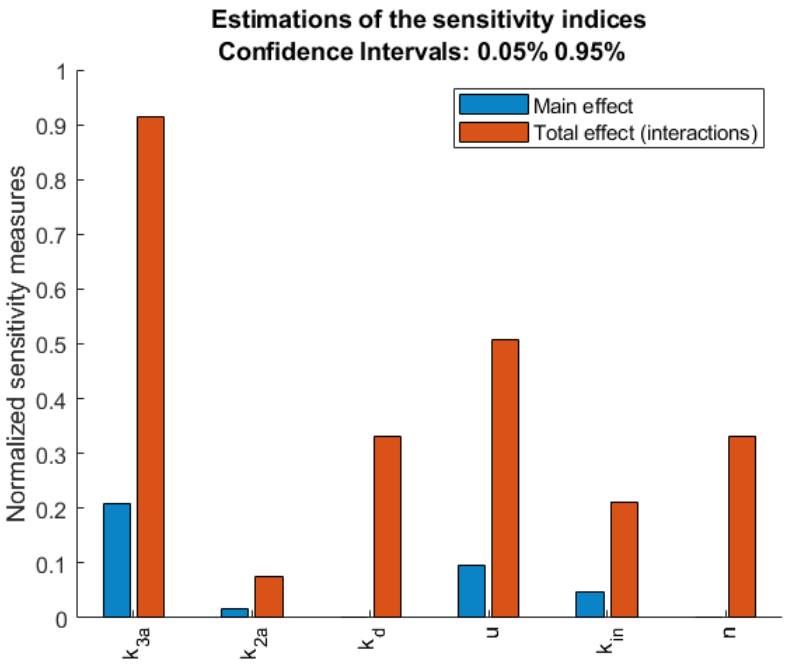

Figure 4.33: The global sensitivity output from COSSAN for total number of internalised polymersomes. The parameter that has the greatest effect on the total number of internalised polymersomes is the 3d binding rate, k_{3a}.

The second most important parameter is the receptor recycling rate, u. An increase in receptor recycling rate, leads to an increased number of surface receptors F_s, which in turn, increases the number of available initial binding sites. On the contrary, reduction in the receptor recycling rate decreases the number of available binding sites. Finally, an increase in internalisation rate k_{in}, will clearly increase the number of polymersomes internalised.

In order to quantify the effect of perturbing the above sensitive parameters, we will now perturb each parameter individually, between -90% and 300%, in order to see how it affects the total number of internalised polymersomes. Like with the global sensitivity analysis, the total number of internalised polymersomes will be calculated using Equation 4.69. However, for comparison, a single value of B_{int} will be taken

after 12 hours.

Figure 4.34 shows how individually perturbing k_{3a}, u and k_{in} affects the total number of internalised polymersomes. As shown in the global sensitivity analysis, k_{3a} is the most sensitive parameter, where a 100% rate increase would result in a 46% increase in the number of polymersomes internalised after 12 hours. Likewise, a 100% increase in the least sensitive of the 3 parameters, k_{in} would cause an 13.5% increase in the number of polymersomes internalised.

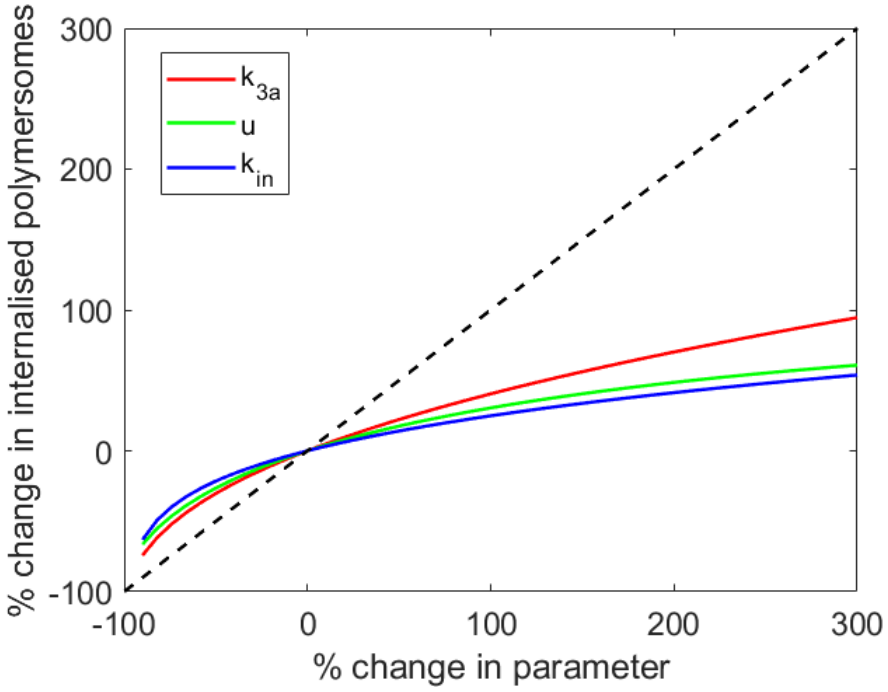

Figure 4.34: The 3 most sensitive parameters from the global sensitivity analysis are perturbed individually, between -90% and 300% of their original value. The cumulative number of internalised polymersomes after 12 hours is then normalised by the unperturbed value and plotted as a % change.

Due to the method of calculating the effective diffusion coefficient in section 4.7, another parameter which could effect the total number of internalised polymersomes

is the polymersome radius, α. The diffusion coefficient is calculated as a function of the ratio of polymersome radius to the pore radius r_p, and therefore, decreasing α, would result in an increased concentration of polymersomes within the spheroid. Like in Figure 4.34, we will perturb the radius of the polymersome to show how this effect the number of internalised polymersomes. However, α will only be perturbed between -80% and $+5\%$ of its original value, as the effective diffusion coefficient is equal to zero when $\alpha \geq r_p$.

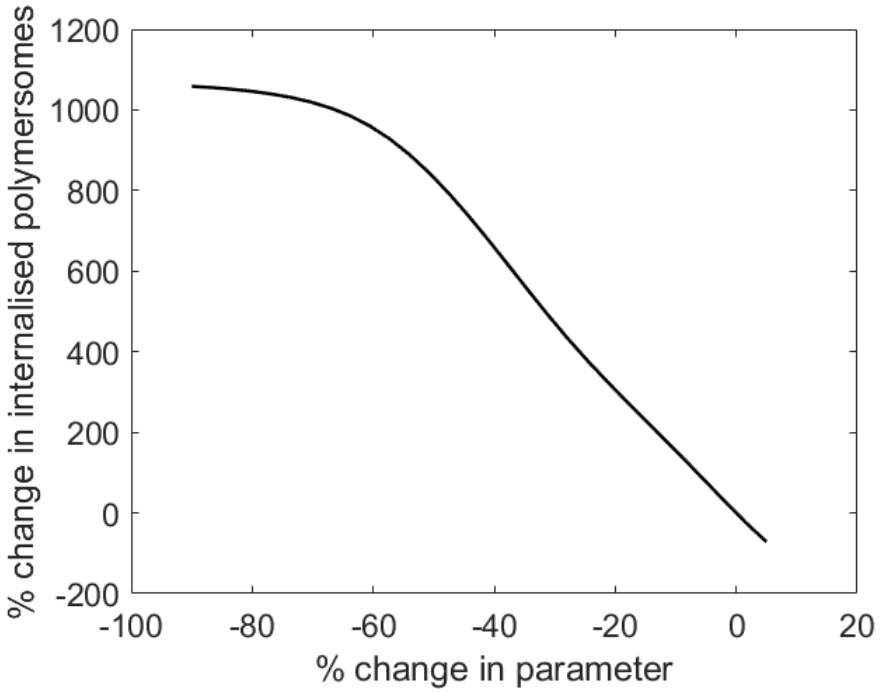

Figure 4.35: A decrease in the polymersome radius, a, increases the effective diffusion coefficient, and therefore increases the concentration of polymersomes within the spheroid. This leads to an increase number of complexes forming, and therefore an increase in the number of internalised polymersomes.

Figure 4.35 shows the relationship between polymersome radius, and the number of internalised polymersomes. Initially, decreasing the radius of the polymersome shows a linear increase in the number of internalised polymersomes, however, after a -60%

decrease, there is a far less significant change. To better understand, we look to Figure 4.36 and Figure 4.37, which show the distribution of unbound polymersomes with a 20% and 60% reduction in the the radius of the polymersome. In Figure 4.36, the concentration of unbound polymersomes is high near the spheroid boundary and negligible in the core. In comparison, Figure 4.37 the external and internal concentrations are equal in all points of the spheroid after 7 hours. At this point, initial binding will reach its maximum rate, subsequently maximising the number of internalised polymersomes.

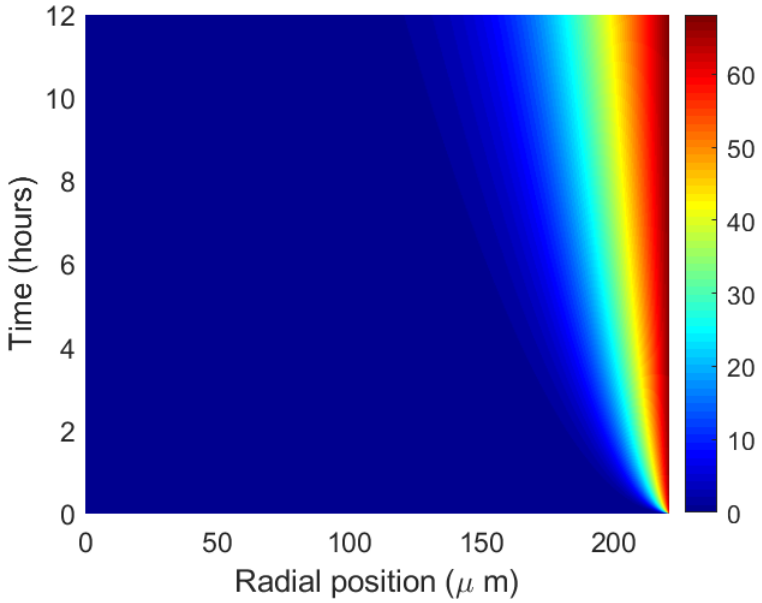

Figure 4.36: The distribution of unbound polymersomes, B_0, with a 20% decrease in the radius of the polymersomes. Units of the colour bar are polymersomes per μm^3.

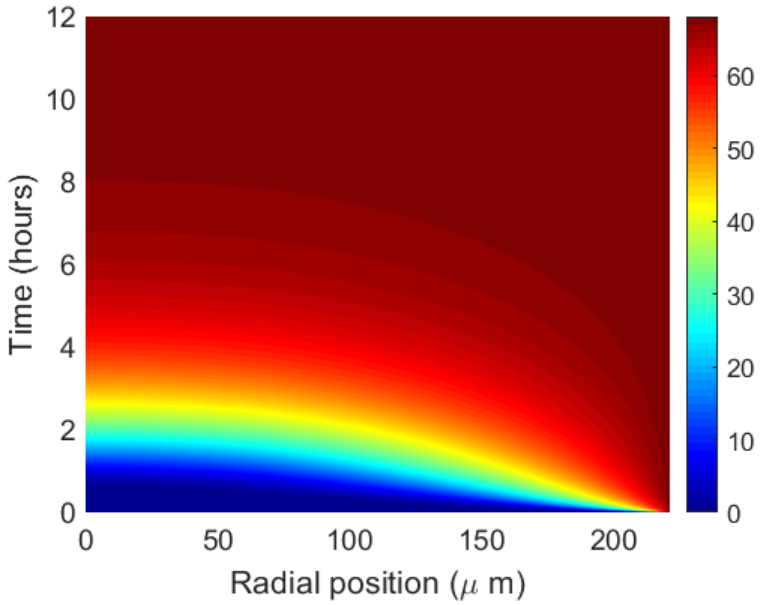

Figure 4.37: The distribution of unbound polymersomes, B_0, with a 60% decrease in the radius of the polymersomes. Once the polymersome radius has reduced by 60%, there in very little increase in the number of internalised polymersomes. Units of the colour bar are polymersomes per μm^3.

4.13.2 Cells containing polymersomes

Another metric we may perform a global sensitivity analysis on is the number of cells containing polymersomes. As in Section 4.9.2, we calculate the percentage of cells containing polymersomes, by calculating if the number of polymersomes per cell in an annulus is greater than a given threshold, where the threshold is given as 1.6327 polymersomes/cell. The percentage of cells containing polymersomes at time t is given as,

$$\%\, cells(t) = \frac{\sum_{j=1}^{q} h(j,t) M_c(j)}{4\pi \int_0^R r^2 M \, dr}, \tag{4.70}$$

where $h(j,t)$ is a binarising function defined as,

$$h(j,t) = \begin{cases} 0 & \text{if } P(j,t) < \text{threshold}, \\ 1 & \text{if } P(j,t) \geq \text{threshold}. \end{cases}$$

and $P(j,t)$ is the number of polymersomes per cell in a given annulus, j and the number of cells in a given annulus is defined to as follows,

$$M_c(x) = 4\pi \int_{r_j}^{r_{j+1}} r^2 m \, dr, \tag{4.71}$$

where m is the concentration of cells.

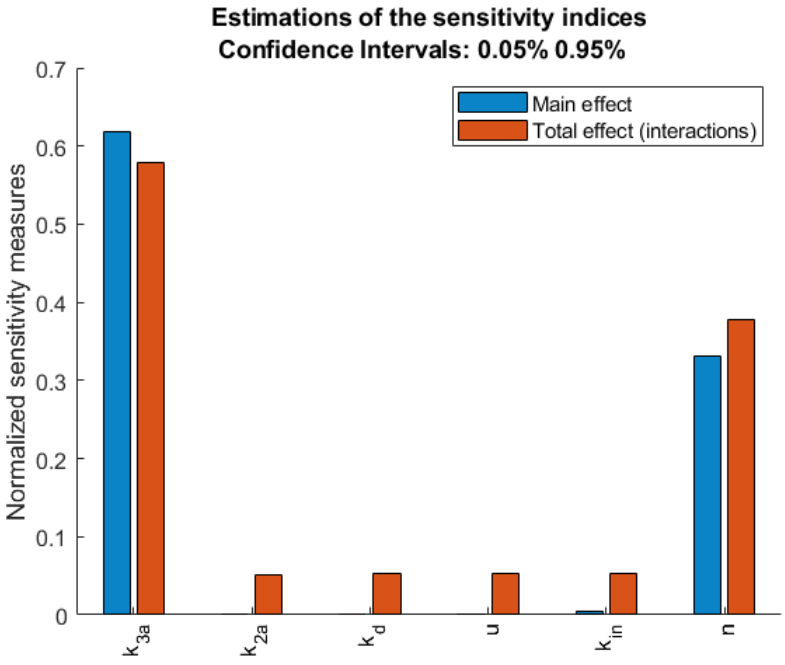

Figure 4.38: The Global sensitivity output from COSSAN for percentage of cells containing polymersomes after 12 hours. The parameter that has the greatest effect on the total number of internalised polymersomes is the 3d binding rate, k_{3a}.

Figure 4.38 shows the normalised first order, and total effect sensitivity measures

for each of the parameters. As with the total number of internalised polymersomes, the most sensitive parameter is the 3d binding rate, k_{3a}. In regions of low extracellular concentration of unbound polymersomes, a larger initial binding rate ensures receptor-ligand complexes more readily form. On the contrary, even in regions with high extracellular concentrations, if there is a low rate of initial binding then polymersomes cannot be internalised. The maximum number of bonds formed, n is also a sensitive parameter. If there a lower number of maximum bonds, there are less ligands to form the ligand-receptor complexes, resulting in less internalised polymersomes. Again, we can quantify how much changing the parameters effects the number of cells containing polymersomes, by perturbing their values individually and looking at the relative fold change.

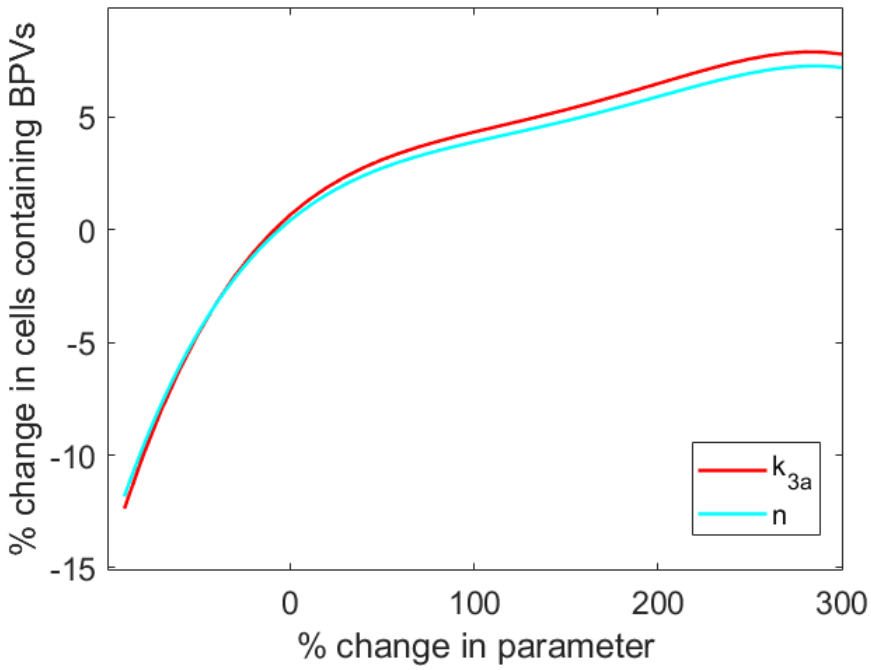

Figure 4.39: The global sensitivity output from COSSAN for percentage of cells containing polymersomes after 12 hours. The parameter that has the greatest effect on the total number of internalised polymersomes is the 3d binding rate, k_{3a}.

Figure 4.39 shows how perturbing k_{3a} and n relates the the relative fold change in cells containing polymersomes. A 95% reduction in k_{3a} leads to no cells containing polymersomes, while a 100% increase leads to a 18.5% increase in cells containing polymersomes. A 150% increase in the maximum number of only leads to an increase of 5% more cells containing polymersomes, while a 95% decrease leads to 20% less cells containing polymersomes.

A factor which affects the amount of cells containing polymersomes is the inability for the polymersome to permeate deeper into the spheroid. Figures 4.36 and 4.37 showed that decreasing the polymersome radius, increased the extracellular concentration, and the total number of internalised polymersomes. Figure 4.40 shows a similar relationship to Figure 4.35, where a reduction in particle radius leads to a large increase in the number of cells containing polymersomes. A reduction of 20% leads to 150% increase in the number of cells containing polymersomes, while a 40% decrease leads to nearly all cells containing polymersomes. We may therefore conclude that the limiting factor for the uptake of polymersomes to all cells within the spheroid is the ability for the polymersome to permeate, as long as the reduced radius does not have a large, detrimental effect on the 3d binding rate, or the maximum number of bonds.

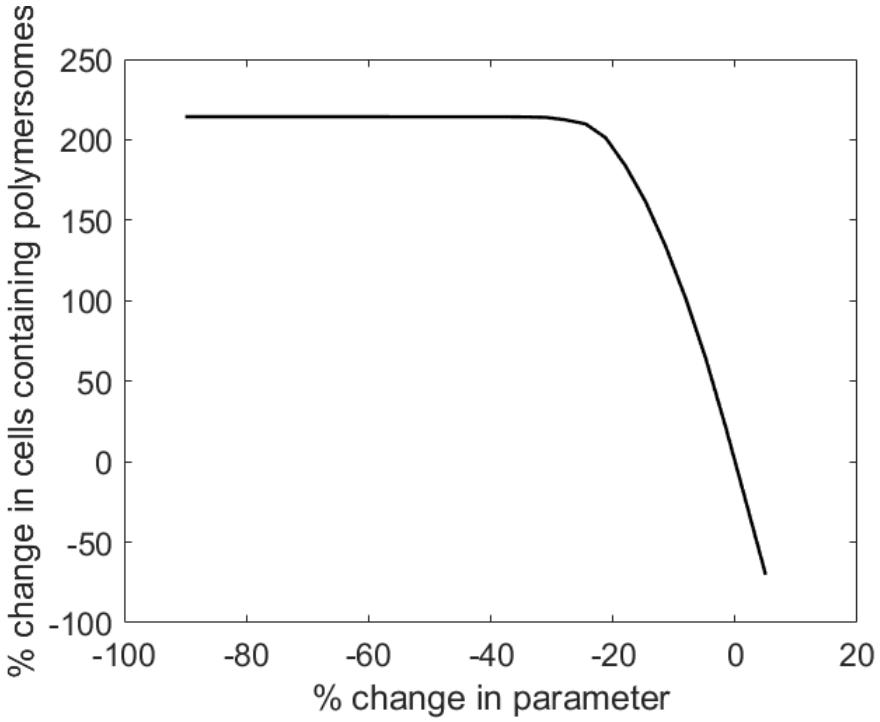

Figure 4.40: The relationship between polymersome radius and the number of cells containing polymersomes. A 40% decrease leads to nearly all cells containing polymersomes, due to their ability to permeate through the entire spheroid.

4.14 Chapter discussion

The use of polymersomes as a vehicle to deliver therapeutic agents to specific cells type is an exciting prospect in increasing payload delivery [47], and reduce off target toxicity [45], which leads to many of the side effects found with current treatments [150]. Modelling the uptake of these polymersomes was done in one of two ways: a complex binding model that was only dependent on time [63, 40]; or a simple binding model which is dependent on both space and time [64, 13, 47]. However, there are currently no models which combines the two. This is due to the computational power required to solve a large number of partial differential equations (PDEs), which makes model analysis slow.

In the first Sections of this chapter, we recreated a previously published model by Sorrell et al. [63], which was parametrised against monoculture experimental data. It was shown, that under the assumption of a constant internalisation rate, and $k_d B_1 \approx 1$, statistical moments could be used to create a simpler model with much of the model complexity removed. This reduced the model from 44 ODEs, to 8 ODEs, while retaining all relevant variables, such as unbound, bound and internalised polymersomes, and unbound and internalised surface receptors. Methods for defining the aggregation of a distribution were investigated. Both the variance-to-mean ratio, and coefficient of variation were described as possible metrics, however, due to the changing direction of aggregation, neither were suitable. Instead, a modified variance-to-mean ratio was suggested, which could describe both the degree and direction of aggregation, (i.e. aggregation to a higher number, or lower number of bonds). By utilising this metric alongside the mean and variance, we gained a greater understand as to what happens to the distribution across the parameter space. It was found that a reduction in the rate of internalisation, k_{in}, and an increase in the subsequent binding rate, k_{2a}, caused the greatest degree of aggregation. Defining this aggregation is key in aiding experimentalists modify the polymersome membrane properties, to optimise delivery.

Next, we applied this complex binding model to a spatial framework published by Goodman et al. [64]. The model by Goodman et al. described the diffusion of nanoparticles through the extracellular space of a spheroid. However, it only included simple rate equations for unbound, bound and internalised nanoparticles. This model incorporated a number of physiological parameters which affected the diffusivity of

these nanoparticles, such as the tortuosity and porosity terms. However, it was found that a number of the physiological parameters from the work didn't match previously reported ranges from within the literature. This is particularly important in modelling nanoparticles, as it has been shown by both Graff [13] and Ghaghaha [40], that the permeation was the rate limiting factor in uptake. It was therefore important to recalculate these physiological parameters based up on data and images provided to us by collaborators at the University of Sheffield. These were used to derive values for tortuosity, pore size, volume fraction of inter/extracellular space and a threshold intensity for the number of polymersomes per cell. In particular, we found a large discrepancy between our predicted values for both tortuosity and pore size, when compared to the values calculated by Goodman et al. [64]. Part of the differences may be attributed to the difference in methods used to calculate these parameters.

With a fully parametrised model for four day old spheroids, we were able to begin to understand how the different physiological and binding parameters affected permeation and uptake, which is key when trying to optimise delivery. Under the assumption that the only physiological change between 4 and 7 day old spheroids was the radius of extracellular gap, we could quantify the difference in permeation depth and total therapeutic dose delivery. As more recent methods to control the size of the nanoparticles are developed, such as work by Hicky et al. [185], we are explore the relationship between polymersome size and pore radius in order to maximise delivery of therapeutic agent. There is clear trade off, as reducing polymersome size in order to increase permeability, also decreases the volume of therapeutic agent. However, we were able to quantify the radius which optimises this trade off for a number three

different points within the spheroid. We believe this the first example of optimising delivery based on polymersome volume within the literature.

Finally, we wanted to understand how the various binding parameters affected both the number of cells containing polymersomes, and how many polymersomes these cells contained. We chose to utilise a global sensitivity analysis in order better understand the interactions between parameter in the system. One of the key points was how important the initial binding rate, or polymersome affinity is to the binding process. An increase affinity not only lead to an increase in polymersome uptake, but a small increase in the number of cells containing polymersomes. Experimentally, this will lead to a greater volume of the therapeutic agent delivered into cells, which in turn will lead to an increase in percentage of cell deaths. This may be attributed to an increased concentration gradient if there is more binding and uptake near the outer boundary of the spheroid.

Chapter 5

Discussion & Future Work

The development of multi-scale, mechanistic *in-silico* models are ever more important at all stages of the drug development process. In the early stages, models may be used in order to screen potential candidate molecules. In the latter stages, the *in-silico* models are constantly refined using data from both *in-vitro* and *in-vivo* experiments to better inform the development process. The methods used to model these processes generally fall into one of two categories: spatially dependent models, where movement is governed by a diffusion coefficient, solved using partial differential equations; and mass balance derived models where movement is generally governed by a first-order kinetic term solved with ordinary differential equations. This thesis outlines problems that are solved using both of these methods; in Chapters 2 and 4, where we are exploring heterogeneity on the micro-scale, space is far more important than when looking at organs as a whole as found in the PBPK model in Chapter 3. Chapter 2 describes the development of a novel numerical, continuous-discrete hybrid partial differential equation approach to predicting the permeation of xenobiotics

through the skin. The model's first novelty is the inclusion of histology derived geometries for both layer boundaries, and the discrete cells within the lower layer of the epidermis. One benefit of this approach over a brick and mortar style approach is the ability to account for the evolving shape of the keratinocytes as they perfuse from the basal layer up towards the stratum corneum, becoming flatter. This ensures the path taken by many lipophilic compounds which diffuse via intracellular lipid matrix will have a gradually reducing tortuosity as it permeates to the lower layers of the skin. This is particularly advantageous when modelling compounds which may be subject to change from the phase I and II enzymes present in the lower layers of the epidermis [89, 186], as it ensures metabolism is not overestimated.

Model parameters, such as layer-specific diffusion and partition coefficients are derived using a compound's physico-chemical properties as described in other publications using a finite element approach by both Kattou et al. [54], and Chen et al [55]. As found in these publications, many of the boundary conditions in the model from Chapter 2 assume a continuity of flux. However, our model differs on two boundaries; on the donor-phase/stratum-corneum boundary and with the discrete cells found in the lower layers of the epidermis. Due to the large concentration gradient found at early times, a continuity of flux boundary condition on the DP/SC boundary leads to quick saturation of the stratum corneum, rather than the slow saturation dynamics found *in-vitro*, which may in part be due to the presence of the protein filaggrin. It is, therefore more suitable to assign a saturation function to this boundary, where the maximum concentration may be estimated with knowledge of the compounds partition coefficient in the stratum corneum, and solubility in water. The additional

boundary condition to mimic the membrane for the discrete cells in the lower epidermis is also a novelty of this work. If instead, a continuity of flux boundary condition is assumed, a local steady-state between the extracellular and intracellular space is reached quickly, as movement between the two phases will be exclusively governed by the concentration gradient and ratio of partition coefficients. With the addition of the membrane, this movement between phases takes place over a larger time frame, more closely mimicking what is found *in-vivo*.

One of the great difficulties of modelling a compounds permeation of the skin is the large degree of variability in the data, even between similar experiments. There are a number of biological factors that may have contributed to these differences, which include the gender [187, 188], age [189] and ethnicity [190, 191] of the subject from which the skin sample is taken. As shown in Chapter 2, the model performs well at predicting the spatial distribution for compounds with lower initial concentrations but does not perform as well for larger starting concentrations. However, this is less of an issue as compounds delivered transdermally tend to be potent, with therapeutic doses below 20 mg IV dose/day [99].

In Chapter 3, the modifications necessary to alter a previously published PBPK model by Peters [104] to account for percutaneous absorption are described. While there are examples of PBPK models which account for percutaneous absorption [57, 59, 62], they have each been developed to model a single specific chemical, paired with a simple skin model, where uptake is modelled as a difference term rather than being governed by the permeability of the compound based on physico-chemical properties. This is important as it ensures that the uptake of small compounds with a lower

lipophilicity is not overestimated [126].

It was clear from the validation of this model against IV data, a K_p factor that modifies all partition coefficients by the same scaling ratio was necessary to ensure a good fit, with values varying between 2 and 50. This may be attributed to intrasubject variability [192], and errors in estimates for parameters such as the fraction unbound in plasma, and blood-plasma ratio. An alternate approach taken by Sawyer et al. [57] was to fit the diffusion coefficient, and permeation of dermal capillaries to instead fit *in-vivo* data. However, this method isn't viable for a finite-element approach due to the run time and still requires *in-vivo* data.

A key novelty from this chapter quantifies the effect on plasma concentration by altering both the thickness of the stratum corneum and the concentration in the patch modelled. We show that if the concentration within the patch is higher than the estimated maximum stratum corneum concentration, then increasing the concentration has little effect on increasing the plasma concentration. This chapter, also quantifies the negative impact a thicker stratum corneum has on the total quantity of drug which enters systemic circulation. This has been well understood for a number of years, but has never been quantified. This work has further highlighted the need for permeability enhancers such as micro-fabricated needles, to bypass the stratum corneum and delivering the therapeutic agent to lower layers of the epidermis, ensuring a more consistent dose is delivered to the patient. A better understanding of the whole process will only aid the development of more chemicals which can be delivered via the dermal route.

There have been numerous reports which have linked the lack of the protein filag-

grin found in patients with atopic dermatitis, to a reduction in epidermal barrier properties [137, 138]. However, very little time has been spent on understanding how this affects the uptake of compounds applied to the skin. We estimate that atopic dermatitis leads to a five-fold increase in the plasma concentration for skin from across the whole body, with this figure increasing linearly with an increase in vehicle concentration. This is an important finding for drug development and must be considered when designing the mode of delivery for highly potent chemicals, such as fentanyl. This also has an effect on the development of other compounds that humans are regularly exposed to, such as cosmetics and household cleaning products.

Chapter 4 describes the delivery and uptake of polymersomes as a vehicle for delivering anticancer therapeutics. The chapter describes the steps needed to modify a previously published complex binding model by Sorrell et al. [63], with a spatial model published by Goodman et al. [64]. Currently, modelling polymersome uptake is achieved in one of two ways: a complex binding model only dependent on time [40, 63]; or a simple binding model which is dependent on both space and time [13, 47, 64]. However, there currently is not a model that accounts for both, due to the computational cost of running large, partial differential equation models. The use of statistical moments for model closure is not novel technique, however is novel method when applied to this problem. It has previously been used, and is particularly useful in a system with many states, as it allows the system to still be described, with a reduced number of equations.

The model's physiological parameters were fitted to experimental data provided by collaborators at the University of Sheffield. There were large differences between our

estimated values for porosity, tortuosity, and pore size when compared to the values published by Goodman et al. [64]. However, these values do vary depending on cell type, age of spheroid, and method of measuring them. This fully parametrised model allowed us to study the key binding and physiological parameters which affect the total number of cells containing polymersomes, and the total number of internalised polymersomes.

One of the key results in this chapter is that there is an optimal polymersome size that maximises the delivery of the therapeutic agent. As discussed by both Graff et al. [13] and Ghaghaha et al. [40], permeation is the rate-limiting factor of uptake. However, as the volume of a polymersome scales cubically with radius, reducing this in order to increase permeation reduces the volume of the therapeutic agent delivered. Neither of these authors explores the range of optimal radii, in order to maximise delivery of the therapeutic agent. As permeation is a function of both the polymersome radius and the radius of on extracellular gaps, we have defined optimal size for delivery to different points within a spheroid. This is particularly useful, as more recent methods have been developed to control the size of polymersome produced [185].

As a complex binding model with spatial components has not yet been explored within the literature, the effect of the binding parameters on the uptake in a spatial context has not yet been quantified. We show using global sensitivity analysis that the key parameter which increased both the number of cells containing polymersomes and the total number of polymersomes was the initial binding affinity of the polymersome to the cell receptor. However, as permeation is still a key issue, altering

the binding affinity only had a small positive effect on the number of cells containing polymersomes.

While the results in this thesis are novel, and have interesting applications, with additional time and resources, model predictions and utility could be improved. With regards to the skin model and its application to PBPK in Chapters 2 and 3, the use of additional histology images would be useful in order to quantify any difference between *in-silico* calculations. While we believe there would be very little difference in results, it would allow us to put more trust in our results. Additionally, exploring histology images of skin from different regions of the body may also be interesting.

Any anti-cancer therapy which leads to a greater volume of therapeutic agent delivered to target cells while reducing off-target toxicity has great future potential. In order to further validate the physiological parameters estimated in Chapter 4, mimicking the process with additional histology images to assess differences in estimated values would be worth investigating. Additionally, this may be investigated with different cell lines, to assess whether the binding dynamics and optimal physiological parameters vary.

Bibliography

[1] Scott W Robinson, Marco Fernandes, and Holger Husi. Current advances in systems and integrative biology. *Computational and structural biotechnology journal*, 11(18):35–46, 2014.

[2] Thomas J Snowden, Piet H van der Graaf, and Marcus J Tindall. Model reduction in mathematical pharmacology. *Journal of pharmacokinetics and pharmacodynamics*, 45(4):537–555, 2018.

[3] Gerald T Ankley, Richard S Bennett, Russell J Erickson, Dale J Hoff, Michael W Hornung, Rodney D Johnson, David R Mount, John W Nichols, Christine L Russom, Patricia K Schmieder, et al. Adverse outcome pathways: a conceptual framework to support ecotoxicology research and risk assessment. *Environmental Toxicology and Chemistry: An International Journal*, 29(3): 730–741, 2010.

[4] Office of National Statistics. Oecd, . URL `https://www.https://aopwiki.org/`. (accessed: 28.04.2020).

[5] National Research Council, Committee on Acute Exposure Guideline Levels,

et al. Pbpk modeling white paper: Addressing the use of pbpk models to support derivation of acute exposure guideline levels. In *Acute Exposure Guideline Levels for Selected Airborne Chemicals: Volume 9*. National Academies Press (US), 2010.

[6] Jean Philibert. One and a half century of diffusion: Fick, einstein, before and beyond. *Diffusion Fundamentals*, 2(1):1–10, 2005.

[7] John Crank. *The mathematics of diffusion*. Oxford university press, 1979.

[8] George Gabriel Stokes et al. *On the effect of the internal friction of fluids on the motion of pendulums*, volume 9. Pitt Press Cambridge, 1851.

[9] Albert Einstein. Über die von der molekularkinetischen theorie der wärme geforderte bewegung von in ruhenden flüssigkeiten suspendierten teilchen. *Annalen der physik*, 322(8):549–560, 1905.

[10] William Sutherland. Lxxv. a dynamical theory of diffusion for non-electrolytes and the molecular mass of albumin. *The London, Edinburgh, and Dublin Philosophical Magazine and Journal of Science*, 9(54):781–785, 1905.

[11] Rep Kubo. The fluctuation-dissipation theorem. *Reports on progress in physics*, 29(1):255, 1966.

[12] Alexander N Gorban, Hrachya P Sargsyan, and Hafiz A Wahab. Quasichemical models of multicomponent nonlinear diffusion. *Mathematical Modelling of Natural Phenomena*, 6(5):184–262, 2011.

[13] Christilyn P Graff and K Dane Wittrup. Theoretical analysis of antibody targeting of tumor spheroids: importance of dosage for penetration, and affinity for retention. *Cancer research*, 63(6):1288–1296, 2003.

[14] KE Thompson and HM Byrne. Modelling the internalization of labelled cells in tumour spheroids. *Bulletin of mathematical biology*, 61(4):601–623, 1999.

[15] Yue Gao, Mingguang Li, Bin Chen, Zancong Shen, Peng Guo, M Guillaume Wientjes, and Jessie L-S Au. Predictive models of diffusive nanoparticle transport in 3-dimensional tumor cell spheroids. *The AAPS journal*, 15(3):816–831, 2013.

[16] Joseph Leedale, Anne Herrmann, James Bagnall, Andreas Fercher, Dmitri Papkovsky, Violaine Sée, and Rachel N Bearon. Modeling the dynamics of hypoxia inducible factor-1α (hif-1α) within single cells and 3d cell culture systems. *Mathematical biosciences*, 258:33–43, 2014.

[17] Cyril P Brayn and Grafton E Smith. The papyrus ebers, translated from the german version. *Letchworth, Herts: The Guardian City Press LTD*, 1930.

[18] Richard Rudgley. *The alchemy of culture: intoxicants in society*. British Museum Press, 1993.

[19] Stephen Rothman. The principles of percutaneous absorption. *The Journal of Laboratory and Clinical Medicine*, 28(11):1305–1321, 1943.

[20] Takeru Higuchi. Physical chemical analysis of percutaneous absorption process from creams and ointments. *J. Soc. Cosmet. Chem*, 11:85–97, 1960.

[21] Takeru Higuchi. Rate of release of medicaments from ointment bases containing drugs in suspension. *Journal of pharmaceutical sciences*, 50(10):874–875, 1961.

[22] JW Hadgraft and GF Somers. Percutaneous absorption. *Journal of Pharmacy and Pharmacology*, 8(1):625–634, 1956.

[23] Irvin H Blank. Cutaneous barriers. *Journal of investigative dermatology*, 45(4): 249–256, 1965.

[24] Irvin H Blank, Robert J Scheuplein, and Dorothy J MacFarlane. Mechanism of percutaneous absorption. 3. the effect of temperature on the transport of non-electrolytes across the skin. *The Journal of investigative dermatology*, 49 (6):582–589, 1967.

[25] Robert J Scheuplein, Irvin H Blank, GJ Brauner, and Dorothy J Macfarlane. Percutaneous absorption of steroids. *Journal of Investigative Dermatology*, 52 (1):63–70, 1969.

[26] Robert J Scheuplein and Irvin H Blank. Permeability of the skin. *Physiological reviews*, 51(4):702–747, 1971.

[27] Samir Mitragotri, Yuri G Anissimov, Annette L Bunge, H Frederick Frasch, Richard H Guy, Jonathan Hadgraft, Gerald B Kasting, Majella E Lane, and Michael S Roberts. Mathematical models of skin permeability: an overview. *International journal of pharmaceutics*, 418(1):115–129, 2011.

[28] Kelly D Mccarley and Annette L Bunge. Pharmacokinetic models of dermal absorption. *Journal of Pharmaceutical Sciences*, 90(11):1699–1719, 2001.

[29] Michael Davies, Ruth U Pendlington, Leanne Page, Clive S Roper, David J Sanders, Clare Bourner, Camilla K Pease, and Cameron MacKay. Determining epidermal disposition kinetics for use in an integrated nonanimal approach to skin sensitization risk assessment. *Toxicological Sciences*, 119(2):308–318, 2010.

[30] Kelly D Mccarley and Annette L Bunge. Physiologically relevant one-compartment pharmacokinetic models for skin. 1. development of models. *Journal of pharmaceutical sciences*, 87(4):470–481, 1998.

[31] Kelly D McCarley and Annette L Bunge. Physiologically relevant two-compartment pharmacokinetic models for skin. *Journal of pharmaceutical sciences*, 89(9):1212–1235, 2000.

[32] Micaela B Reddy, Kelly D Mccarley, and Annette L Bunge. Physiologically relevant one-compartment pharmacokinetic models for skin. 2. comparison of models when combined with a systemic pharmacokinetic model. *Journal of pharmaceutical sciences*, 87(4):482–490, 1998.

[33] B Mochnacki and A Piasecka-Belkhayat. Numerical modeling of skin tissue heating using the interval finite difference method. *MCB: Molecular & Cellular Biomechanics*, 10(3):233–244, 2013.

[34] Randall J LeVeque et al. *Finite volume methods for hyperbolic problems*, volume 31. Cambridge university press, 2002.

[35] Arne Naegel, Steffi Hansen, Dirk Neumann, Claus-Michael Lehr, Ulrich F Schaefer, Gabriel Wittum, and Michael Heisig. In-silico model of skin pene-

tration based on experimentally determined input parameters. part ii: Mathematical modelling of in-vitro diffusion experiments. identification of critical input parameters. *European journal of pharmaceutics and biopharmaceutics*, 68(2):368–379, 2008.

[36] Steffi Hansen, Andreas Henning, Arne Naegel, Michael Heisig, Gabriel Wittum, Dirk Neumann, Karl-Heinz Kostka, Jarmila Zbytovska, Claus-Michael Lehr, and Ulrich F Schaefer. In-silico model of skin penetration based on experimentally determined input parameters. part i: Experimental determination of partition and diffusion coefficients. *European Journal of Pharmaceutics and Biopharmaceutics*, 68(2):352–367, 2008.

[37] H Frederick Frasch. A random walk model of skin permeation. *Risk Analysis*, 22(2):265–276, 2002.

[38] MunJu Kim, Robert J Gillies, and Katarzyna Anna Rejniak. Current advances in mathematical modeling of anti-cancer drug penetration into tumor tissues. *Frontiers in oncology*, 3:278, 2013.

[39] Hak Soo Choi, Wenhao Liu, Fangbing Liu, Khaled Nasr, Preeti Misra, Moungi G Bawendi, and John V Frangioni. Design considerations for tumour-targeted nanoparticles. *Nature nanotechnology*, 5(1):42, 2010.

[40] Ketan B Ghaghada, Justin Saul, Jayaganesh V Natarajan, Ravi V Bellamkonda, and Ananth V Annapragada. Folate targeting of drug carriers: a mathematical model. *Journal of controlled release*, 104(1):113–128, 2005.

[41] James W Baish, Triantafyllos Stylianopoulos, Ryan M Lanning, Walid S Kamoun, Dai Fukumura, Lance L Munn, and Rakesh K Jain. Scaling rules for diffusive drug delivery in tumor and normal tissues. *Proceedings of the National Academy of Sciences*, 108(5):1799–1803, 2011.

[42] Triantafyllos Stylianopoulos, Konstantinos Soteriou, Dai Fukumura, and Rakesh K Jain. Cationic nanoparticles have superior transvascular flux into solid tumors: insights from a mathematical model. *Annals of biomedical engineering*, 41(1):68–77, 2013.

[43] Anne L Van De Ven, Min Wu, John Lowengrub, Steven R McDougall, Mark AJ Chaplain, Vittorio Cristini, Mauro Ferrari, and Hermann B Frieboes. Integrated intravital microscopy and mathematical modeling to optimize nanotherapeutics delivery to tumors. *AIP advances*, 2(1):011208, 2012.

[44] Steven R McDougall, Alexander RA Anderson, and Mark AJ Chaplain. Mathematical modelling of dynamic adaptive tumour-induced angiogenesis: clinical implications and therapeutic targeting strategies. *Journal of theoretical biology*, 241(3):564–589, 2006.

[45] Hermann B Frieboes, Min Wu, John Lowengrub, Paolo Decuzzi, and Vittorio Cristini. A computational model for predicting nanoparticle accumulation in tumor vasculature. *PloS one*, 8(2):e56876, 2013.

[46] Hamidreza Namazi, Vladimir V Kulish, Albert Wong, and Sina Nazeri. Math-

ematical based calculation of drug penetration depth in solid tumors. *BioMed research international*, 2016, 2016.

[47] Zhihui Wang, Romica Kerketta, Yao-Li Chuang, Prashant Dogra, Joseph D Butner, Terisse A Brocato, Armin Day, Rong Xu, Haifa Shen, Eman Simbawa, et al. Theory and experimental validation of a spatio-temporal model of chemotherapy transport to enhance tumor cell kill. *PLoS computational biology*, 12(6):e1004969, 2016.

[48] Edoardo Scarpa, Joanne L Bailey, Agnieszka A Janeczek, Patrick S Stumpf, Alexander H Johnston, Richard OC Oreffo, Yin L Woo, Ying C Cheong, Nicholas D Evans, and Tracey A Newman. Quantification of intracellular payload release from polymersome nanoparticles. *Scientific reports*, 6:29460, 2016.

[49] John P Sinek, Sandeep Sanga, Xiaoming Zheng, Hermann B Frieboes, Mauro Ferrari, and Vittorio Cristini. Predicting drug pharmacokinetics and effect in vascularized tumors using computer simulation. *Journal of mathematical biology*, 58(4-5):485, 2009.

[50] X Zheng, SM Wise, and V Cristini. Nonlinear simulation of tumor necrosis, neo-vascularization and tissue invasion via an adaptive finite-element/level-set method. *Bulletin of mathematical biology*, 67(2):211, 2005.

[51] Tsuo-Feng Wang, Gerald B Kasting, and Johannes M Nitsche. A multiphase microscopic diffusion model for stratum corneum permeability. i. formulation,

solution, and illustrative results for representative compounds. *Journal of pharmaceutical sciences*, 95(3):620–648, 2006.

[52] Tsuo-Feng Wang, Gerald B Kasting, and Johannes M Nitsche. A multiphase microscopic diffusion model for stratum corneum permeability. ii. estimation of physicochemical parameters, and application to a large permeability database. *Journal of pharmaceutical sciences*, 96(11):3024–3051, 2007.

[53] Johannes M Nitsche and Gerald B Kasting. A microscopic multiphase diffusion model of viable epidermis permeability. *Biophysical journal*, 104(10):2307–2320, 2013.

[54] Panayiotis Kattou, Guoping Lian, Stephen Glavin, Ian Sorrell, and Tao Chen. Development of a two-dimensional model for predicting transdermal permeation with the follicular pathway: demonstration with a caffeine study. *Pharmaceutical research*, 34(10):2036–2048, 2017.

[55] Longjian Chen, Lujia Han, Ouarda Saib, and Guoping Lian. In silico prediction of percutaneous absorption and disposition kinetics of chemicals. *Pharmaceutical research*, 32(5):1779–1793, 2015.

[56] Aileen Sandilands, Calum Sutherland, Alan D Irvine, and WH Irwin McLean. Filaggrin in the frontline: role in skin barrier function and disease. *Journal of cell science*, 122(9):1285–1294, 2009.

[57] Megan E Sawyer, Marina V Evans, Charles A Wilson, Lauren J Beesley, Lider S Leon, Chris R Eklund, Edward L Croom, and Rex A Pegram. Development

of a human physiologically based pharmacokinetic (pbpk) model for dermal permeability for lindane. *Toxicology letters*, 245:106–109, 2016.

[58] James B Knaak, Curt C Dary, Fred Power, Carol B Thompson, and Jerry N Blancato. Physicochemical and biological data for the development of predictive organophosphorus pesticide qsars and pbpk/pd models for human risk assessment. *Critical reviews in toxicology*, 34(2):143–207, 2004.

[59] Torka S Poet, Betsy D Carlton, James A Deyo, and Paul M Hinderliter. Hydroquinone pbpk model refinement and application to dermal exposure. *Food and chemical toxicology*, 48(11):3085–3092, 2010.

[60] HY Chang, WC Chia, JS Chou, and TS Shih. Using a physiologically-based pharmacokinetic (pbpk) model to estimate the contribution of skin absorption resulting from exposure to 2-methoxy ethanol (me) vapor in the occupational environment. *ARBETE OCH HALSA VETENSKAPLIG SKRIFTSERIE*, 10: 116–118, 2001.

[61] Ananya Roy, Clifford Weisel, and Panos Georgopoulos. A distributed parameter physiologically-based pharmacokinetic model for dermal and inhalation exposure to volatile organic compounds. *Risk analysis*, 16(2):147–160, 1996.

[62] Samee Maharjan, Roshan Sharma, Trine Husøy, Hubert Dirven, Monica Andreassen, and Bernt Lie. Modeling and simulation of triclosan kinetics and distribution in humans using a pbpk model. 2015.

[63] Ian Sorrell, Rebecca J Shipley, Vanessa Hearnden, Helen E Colley, Martin H

Thornhill, Craig Murdoch, and Steven D Webb. Combined mathematical modelling and experimentation to predict polymersome uptake by oral cancer cells. *Nanomedicine: Nanotechnology, Biology and Medicine*, 10(2):339–348, 2014.

[64] Thomas T Goodman, Jingyang Chen, Konstantin Matveev, and Suzie H Pun. Spatio-temporal modeling of nanoparticle delivery to multicellular tumor spheroids. *Biotechnology and bioengineering*, 101(2):388–399, 2008.

[65] Barry Markman and Jr FE Barton. Anatomy of the subcutaneous tissue of the trunk and lower extremity. *Plastic and reconstructive surgery*, 80(2):248–254, 1987.

[66] Gerard J Tortora and Bryan Derrickson. *Principles of anatomy and physiology*. John Wiley and Sons, 14th edition, 2014.

[67] Roland Moll, Ingrid Moll, and Werner W Franke. Identification of merkel cells in human skin by specific cytokeratin antibodies:: Changes of cell density and distribution in fetal and adult plantar epidermis. *Differentiation*, 28(2):136–154, 1984.

[68] Ehrhardt Proksch, Johanna M Brandner, and Jens-Michael Jensen. The skin: an indispensable barrier. *Experimental dermatology*, 17(12):1063–1072, 2008.

[69] Mark R Prausnitz and Robert Langer. Transdermal drug delivery. *Nature biotechnology*, 26(11):1261, 2008.

[70] Jens M Baron, Daniela HoÈller, Ruth Schiffer, Silke Frankenberg, Mark Neis, Hans F Merk, and Frank K Jugert. Expression of multiple cytochrome p450

enzymes and multidrug resistance-associated transport proteins in human skin keratinocytes. *Journal of Investigative Dermatology*, 116(4):541–548, 2001.

[71] Lilian G Yengi, Qian Xiang, Jinmei Pan, JoAnn Scatina, John Kao, Simon E Ball, Richard Fruncillo, Geraldine Ferron, and C Roland Wolf. Quantitation of cytochrome p450 mrna levels in human skin. *Analytical biochemistry*, 316(1): 103–110, 2003.

[72] Werner H Braun and John M Waechter Jr. Sources of uncertainty in pharmacokinetic prediction. *Journal of animal science*, 56(1):235–243, 1983.

[73] H Rothe, R Cubberley, H Duplan, J Einstein, S Gregoire, C Jacques Jamin, M Klaric, N Hewitt, and A Schepky. Cosmetics europe skin bioavailability and metabolism project. *Toxicology Letters*, (258):S62, 2016.

[74] Lisa M Russell and Richard H Guy. Measurement and prediction of the rate and extent of drug delivery into and through the skin. *Expert opinion on drug delivery*, 6(4):355–369, 2009.

[75] Multiphysics cyclopedia. URL `https://uk.comsol.com/multiphysics/finite-element-method`.

[76] Kosmas Kretsos, Matthew A Miller, Grettel Zamora-Estrada, and Gerald B Kasting. Partitioning, diffusivity and clearance of skin permeants in mammalian dermis. *International journal of pharmaceutics*, 346(1-2):64–79, 2008.

[77] Russell O Potts and Richard H Guy. Predicting skin permeability. *Pharmaceutical research*, 9(5):663–669, 1992.

[78] Mark E Johnson, Daniel Blankschtein, and Robert Langer. Evaluation of solute permeation through the stratum corneum: lateral bilayer diffusion as the primary transport mechanism. *Journal of pharmaceutical sciences*, 86(10):1162–1172, 1997.

[79] Samir Mitragotri. A theoretical analysis of permeation of small hydrophobic solutes across the stratum corneum based on scaled particle theory. *Journal of pharmaceutical sciences*, 91(3):744–752, 2002.

[80] Frank H Stillinger, Pablo G Debenedetti, and Swaroop Chatterjee. Scaled particle theory for hard sphere pairs. i. mathematical structure. *The Journal of chemical physics*, 125(20):204504, 2006.

[81] Hiromi Yasuda, CE Lamaze, and Anton Peterlin. Diffusive and hydraulic permeabilities of water in water-swollen polymer membranes. *Journal of Polymer Science Part A-2: Polymer Physics*, 9(6):1117–1131, 1971.

[82] Karelle Ménochet, Kathryn E Kenworthy, J Brian Houston, and Aleksandra Galetin. Simultaneous assessment of uptake and metabolism in rat hepatocytes: a comprehensive mechanistic model. *Journal of Pharmacology and Experimental Therapeutics*, 341(1):2–15, 2012.

[83] Karelle Menochet, Kathryn E Kenworthy, J Brian Houston, and Aleksandra Galetin. Use of mechanistic modeling to assess interindividual variability and interspecies differences in active uptake in human and rat hepatocytes. *Drug Metabolism and Disposition*, 40(9):1744–1756, 2012.

[84] Joseph A Leedale, Jonathan A Kyffin, Amy L Harding, Helen E Colley, Craig Murdoch, Parveen Sharma, Dominic P Williams, Steven D Webb, and Rachel N Bearon. Multiscale modelling of drug transport and metabolism in liver spheroids. *Interface focus*, 10(2):20190041, 2020.

[85] Joel L Bert, Joyce M Mathieson, and Richard H Pearce. The exclusion of human serum albumin by human dermal collagenous fibres and within human dermis. *Biochemical Journal*, 201(2):395–403, 1982.

[86] Saroja Ramanujan, Alain Pluen, Trevor D McKee, Edward B Brown, Yves Boucher, and Rakesh K Jain. Diffusion and convection in collagen gels: implications for transport in the tumor interstitium. *Biophysical journal*, 83(3): 1650–1660, 2002.

[87] Yuri Dancik, Matthew A Miller, Joanna Jaworska, and Gerald B Kasting. Design and performance of a spreadsheet-based model for estimating bioavailability of chemicals from dermal exposure. *Advanced drug delivery reviews*, 65(2): 221–236, 2013.

[88] Neera Jain and Samuel H Yalkowsky. Estimation of the aqueous solubility i: application to organic nonelectrolytes. *Journal of pharmaceutical sciences*, 90 (2):234–252, 2001.

[89] Siamaque Kazem, Emma Charlotte Linssen, and Susan Gibbs. Skin metabolism phase i and phase ii enzymes in native and reconstructed human skin: a short review. *Drug discovery today*, 2019.

[90] Anke Wilm, Jochen Kühnl, and Johannes Kirchmair. Computational approaches for skin sensitization prediction. *Critical reviews in toxicology*, 48 (9):738–760, 2018.

[91] Qingda Zang, Michael Paris, David M Lehmann, Shannon Bell, Nicole Kleinstreuer, David Allen, Joanna Matheson, Abigail Jacobs, Warren Casey, and Judy Strickland. Prediction of skin sensitization potency using machine learning approaches. *Journal of Applied Toxicology*, 37(7):792–805, 2017.

[92] Gerald B Kasting, Matthew A Miller, and Varsha D Bhatt. A spreadsheet-based method for estimating the skin disposition of volatile compounds: application to n, n-diethyl-m-toluamide (deet). *Journal of occupational and environmental hygiene*, 5(10):633–644, 2008.

[93] Joke A Bouwstra, Anko de Graaff, Gert S Gooris, Jaap Nijsse, Johann W Wiechers, and Adriaan C van Aelst. Water distribution and related morphology in human stratum corneum at different hydration levels. *Journal of Investigative Dermatology*, 120(5):750–758, 2003.

[94] Ronald R Warner, Keith J Stone, and Ying L Boissy. Hydration disrupts human stratum corneum ultrastructure. *Journal of investigative dermatology*, 120(2): 275–284, 2003.

[95] Mark Pellett, Michael Roberts, and Jonathon Hadgraft. Supersaturated solutions evaluated with an in vitro stratum corneum tape stripping technique. *International journal of pharmaceutics*, 151(1):91–98, 1997.

[96] Beverly B Sanders and KW Smith. Dinitrochlorobenzene immunotherapy of human warts. *Cutis*, 27(4):389–392, 1981.

[97] Guoping Lian, Longjian Chen, and Lujia Han. An evaluation of mathematical models for predicting skin permeability. *Journal of pharmaceutical sciences*, 97 (1):584–598, 2008.

[98] Ahlam Zaid Alkilani, Maelíosa TC McCrudden, and Ryan F Donnelly. Transdermal drug delivery: innovative pharmaceutical developments based on disruption of the barrier properties of the stratum corneum. *Pharmaceutics*, 7(4): 438–470, 2015.

[99] Inderjeet Singh and Andrew Phillip Morris. Performance of transdermal therapeutic systems: Effects of biological factors. *International journal of pharmaceutical investigation*, 1(1):4, 2011.

[100] Hannah M Jones, Iain B Gardner, and Kenny J Watson. Modelling and pbpk simulation in drug discovery. *The AAPS journal*, 11(1):155–166, 2009.

[101] P Zhao, L Zhang, JA Grillo, Q Liu, JM Bullock, YJ Moon, P Song, SS Brar, R Madabushi, TC Wu, et al. Applications of physiologically based pharmacokinetic (pbpk) modeling and simulation during regulatory review. *Clinical Pharmacology & Therapeutics*, 89(2):259–267, 2011.

[102] Jennifer E Sager, Jingjing Yu, Isabelle Ragueneau-Majlessi, and Nina Isoherranen. Physiologically based pharmacokinetic (pbpk) modeling and simulation

approaches: a systematic review of published models, applications, and model verification. *Drug Metabolism and Disposition*, 43(11):1823–1837, 2015.

[103] Masoud Jamei. Where do pbpk models stand in pharmacometrics and systems pharmacology? *CPT: Pharmacometrics & Systems Pharmacology*, 2020.

[104] Sheila Annie Peters. Evaluation of a generic physiologically based pharmacokinetic model for lineshape analysis. *Clinical pharmacokinetics*, 47(4):261–275, 2008.

[105] Yuching Yang, Xu Xu, and Panos G Georgopoulos. A bayesian population pbpk model for multiroute chloroform exposure. *Journal of exposure science & environmental epidemiology*, 20(4):326–341, 2010.

[106] Markus Krauss, Kai Tappe, Andreas Schuppert, Lars Kuepfer, and Linus Goerlitz. Bayesian population physiologically-based pharmacokinetic (pbpk) approach for a physiologically realistic characterization of interindividual variability in clinically relevant populations. *PloS one*, 10(10), 2015.

[107] Sheila Annie Peters. *Physiologically-based pharmacokinetic (PBPK) modeling and simulations: principles, methods, and applications in the pharmaceutical industry*. John Wiley & Sons, 2012.

[108] Hannah Jones and Karen Rowland-Yeo. Basic concepts in physiologically based pharmacokinetic modeling in drug discovery and development. *CPT: pharmacometrics & systems pharmacology*, 2(8):1–12, 2013.

[109] Patrick Poulin and Frank-Peter Theil. Prediction of pharmacokinetics prior to in vivo studies. 1. mechanism-based prediction of volume of distribution. *Journal of pharmaceutical sciences*, 91(1):129–156, 2002.

[110] Trudy Rodgers, David Leahy, and Malcolm Rowland. Physiologically based pharmacokinetic modeling 1: predicting the tissue distribution of moderate-to-strong bases. *Journal of pharmaceutical sciences*, 94(6):1259–1276, 2005.

[111] Trudy Rodgers and Malcolm Rowland. Physiologically based pharmacokinetic modelling 2: predicting the tissue distribution of acids, very weak bases, neutrals and zwitterions. *Journal of pharmaceutical sciences*, 95(6):1238–1257, 2006.

[112] Malcolm Rowland and Thomas N Tozer. *Clinical pharmacokinetics: concepts and applications*, volume 162. Lea & Febiger Philadelphia, 1989.

[113] Jianghong Fan, Shu Chen, Edwin CY Chow, and K Sandy Pang. Pbpk modeling of intestinal and liver enzymes and transporters in drug absorption and sequential metabolism. *Current drug metabolism*, 11(9):743–761, 2010.

[114] Lu Gaohua, Khaled Abduljalil, Masoud Jamei, Trevor N Johnson, and Amin Rostami-Hodjegan. A pregnancy physiologically based pharmacokinetic (p-pbpk) model for disposition of drugs metabolized by cyp1a2, cyp2d6 and cyp3a4. *British journal of clinical pharmacology*, 74(5):873–885, 2012.

[115] C-H Hsueh, V Hsu, P Zhao, L Zhang, KM Giacomini, and S-M Huang. Pbpk modeling of the effect of reduced kidney function on the pharmacokinetics of

drugs excreted renally by organic anion transporters. *Clinical Pharmacology & Therapeutics*, 103(3):485–492, 2018.

[116] Christopher M Florkowski and Janice SC Chew-Harris. Methods of estimating gfr–different equations including ckd-epi. *The Clinical Biochemist Reviews*, 32 (2):75, 2011.

[117] Sibylle Neuhoff, Lu Gaohua, Howard Burt, Masoud Jamei, Linzhong Li, Geoffrey T Tucker, and Amin Rostami-Hodjegan. Accounting for transporters in renal clearance: towards a mechanistic kidney model (mech kim). In *Transporters in Drug Development*, pages 155–177. Springer, 2013.

[118] Daniel Scotcher, Christopher Jones, Maria Posada, Aleksandra Galetin, and Amin Rostami-Hodjegan. Key to opening kidney for in vitro-in vivo extrapolation entrance in health and disease: Part ii: Mechanistic models and in vitro-in vivo extrapolation. *The AAPS journal*, 18(5):1082–1094, 2016.

[119] Sheila Annie Peters and Hugues Dolgos. Requirements to establishing confidence in physiologically based pharmacokinetic (pbpk) models and overcoming some of the challenges to meeting them. *Clinical Pharmacokinetics*, 58(11): 1355–1371, 2019.

[120] European Medicines Agency. Guideline on the qualification and reporting of physiologically based pharmacokinetic (pbpk) modelling and simulation, 2016.

[121] Food and Drugs Administration. Physiologically based pharmacokinetic analyses âĂŤ format and content guidance for industry, 2018.

[122] Mohamad Shebley, Punam Sandhu, Arian Emami Riedmaier, Masoud Jamei, Rangaraj Narayanan, Aarti Patel, Sheila Annie Peters, Venkatesh Pilla Reddy, Ming Zheng, Loeckie de Zwart, et al. Physiologically based pharmacokinetic model qualification and reporting procedures for regulatory submissions: a consortium perspective. *Clinical Pharmacology & Therapeutics*, 104(1):88–110, 2018.

[123] Kosmas Kretsos and Gerald Kasting. Dermal capillary clearance: physiology and modeling. *Skin pharmacology and physiology*, 18(2):55–74, 2005.

[124] Rania Ibrahim, Johannes M Nitsche, and Gerald B Kasting. Dermal clearance model for epidermal bioavailability calculations. *Journal of pharmaceutical sciences*, 101(6):2094–2108, 2012.

[125] Charles Michel and FitRoz Curry. Microvascular permeability. *Physiological reviews*, 79(3):703–761, 1999.

[126] Edward Lansing Cussler and Edward Lansing Cussler. *Diffusion: mass transfer in fluid systems*. Cambridge university press, 2009.

[127] Corwin Hansch and Albert Leo. Exploring qsar. hydrophobic, electronic, and steric constants. acs professional reference book. *ACS, Washington*, 1995.

[128] Reiko Watanabe, Tsuyoshi Esaki, Hitoshi Kawashima, Yayoi Natsume-Kitatani, Chioko Nagao, Rikiya Ohashi, and Kenji Mizuguchi. Predicting fraction unbound in human plasma from chemical structure: improved accuracy in the low value ranges. *Molecular pharmaceutics*, 15(11):5302–5311, 2018.

[129] Albert P Li, Asenath Rasmussen, Lilly Xu, and Donald L Kaminski. Rifampicin induction of lidocaine metabolism in cultured human hepatocytes. *Journal of Pharmacology and Experimental Therapeutics*, 274(2):673–677, 1995.

[130] Leslie Z Benet and Jasleen K Sodhi. Investigating the theoretical basis for in vitro–in vivo extrapolation (ivive) in predicting drug metabolic clearance and proposing future experimental pathways. *The AAPS Journal*, 22(5):1–11, 2020.

[131] Amin Rostami-Hodjegan. Translation of in vitro metabolic data to predict in vivo drug–drug interactions: Ivive and modeling and simulations. In *Enzyme- and Transporter-Based Drug-Drug Interactions*, pages 317–341. Springer, 2010.

[132] David Hallifax, Joanne A Foster, and J Brian Houston. Prediction of human metabolic clearance from in vitro systems: retrospective analysis and prospective view. *Pharmaceutical research*, 27(10):2150–2161, 2010.

[133] HERMAN R Ochs, MARTIN Knuchel, DARRELL R Abernethy, and DAVID J Greenblatt. Dose-independent pharmacokinetics of intravenous lidocaine in humans. *Journal of clinical pharmacology*, 23(4):186–188, 1983.

[134] Jeffrey C Lagarias, James A Reeds, Margaret H Wright, and Paul E Wright. Convergence properties of the nelder–mead simplex method in low dimensions. *SIAM Journal on optimization*, 9(1):112–147, 1998.

[135] Food and Drugs administration. Lidoderm. URL `https://www.accessdata.fda.gov/drugsatfda_docs/label/2015/020612s012lbl.pdf`. (accessed: 21.1.2020).

[136] Lisa M Russell, Sandra Wiedersberg, and M Begoña Delgado-Charro. The determination of stratum corneum thickness an alternative approach. *European journal of pharmaceutics and biopharmaceutics*, 69(3):861–870, 2008.

[137] Donald YM Leung, Mark Boguniewicz, Michael D Howell, Ichiro Nomura, and Qutayba A Hamid. New insights into atopic dermatitis. *The Journal of clinical investigation*, 113(5):651–657, 2004.

[138] Hywel C Williams. Atopic dermatitis. *New England Journal of Medicine*, 352 (22):2314–2324, 2005.

[139] Michael J Cork, Simon G Danby, Yiannis Vasilopoulos, Jonathan Hadgraft, Majella E Lane, Manar Moustafa, Richard H Guy, Alice L MacGowan, Rachid Tazi-Ahnini, and Simon J Ward. Epidermal barrier dysfunction in atopic dermatitis. *Journal of Investigative Dermatology*, 129(8):1892–1908, 2009.

[140] Colin NA Palmer, Alan D Irvine, Ana Terron-Kwiatkowski, Yiwei Zhao, Haihui Liao, Simon P Lee, David R Goudie, Aileen Sandilands, Linda E Campbell, Frances JD Smith, et al. Common loss-of-function variants of the epidermal barrier protein filaggrin are a major predisposing factor for atopic dermatitis. *Nature genetics*, 38(4):441–446, 2006.

[141] Michael Mildner, Jiang Jin, Leopold Eckhart, Sanja Kezic, Florian Gruber, Caterina Barresi, Caroline Stremnitzer, Maria Buchberger, Veronika Mlitz, Claudia Ballaun, et al. Knockdown of filaggrin impairs diffusion barrier func-

tion and increases uv sensitivity in a human skin model. *Journal of Investigative Dermatology*, 130(9):2286–2294, 2010.

[142] Ting Jiang, Kai Jin, Xianpping Liu, and Zhiqing Pang. 8 - nanoparticles for tumor targeting. In Sougata Jana, Sabyasachi Maiti, and Subrata Jana, editors, *Biopolymer-Based Composites*, pages 221 – 267. Woodhead Publishing, 2017. ISBN 978-0-08-101914-6. doi: https://doi.org/10.1016/B978-0-08-101914-6.00008-9. URL `http://www.sciencedirect.com/science/article/pii/B9780081019146000089`.

[143] Rebecca L Siegel, Kimberly D Miller, Stacey A Fedewa, Dennis J Ahnen, Reinier GS Meester, Afsaneh Barzi, and Ahmedin Jemal. Colorectal cancer statistics, 2017. *CA: a cancer journal for clinicians*, 67(3):177–193, 2017.

[144] Office of National Statistics. Cancer registration statistics, england: 2014, . URL `https://www.ons.gov.uk/peoplepopulationandcommunity/healthandsocialcare/conditionsanddiseases/bulletins/cancerregistrationstatisticsengland/2014`. (accessed: 20.03.2019).

[145] Office of National Statistics. Cancer survival in england-adults diagnosed: 2009 to 2013, followed up to 2014, . URL `https://www.ons.gov.uk/peoplepopulationandcommunity/healthandsocialcare/conditionsanddiseases/bulletins/cancersurvivalinenglandadultsdiagnosed/2009to2013followedupto2014`. (accessed: 20.03.2019).

[146] Types of cancer treatment. URL `https://www.cancer.gov/about-cancer/treatment/types`. (accessed: 02.05.2019).

[147] BWKP Stewart, Christopher P Wild, et al. World cancer report 2014. *Public Health*, 2019.

[148] Chanchala D Kaddi, John H Phan, and May D Wang. Computational nanomedicine: modeling of nanoparticle-mediated hyperthermal cancer therapy. *Nanomedicine*, 8(8):1323–1333, 2013.

[149] David E Gerber. Targeted therapies: a new generation of cancer treatments. *American family physician*, 77(3), 2008.

[150] Nadége Carelle, Estelle Piotto, Agnés Bellanger, Jerome Germanaud, Alain Thuillier, and David Khayat. Changing patient perceptions of the side effects of cancer chemotherapy. *Cancer*, 95(1):155–163, 2002.

[151] Yasuhiro Matsumura and Hiroshi Maeda. A new concept for macromolecular therapeutics in cancer chemotherapy: mechanism of tumoritropic accumulation of proteins and the antitumor agent smancs. *Cancer research*, 46(12 Part 1): 6387–6392, 1986.

[152] Bohdana M Discher, Harry Bermudez, Daniel A Hammer, Dennis E Discher, You-Yeon Won, and Frank S Bates. Cross-linked polymersome membranes: vesicles with broadly adjustable properties. *The Journal of Physical Chemistry B*, 106(11):2848–2854, 2002.

[153] Fariyal Ahmed, Refika I Pakunlu, Aaron Brannan, Frank Bates, Tamara Minko, and Dennis E Discher. Biodegradable polymersomes loaded with both paclitaxel and doxorubicin permeate and shrink tumors, inducing apoptosis in proportion to accumulated drug. *Journal of Controlled Release*, 116(2):150–158, 2006.

[154] Hannah Lomas, Marzia Massignani, Khairuddin A Abdullah, Irene Canton, Caterina Lo Presti, Sheila MacNeil, Jianzhong Du, Adam Blanazs, Jeppe Madsen, Steven P Armes, et al. Non-cytotoxic polymer vesicles for rapid and efficient intracellular delivery. *Faraday discussions*, 139:143–159, 2008.

[155] Huanli Sun, Fenghua Meng, Ru Cheng, Chao Deng, and Zhiyuan Zhong. Reduction and ph dual-bioresponsive crosslinked polymersomes for efficient intracellular delivery of proteins and potent induction of cancer cell apoptosis. *Acta biomaterialia*, 10(5):2159–2168, 2014.

[156] Wei Chen, Fenghua Meng, Ru Cheng, and Zhiyuan Zhong. ph-sensitive degradable polymersomes for triggered release of anticancer drugs: a comparative study with micelles. *Journal of Controlled Release*, 142(1):40–46, 2010.

[157] Cristiano Giacomelli, Lucile Le Men, Redouane Borsali, Joséphine Lai-Kee-Him, Alain Brisson, Steven P Armes, and Andrew L Lewis. Phosphorylcholine-based ph-responsive diblock copolymer micelles as drug delivery vehicles: light scattering, electron microscopy, and fluorescence experiments. *Biomacromolecules*, 7(3):817–828, 2006.

[158] Lei Shen, Jianzhong Du, Steven P Armes, and Shiyong Liu. Kinetics of ph-

induced formation and dissociation of polymeric vesicles assembled from a water-soluble zwitterionic diblock copolymer. *Langmuir*, 24(18):10019–10025, 2008.

[159] Karel Ulbrich and Vladimır Šubr. Polymeric anticancer drugs with ph-controlled activation. *Advanced drug delivery reviews*, 56(7):1023–1050, 2004.

[160] Jackie E Hipp. Modulation classification based on statistical moments. In *MILCOM 1986-IEEE Military Communications Conference: Communications-Computers: Teamed for the 90's*, volume 2, pages 20–2. IEEE, 1986.

[161] Kenneth Wilson, ON Bjørnstad, AP Dobson, Stefano Merler, G Poglayen, SE Randolph, AF Read, and A Skorping. Heterogeneities in macroparasite infections: patterns and processes. *The ecology of wildlife diseases*, 44:6–44, 2002.

[162] Hsieh-Fu Tsai, Alen Trubelja, Amy Q Shen, and Gang Bao. Tumour-on-a-chip: microfluidic models of tumour morphology, growth and microenvironment. *Journal of the Royal Society Interface*, 14(131):20170137, 2017.

[163] Kayla Duval, Hannah Grover, Li-Hsin Han, Yongchao Mou, Adrian F Pegoraro, Jeffery Fredberg, and Zi Chen. Modeling physiological events in 2d vs. 3d cell culture. *Physiology*, 32(4):266–277, 2017.

[164] Rasheena Edmondson, Jessica Jenkins Broglie, Audrey F Adcock, and Liju Yang. Three-dimensional cell culture systems and their applications in drug

discovery and cell-based biosensors. *Assay and drug development technologies*, 12(4):207–218, 2014.

[165] Jonathan Arthur Kyffin. *Establishing species-specific 3D liver microtissues for repeat dose toxicology and advancing in vitro to in vivo translation through computational modelling*. PhD thesis, Liverpool John Moores University, 2018.

[166] John P Ward and John R King. Mathematical modelling of drug transport in tumour multicell spheroids and monolayer cultures. *Mathematical biosciences*, 181(2):177–207, 2003.

[167] Jörgen Carlsson and Thore Nederman. Tumour spheroid technology in cancer therapy research. *European Journal of Cancer and Clinical Oncology*, 25(8): 1127–1133, 1989.

[168] David J Kerr, Thomas E Wheldon, Sharyn Hydns, and Stanley B Kaye. Cytotoxic drug penetration studies in multicellular tumour spheroids. *Xenobiotica*, 18(6):641–648, 1988.

[169] Johann Hansing and Roland R Netz. Hydrodynamic effects on particle diffusion in polymeric hydrogels with steric and electrostatic particle–gel interactions. *Macromolecules*, 51(19):7608–7620, 2018.

[170] Triantafyllos Stylianopoulos, Ming-Zher Poh, Numpon Insin, Moungi G Bawendi, Dai Fukumura, Lance L Munn, and Rakesh K Jain. Diffusion of particles in the extracellular matrix: the effect of repulsive electrostatic interactions. *Biophysical journal*, 99(5):1342–1349, 2010.

[171] Alastair H Kyle, Carmel TO Chan, and Andrew I Minchinton. Characterization of three-dimensional tissue cultures using electrical impedance spectroscopy. *Biophysical journal*, 76(5):2640–2648, 1999.

[172] Sara Kaliman, Christina Jayachandran, Florian Rehfeldt, and Ana-Sunčana Smith. Limits of applicability of the voronoi tessellation determined by centers of cell nuclei to epithelium morphology. *Frontiers in physiology*, 7:551, 2016.

[173] Anne E Carpenter, Thouis R Jones, Michael R Lamprecht, Colin Clarke, In Han Kang, Ola Friman, David A Guertin, Joo Han Chang, Robert A Lindquist, Jason Moffat, et al. Cellprofiler: image analysis software for identifying and quantifying cell phenotypes. *Genome biology*, 7(10):R100, 2006.

[174] Atsuyuki Okabe, Barry Boots, and Kokichi Sugihara. *Spatial Tessellations: Concepts and Applications of Voronoi Diagrams*. John Wiley & Sons, Inc., New York, NY, USA, 1992. ISBN 0-471-93430-5.

[175] Adam Dobrin. A review of properties and variations of voronoi diagrams. *Whitman College*, pages 1949–3053, 2005.

[176] Kazumori Funatsu, Hiroyuki Ijima, Kohji Nakazawa, Yo-ichi Yamashita, Mitsuo Shimada, and Keizo Sugimachi. Hybrid artificial liver using hepatocyte organoid culture. *Artificial organs*, 25(3):194–200, 2001.

[177] Pietro Mascheroni, M Carfagna, Alfio Grillo, Daniela Boso, and Bernhard Schrefler. An avascular tumor growth model based on porous media mechan-

ics and evolving natural states. *Mathematics and Mechanics of Solids*, 23(4): 686–712, 2018.

[178] Maria Teresa Santini, Gabriella Rainaldi, and Pietro Luigi Indovina. Apoptosis, cell adhesion and the extracellular matrix in the three-dimensional growth of multicellular tumor spheroids. *Critical reviews in oncology/hematology*, 36(2-3): 75–87, 2000.

[179] Simeone Marino, Ian B Hogue, Christian J Ray, and Denise E Kirschner. A methodology for performing global uncertainty and sensitivity analysis in systems biology. *Journal of theoretical biology*, 254(1):178–196, 2008.

[180] He Wei and Yang Hua. Efast method for global sensitivity analysis of remote sensing modelâĂŹs parameters. *Remote Sensing Technol. Appl*, 28:836–843, 2013.

[181] Ilya M Sobol. Sensitivity estimates for nonlinear mathematical models. *Math. Model. Comput. Exp*, 1(4):407–414, 1993.

[182] Marco Ratto Andrea Saltelli. *Global Sensitivity Analysis. The Primer.*

[183] X-Y Zhang, MN Trame, LJ Lesko, and S Schmidt. Sobol sensitivity analysis: a tool to guide the development and evaluation of systems pharmacology models. *CPT: pharmacometrics & systems pharmacology*, 4(2):69–79, 2015.

[184] Andrea Saltelli, Paola Annoni, Ivano Azzini, Francesca Campolongo, Marco Ratto, and Stefano Tarantola. Variance based sensitivity analysis of model

output. design and estimator for the total sensitivity index. *Computer Physics Communications*, 181(2):259–270, 2010.

[185] John W Hickey, Jose Luis Santos, John-Michael Williford, and Hai-Quan Mao. Control of polymeric nanoparticle size to improve therapeutic delivery. *Journal of Controlled Release*, 219:536–547, 2015.

[186] Sarah A Smith, Helen E Colley, Parveen Sharma, Klaudia M Slowik, Rowena Sison-Young, Andrew Sneddon, Steven D Webb, and Craig Murdoch. Expression and enzyme activity of cytochrome p450 enzymes cyp 3a4 and cyp 3a5 in human skin and tissue-engineered skin equivalents. *Experimental dermatology*, 27(5):473–475, 2018.

[187] Adrian Williams et al. *Transdermal and topical drug delivery: from theory to clinical practice*. Pharmaceutical Press London, 2003.

[188] Ute Jacobi, Julien Gautier, Wolfram Sterry, and Jürgen Lademann. Gender-related differences in the physiology of the stratum corneum. *Dermatology*, 211 (4):312–317, 2005.

[189] Jane Fore. A review of skin and the effects of aging on skin structure and function. *Ostomy/wound management*, 52(9):24–35, 2006.

[190] E Berardesca and HI Maibach. Racial differences in pharmacodynamic response to nicotinates in vivo in human skin: black and white. *Acta dermato-venereologica*, 70(1):63–66, 1990.

[191] Dennis Allen Weigand, Carl Haygood, and James R Gaylor. Cell layer and density of negro and caucasian stratum corneum. *Journal of Investigative Dermatology*, 62(6):563–568, 1974.

[192] Cheng-Tao Chang and Robert L Wong. Assessment of intrasubject variability of pharmacokinetic parameters in clinical studies. *Drug information journal: DIJ/Drug Information Association*, 31(4):1203–1213, 1997.